FAKULTA MECHATRONIKY,
INFORMATIKY A MEZIOBOROVÝCH
STUDIÍ TUL

Disertační práce

Fluorescence lifetime imaging via the RATS method in a single-pixel camera configuration

Studijní program:	P3901 Aplikované vědy v inženýrství
Studijní obor:	Aplikované vědy v inženýrství
Autor práce:	**Ing. Jiří Junek**
Školitel práce:	RNDr. Karel Žídek, Ph.D. Ústav nových technologií a aplikované informatiky

Liberec 2022

Prohlášení

Prohlašuji, že svou disertační práci jsem vypracoval samostatně jako původní dílo s použitím uvedené literatury a na základě konzultací s vedoucím mé disertační práce a konzultantem.

Jsem si vědom toho, že na mou disertační práci se plně vztahuje zákon č. 121/2000 Sb., o právu autorském, zejména § 60 – školní dílo.

Beru na vědomí, že Technická univerzita v Liberci nezasahuje do mých autorských práv užitím mé disertační práce pro vnitřní potřebu Technické univerzity v Liberci.

Užiji-li disertační práci nebo poskytnu-li licenci k jejímu využití, jsem si vědom povinnosti informovat o této skutečnosti Technickou univerzitu v Liberci; v tomto případě má Technická univerzita v Liberci právo ode mne požadovat úhradu nákladů, které vynaložila na vytvoření díla, až do jejich skutečné výše.

Současně čestně prohlašuji, že text elektronické podoby práce vložený do IS/STAG se shoduje s textem tištěné podoby práce.

Beru na vědomí, že má disertační práce bude zveřejněna Technickou univerzitou v Liberci v souladu s § 47b zákona č. 111/1998 Sb., o vysokých školách a o změně a doplnění dalších zákonů (zákon o vysokých školách), ve znění pozdějších předpisů.

Jsem si vědom následků, které podle zákona o vysokých školách mohou vyplývat z porušení tohoto prohlášení.

19. prosince 2022 Ing. Jiří Junek

Anotace

Zobrazování doby života fluorescence (FLIM) patří mezi hojně rozšířené přístupy pro analýzu materiálů v široké škále výzkumných témat. Je však vždy nutné zvolit vhodnou principiální metodu pro měření dynamiky fotoluminiscence (PL) vzhledem k měřenému vzorku.

V rámci dizertační práce je představen návrh nové robustní metody, kde není nutná předběžná znalost PL dynamiky vzorku. Princip využívá náhodně modulovaný excitační signál, což umožňuje měřit dohasínání na širokém rozsahu frekvencí v rámci jedné datové sady. To zaručuje přesnou rekonstrukci multi-exponenciální křivky dohasínání PL. Metoda získala název RATS z anglického „Random temporal signals". Pro účely FLIM lze metodu RATS přenést do 2D snímání například pomocí konfigurace jedno-pixelové kamery (SPC). Zde jsou prezentovány dvě optické uspořádání metody RATS využívající SPC. První z nich využívá dvou difusorů (dvakrát rozptýlené světlo), které jednak zajistí náhodnost časového signálu, ale i náhodné prostorové osvětlení měřeného vzorku -- stěžejní pro rekonstrukci SPC scény. Druhé optické uspořádání je implementace metody RATS do SPC mikroskopu, kde je prostorová náhodnost zajištěna digitálně ovládaným mikro-zrcátkovým čipem (DMD) a časová náhodnost je zajištěn náhodně digitálně modulovaným laserem.

Kromě toho práce představuje dva rekonstrukční přístupy FLIM spektrogramu. První z nich se blíží standardním přístupům rekonstrukce spektrogramu FLIM v SPC. Proto sdílí podobné vlastnosti, jako je počet nutných rekonstrukcí vedoucí k dlouhé době výpočetního zpracování výsledků. Druhý z navrhovaných rekonstrukčních přístupů však potřebuje pouze tolik rekonstrukcí, kolik je dílčích životů dohasínání obsaženo v multi-exponenciální křivce PL dohasínání (obvykle bi-, tri-). To výrazně šetří čas následného zpracování. Navíc umožňuje zobrazení amplitudových map jednotlivých životů PL, což může být přínosné pro výzkum materiálového inženýrství. Oba přístupy jsou analyzovány pomocí simulací z hlediska šumových charakteristik a jsou vzájemně porovnávány.

Nakonec jsou uvedeny myšlenky přímé rekonstrukce parametrů multi-exponenciálních křivek dohasínání v případech se šumem. První návrh, založený na řešení nedourčeného systému, očekává řídké řešení. Poskytuje přesné výsledky, ale není vhodný pro systém se šumem. Druhý návrh, využívá hlubokého učení a ukazuje na možnost získat hledané parametry dohasínání i v systému se šumem. Hladina šumu (0-1%) navíc neovlivňuje přesnost zjištěných parametrů. Tyto přístupy by nahradily regresní zpracování a dále zjednodušily metodu.

Klíčová slova: spektrometrie FLIM, metoda RATS, komprimované snímání, jedno-pixelová kamera

Annotation

Fluorescence lifetime imaging (FLIM) is one of the most widespread approaches to materials analysis in a broad range of scientific fields. However, it is always necessary to choose a principal method for measuring the dynamics of photoluminescence (PL) concerning the measured sample.

As a part of the dissertation thesis, a new robust and straightforward method for PL dynamics measurement is presented, eliminating the need for prior knowledge about the PL dynamics of the sample. The method is based on a randomly modulated excitation signal, which makes it possible to measure PL decay at a wide range of frequencies within a single dataset. This guarantees an accurate reconstruction of the multi-exponential PL decay curve. The method was named RATS according to the "Random temporal signals". The RATS method can be transferred to 2D imaging by using a single-pixel camera (SPC) configuration. Here are presented two optical arrangements of the RATS method in SPC. The first of them is based on two diffusers (double-diffused light), which both ensure the randomness of the temporal signal and the random spatial illumination of the measured sample -- crucial for the SPC scene reconstruction. The second optical arrangement is an implementation of the RATS method into the SPC microscope setup, where spatial randomness is ensured by a digital micro-mirror device (DMD) and temporal randomness is ensured by a randomly digitally modulated laser.

Moreover, two reconstruction approaches for the FLIM spectrogram are introduced. The first of them is close to the standard approaches to FLIM spectrogram reconstruction in SPC and therefore shares similar properties, such as the number of necessary reconstructions leading to the long postprocessing time. However, the second of the proposed reconstruction approaches only needs as many reconstructions as the number of partial lifetimes of multi-exponential PL decay (usually bi-, tri-). This significantly saves post-processing time. In addition, it allows displaying the amplitude maps of individual lifetimes, which can be beneficial for material engineering research. Both of them are analyzed via simulations in terms of noise characteristics and are compared.

The thesis is concluded by ideas of precise and direct reconstruction of multi-exponential decay parameters in a noisy system. The first proposed solution, based on an undetermined system, expects a sparse solution. It gives precise results but is not suitable for noisy systems. However, using the second proposal, based on deep learning, it is possible to get precise decay parameters even in noisy systems. Moreover, the noise level (0-1%) does not seriously affect the precision of the found parameters. The algorithms would replace the regression processing and would further simplify the method.

Keywords: FLIM spectrometry, RATS method, compressed sensing, single-pixel camera

Acknowledgement

I would like to give warm thanks to my supervisor doc. RNDr. Karel Žídek, Ph.D. His passion for science and endless enthusiasm for work gave me big moral support to finish this thesis. I am also grateful to Ing. Karel Paleček, Ph.D., who kindly discussed with me the issue of deep learning.

I also want to thank all my colleagues at the TOPTEC research centre, where I had the opportunity to build my optical setups and discuss my issues over coffee breaks.

Special thanks to my family for their endless support. Above all, I thank my wife for her patience and love. I can not forget my brother, who helped me get motors for my very first attempts at building a rotary diffuser-based random signal generator.

Dedication

I would like to dedicate this work to my father, whose lifetime ended too early. However, his philosophy of life - "Do anything properly or not at all." - has excited me and many people worldwide.

List of all author's publications

1. J. Junek, and K. Žídek, "Luminescence Decay Measurement via Temporal Speckles," in *Imaging and Applied Optics 2019 (COSI, IS, MATH, PcAOP) (2019), Paper CW4A.7* (Optical Society of America, 2019), p. CW4A.7.

2. J. Junek, L. Ondič, and K. Žídek, "Random temporal laser speckles for the robust measurement of sub-microsecond photoluminescence decay," Opt. Express, OE **28**(8), 12363–12372 (2020).

3. J. Junek, and K. Zidek, "FLIM via RATS Method Using Single Pixel Camera," in *Imaging and Applied Optics Congress (2020), Paper JW5C.1* (Optical Society of America, 2020), p. JW5C.1.

4. J. Junek, and K. Žídek, "Fluorescence lifetime imaging via spatio-temporal speckle patterns in a single-pixel camera configuration," Opt. Express, OE **29**(4), 5538–5551 (2021).

5. J. Junek, and K. Žídek, "Noise Effect to Data Acquisition Time in FLIM via RATS Method Using Single-Pixel Camera Configuration," in *OSA Optical Sensors and Sensing Congress 2021 (AIS, FTS, HISE, SENSORS, ES) (2021), Paper JTh6A.8* (Optical Society of America, 2021), p. JTh6A.8.

6. J. Junek, and K. Žídek, "Noise effect on 2D photoluminescence decay analysis using the RATS method in a single-pixel camera configuration," Opt. Express, OE **30**(8), 12654–12669 (2022).

7. P. Reinig, H.-G. Dallmann, M. Schwarzenberg, J. Ziebarth, J. Knobbe, J. Junek, R. Herbst, J. Rathert, R. Gerlach, U. Blache, S. Tretbar, and S. Fricke, "MEMS-based confocal laser scanning fluorescence microscopy for tumor demarcation in oncological surgery," in Advanced Biomedical and Clinical Diagnostic and Surgical Guidance Systems XX (SPIE, 2022), Vol. 11949, pp. 32–40.

8. J. Junek, and K. Žídek, " Nanosecond compressive fluorescence lifetime microscopy imaging via the RATS method with a direct reconstruction of lifetime maps," arXiv: 2208.13640v3 [physics] (2022).

Author's publications with scope outside of the thesis

9. J. Budasz, J. Junek, and J. Václavík, "Broadband antireflective coating for NEOSTED," in *Optics and Measurement International Conference 2016* (SPIE, 2016), Vol. 10151, pp. 213–221.

10. Junek J, "Model mechanického napětí v systému multivrstev," Jemná mechanika a optika, JMO **63**(2), 62-64 (2018).

11. Špína M., Procháska F., Junek J., Malá K, "Analýza referenčních povrchových vad optických ploch za použití konfokální mikroskopie, interferometrie v bílém světle a mikroskopie atomárních sil," Jemná mechanika a optika, JMO **63**(3), 81-84 (2018).

12. Junek J., and Šulc M, "Měření intenzity světla koherentních svazků pod úrovní šumu detektoru," Jemná mechanika a optika, JMO **64**(1), 20-23 (2019).

List of included publications

[A] J. Junek, L. Ondič, and K. Žídek, "Random temporal laser speckles for the robust measurement of sub-microsecond photoluminescence decay," Opt. Express, OE **28**(8), 12363–12372 (2020).

[B] J. Junek, and K. Žídek, "Fluorescence lifetime imaging via spatio-temporal speckle patterns in a single-pixel camera configuration," Opt. Express, OE **29**(4), 5538–5551 (2021).

[C] J. Junek, and K. Žídek, "Noise effect on 2D photoluminescence decay analysis using the RATS method in a single-pixel camera configuration," Opt. Express, OE **30**(8), 12654–12669 (2022).

[D] J. Junek, and K. Žídek, " Nanosecond compressive fluorescence lifetime microscopy imaging via the RATS method with a direct reconstruction of lifetime maps," arXiv: 2208.13640v3 [physics] (2022).

Description of included publications

Manuscript [A] describes a proof of principles of the 0D-RATS method based on a rotary diffuser (attached as the first in annexes) - in the introductory part of the thesis as s Ref. [46]. Manuscript [B] shows the first implementation of 2D-RATS based on double diffused light and introduces the $FLIM_B$ reconstruction approach (attached as the second in annexes) - in the introductory part of the thesis as a Ref. [47]. An extensive noise analysis of the RATS method is performed in the manuscript [C] (attached as the third in annexes) - in the introductory part of the thesis as a Ref. [50]. Manuscript [D] presents a less time-consuming and less computationally intensive spectrogram reconstruction approach ($FLIM_A$) and points out the possibility of achieving a nanosecond timescale via the RATS method (attached as the fourth in annexes) - in the introductory part of the thesis as a Ref. [49].

Contents

List of abbreviations

CCD	Charge-coupled device
CMOS	Complementary Metal–Oxide–Semiconductor
CNN	Convolutional neural network
CS	Compressed sensing
CUP	Compressed ultrafast photography
DMD	Digital micro-mirror device
iCCD	Intensified Charge Coupled Device
IRF	Impulse response function
FC	Fully connected layer
FLIM	Fluorescence lifetime imaging
FWHM	Full width at half maximum
MCP	Multichannel plate electron multiplier
MEMS	Micro electro mechanical system
NN	Neural network
LFSR	Linear feedback shift register
PL	Photoluminescence
PMT	Photomultiplier
RATS	Random temporal signals
SNR	Signal-to-noise ratio
SPAD	Single-photon avalanche detector
SPC	Single-pixel camera
TCSPC	Time-correlated single photon counting

1 Introduction

Due to the ever-evolving research of new materials, optical spectrometry is an essential analytical method, especially because it is a non-destructive and contactless method. One area of spectrometry is focused on photoluminescence (PL) properties. The PL occurs when charged carriers in a material are excited to a higher energy state by a suitable wavelength of photon radiation [1]. The excited carriers spontaneously return to their stable electronic state, partly by generating the above-mentioned PL. The material itself can then be evaluated in terms of the PL wavelength spectrum or studied from the point of view of the PL lifetime, generally referred to as the study of PL dynamics.

The study of PL dynamics thus makes it possible to reveal the lifetimes of PL decay [2] but also deals with the energy levels of charge carriers [3,4] or examines the mechanisms of relaxation and the transfer of excited energy [5,6]. All this information can be obtained for both transparent and non-transparent samples. Therefore, the measurement of PL dynamics is one of the most used characterization methods in the field of chemical physics [7,8], biochemistry [9] but also material sciences in general [10,11].

While the measurement of the time-integrated PL spectrum could be performed using a conventional spectrometer, time-resolved measurement needs advanced optical experimental arrangements, especially for rapid PL decays (nanosecond or sub-nanosecond timescales). Nowadays, there exist several approaches to measuring PL dynamics. Nevertheless, all standard approaches are often based on a pulsed laser, which makes the method expensive. Moreover, we frequently need to have a prior assumption of a measured lifetime. Besides, each method performs best in a limited range of lifetimes [1,12]. Therefore, it is still of great importance to deal with the development of new methods and approaches to measuring PL dynamics.

All these methods can be converted to 2D imaging of PL lifetimes, which is called "Fluorescence Lifetime Imaging" (FLIM) [13]. This approach is used mainly for biological samples (tracing using PL markers), where it is necessary to monitor ongoing processes [14,15]. Therefore, the main development direction is focused on fast data acquisition in terms of the photodegradation of biological samples and PL markers [16,17]. This is aided by a number of approaches, such as avalanche field sensing (SPAD) [18] or the concept of compressed sensing [19]. Besides, an important direction in the field of instrumentation is to create FLIM setups, which are versatile, low-cost and robust with respect to various experimental factors.

This thesis is devoted to the development and optimization of an entirely new approach to the measurement of PL dynamics and FLIM. The novel method - RATS - is proposed as the central part of this work. The method uses a randomly modulated excitation signal for sample excitation, which makes it possible to reconstruct any multi-exponential decay from a single acquired dataset. The method is robust and does not require any signal-timing. For FLIM measurements, the method was implemented in an optical

setup of a single-pixel camera configuration. The thesis comprises all steps, ranging from proof-of-principle experiments, noise analysis, optimization of the method performance with respect to the temporal and spatial resolution, and a novel approach to the analysis of the PL decays in FLIM.

In the following Chapter 2, commonly used measurement methods for FLIM are introduced. There are pointed out their advantages and ideal working range. Furthermore, a single-pixel camera -- compressed sensing (CS) technique -- is presented, and the intersection of PL dynamics study and CS techniques is outlined. Based on Chapter 2, Chapter 3 defines the main goals of the work. The individual solutions are further described in Chapters 4 -7. Chapter 4 introduces the principles and basic properties of the proposed time-resolved RATS method. Chapter 5 shows possible implementations of the RATS method into 2D measurement using SPC and proposes algorithms to obtain the FLIM spectrogram. In Chapter 6, extensive noise analysis of the method is performed, and Chapter 7 deals with approaches for direct determination of PL decay parameters (amplitudes, lifetimes) to further refine the results and speed up the postprocessing process.

2 Summary of current knowledge of the issue

2.1 Measuring methods of PL dynamics

As it was mentioned, there are many different methods for PL dynamics detection. Such methods are, for example, gated photon counting [20], a streak camera [21], a time-domain analog recording technique [22], or a frequency-domain analog recording technique [23]. However, the most commonly used method, especially due to biological sample research, is time-correlated single-photon counting (TCSPC) [24, 25].

Many of these methods can be used for FLIM, where the current focus of development is primarily on data acquisition speed. In general, the acquisition speed that the FLIM technique can achieve depends on the required signal-to-noise ratio SNR, the number of PL photons emitted from the sample, the time resolution, the method used, the efficiency of the PL collection optics, and the electronics speed.

The factors above show that the crucial parameter is the number of the emitted PL photons from the sample which hit the detector, i.e. the so-called photon budget. The photon budget can be often improved by simply increasing the intensity of the excitation signal. However, it is necessary to pay attention to the parameters of the sample, as it may destroy or bleach the PL of the active substance (so-called photobleaching) [16]. In addition, in some techniques, such as TCSPC, a higher number of photons may be redundant and will distort the resulting decay. All mentioned facts must be taken into account when choosing a suitable method.

2.1.1 Gated photon counting

Gated photon counting is the first time-domain method that has been commonly used for FLIM, and still, it counts among the standard methods [26]. This method uses gating pulses, during which the intensity of PL photons is measured. PL decay is sequentially sampled for different gate pulse delays after the excitation pulse. The limit of the gating interval, i.e. the temporal resolution, is given by the electron response of the photomultiplier, which commonly reaches 100 MHz. Several parallel gate counters can be used, and data can be acquired for all pixels at the same time. Hence, with an electrically and optically tuned system, it is possible to take a picture of 256×256 pixels in 1s for a single delay [17]. However, as it was mentioned previously, the acquisition time also depends on the measured sample (number of emitted PL photons, time resolution). Moreover, depending on the sample PL dynamics and desired temporal resolution, the optimal duration of gating pulses must be set. The method can be optimally used in the range of lifetimes of 500 ps – hundreds of ns [1].

2.1.2 Streak camera

The FLIM system based on a streak camera was first described in 2003 [27]. The principle is that the emitted PL photons are detected by a photocathode, where the emitted electrons are deflected by a rapidly changing electric field in the vacuum tube. The deflection is specific for each electron with a corresponding delay - given by the PL decay (see Fig. 1). In modern streak camera setups is used microchannel plate electron multiplier (MCP) -- for a higher gain of electrons. The deflected electrons are incident on a phosphorescent screen, which is again converting the electrons into photons recorded on a CCD camera.

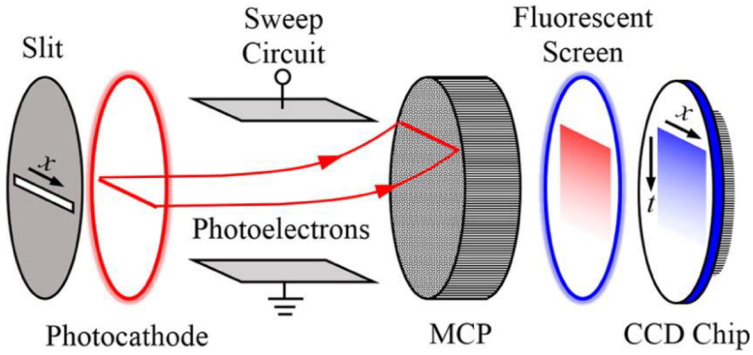

Figure 1: Principle of a streak camera. Emitted electrons (photoelectrons) from the photocathode are deflected with a sweep circuit. Deflection is specific according to the photoelectron's arrival. Adapted from Liu et al. [17], Fig. 7.

The detected PL photons in a streak camera can also be resolved spectrally (x-direction in Fig. 1), for example, through a diffraction grating. An example of such a spectrogram describing both time and spectral information is shown in Fig. 2. The optimal range of the method is similar to gated photon counting

(0.5 – hundreds of ns). However, using optimized electronics, it is possible to reach units of picoseconds [1]. So, for the single-shot measurement, the temporal resolution of a streak camera can reach even hundreds of femtoseconds.

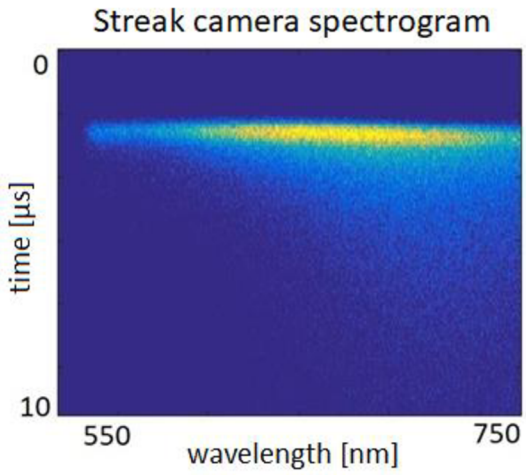

Figure 2: An example of the streak camera spectrogram, where the vertical axis can observe the PL decay of individual wavelengths (horizontal axis). Adapted from Junek et al. [46], Fig. 5(A).

2.1.3 Time-correlated single photon counting (TCSPC)

The TCSPC uses a pulsed laser to excite the sample. Typically, it employs picosecond pulses. The method principle assumes that one excitation pulse will correspond at most to one detected PL photon, which will always reach the detector at a different delay after excitation. Reaching the low number of detected PL photons can be achieved by several means. Since PL is omnidirectional, it is possible to ensure that a limited number of photons pass to the detector by selecting a suitable detection solid angle. The limited number of photons can also be done by tuning the intensity of the excitation source or by placing neutral density filters in front of the detector.

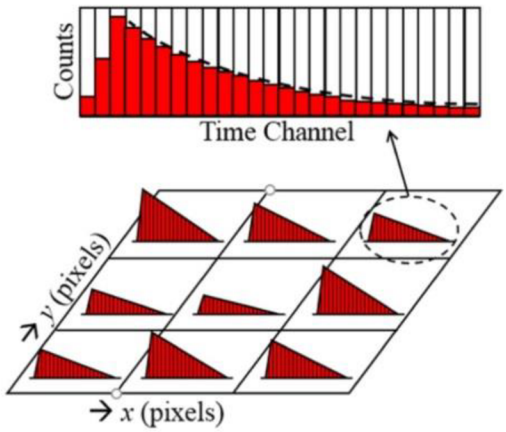

Figure 3: PL decay sensing in each SPAD pixel. Adapted from Liu et al. [17], Fig. 2(A).

If the sample is excited by a sufficient number of pulses, we get a photon detection histogram that copies the PL decay curve because the delay of PL photons follows the statistics set by the PL intensity dynamics after excitation. The acquisition time is given by the laser repetition rate, which must be selected according to the length of the expected PL decay. Therefore, the detection of microsecond PL decay can take several hours, while nanosecond PL decay can be captured within a few seconds.

This method is the most widely used approach for FLIM in biology, as PL markers with a known lifetime are used for tissue staining, and the system can be optimized for them. In addition, it is possible to use an array of avalanche diodes (SPAD), where each diode forms one pixel, and the data in them can be measured simultaneously [17]. The optimal method range is lifetimes from 0.1 ns to 100 ns [1].

2.1.4 Time-domain analog recording technique

The time-domain analog recording technique is one of the most straightforward methods, where the sample is excited by a pulsed laser, and fast electronics then directly record the PL intensity dynamics over the decay. It is often possible to use an oscilloscope or digitizer to read the PL data. In FLIM experiments using advanced electronics, image acquisition of 150×150 pixels was presented in 1s [28]. However, the detected PL decay is distorted by the excitation pulse length, which mainly affects the fast PL decay exponential components. Therefore, the method is usually used in a range of lifetimes from 0.1 to 1 μs [1].

2.1.5 Frequency-domain analog recording technique

The frequency-domain acquisition of PL decay used to be one of the most used methods but later lost its popularity, as a single measured frequency response can only describe a mono-exponential PL decay curve. In order to obtain more components of a multi-exponential PL decay curve, the measurement must be repeated with a different excitation signal configuration. This arises because the sample is excited by a sinusoidal modulated signal and uses the fact that generating a PL involves a signal phase shift and a change in signal modulation, which correspond with the present lifetime. The PL lifetimes can be determined typically in the range of 1 ns – 100 ms [1].

State-of-the-art assemblies use a fast pulsed laser on this principle and sinusoidal the detector gain [17]. The system is not suitable for experiments and samples with low PL intensity.

2.1.6 Summary of the above findings

As described above, the acquisition time for FLIM methods is a complex function of many parameters. In addition, it also depends on whether the experiment records the entire PL decay curve or only a part of it and whether the acquisition is made in all pixels simultaneously or separately [17]. Essential is also the optical technique of FLIM image recording. The choice of method depends on the required image resolution, the time resolution of the decay curve, and the type of decay (mono-exponential, multi-

exponential, non-exponential, ...). It is worth noting that the FLIM method, which is adequate for one application, may be entirely unsuitable for another.

Conventional widescreen FLIM often uses the SPAD field, which allows parallel scanning both in space and over time. Therefore, it is possible to achieve very fast measuring times in the order of seconds or even milliseconds. Such acquisition times can only be assumed for nanosecond or picosecond decays. On the other hand, the conventional approaches may be unsuitable for microseconds or sub-microseconds (hundreds of nanoseconds) decays. For example, the TCSPC acquisition time would be shifted to the order of hours. Materials that manifest themselves by microsecond or sub-microsecond PL decays include halide perovskites [8], nanocrystalline silicon [6,11], or various luminophores [29].

The need for a pulsed laser, advanced electronics, or an array of SPAD avalanche diodes makes FLIM a relatively costly analytical tool. Therefore, it is still of practical importance to come up with proposals for new approaches to measuring PL dynamics that will be robust in terms of the optical arrangement, allow coverage of a wide range of extinction times and reduce the cost of FLIM.

2.2 Compressed sensing and single-pixel camera

The concept of compressed sensing is based on the knowledge associated with signal approximation by a linear combination of a very small number of vectors in a given representation system, whose origin dates back to the 1990s [30]. The concept has become popular mainly because it is not necessary to use complete signal information, yet it is possible to reconstruct the whole signal successfully.

The concept uses the assumption that if it is possible to express the signal of interest in a base (e.g., Fourier, wavelet) where it is sparse, the sparse representation can be reconstructed even in an undetermined system. The sparsity of a signal in a certain basis denotes the fact that the signal can be expressed in this basis as a vector or a vectorized matrix, where the vast majority of elements is equal to zero. In this case, the useful information is stored in a few non-zero components. An example is an image, which can be well approximated in the wavelet basis by a sparse vector, and this fact is used in JPEG compression.

As stated above, the sparse vector can be reconstructed even from an undetermined system of linear equations. The precondition is to capture a sufficient number of random combinations of the base components. Therefore, the complete information does not necessarily need to be stored, which significantly saves data acquisition time and necessary storage capacity. Several algorithms, such as the so-called greedy or proximal algorithms, help the reconstruction [31,32].

Many measured signals are sparse on a certain basis, and therefore it is possible to retrieve them with a reduced number of measured data – respectable whether we talk about a temporal signal or an image. The theory implies that we need to scan a random combination of components of the basis where the measured signal is sparse. For instance, to reconstruct a 2D scene, i.e. an image, Fourier or wavelet

components must be scanned. An analogous approach can be used also for temporal signals. However, it is not experimentally straightforward to capture a specific random combination of wavelet components of an image. Therefore, especially in the case of 2D scene reconstruction, it is more common to use an arbitrary random pattern. This means that we can measure a random combination of pixels instead of the random combination of wavelet components. In practice, it turns out that this approach is sufficient, and it is frequently used, for instance, in the optical single-pixel camera configuration.

The single-pixel camera is the most common experiment of compressive imaging and it is frequently used. The single-pixel camera measurement can be done using only one pixel – a diode or a photomultiplier – to capture the total intensity of the image encoded by a random pattern, referred to as a mask. The total intensity needs to be measured repeatedly for a set of independent masks. The number of masks then corresponds to the number of measurements and is denoted by M. The number of pixels of the reconstructed image is denoted as N. It holds that $M<N$ and the M/N ratio determine the sensing compression ratio k, which is related to the incompleteness of the system.

Let us declare the scene, which needs to be reconstructed, as vectorized image, which is hence converted into vector x featuring size N. Then we define the matrix A, where each row of the matrix is a single vectorized 2D random mask. After M measurements (M different masks), the dimension of the matrix A is $M \times N$, where $M<N$, *i.e.* we attain an undetermined system of linear equations. As mentioned, for each mask, we measure one total intensity of the scene, which together forms the vector y with a size of M. The measured intensities can be expressed via matrix multiplication as $y = Ax$. This expression cannot be solved for an undetermined system, but including a suitable regularization parameter ϕ ensures that minimization finds the correct solution:

$$min\left\{\left\|Ax - y\right\|_2 + \phi(x)\right\}. \tag{1}$$

The roots of the single-pixel camera can be dated back to 2005 [33]. Since then, it has found utilization in various imaging domains, especially in spectral regions, where 2D detectors are difficult to access – infrared or even terahertz optics. Moreover, it is possible to use SPC to replace even high-speed detectors (SPADs, iCCD, high-speed cameras) used to sense very fast processes. However, in this case, the measured phenomenon must be recurring.

Nevertheless, the essential factor enabling high-quality reconstruction is the signal-to-noise ratio SNR of the detected signal. It is necessary to keep in mind that the detected signal in a single-pixel camera experiment is a randomly fluctuating value around a certain mean value. The higher the number of pixels, the lower the relative level of fluctuations due to statistical reasons. Since small variations in the measured value carry useful information, noise can easily overwhelm the signal. Therefore, the SNR should be taken

into account during the construction of a setup – especially in infrared or terahertz regions of the spectrum. The effect of noise also depends on used reconstruction algorithm.

The single-pixel camera setup can be constructed in two modes - structured detection mode or structured scene illumination mode, i.e. one can either apply the random mask on the detected image or on the scene illumination, respectively. The choice depends primarily on the application.

The random mask is most commonly generated using a digital micro-mirror device DMD, which ensures appropriate resolution. An advantage of using DMD is the ability to impose an arbitrary binary pattern to encode the image. Apart from random mask patterns, it is also appropriate to use Hadamard or Fourier-based patterns, which can provide image retrieval with a lower compression ratio [34].

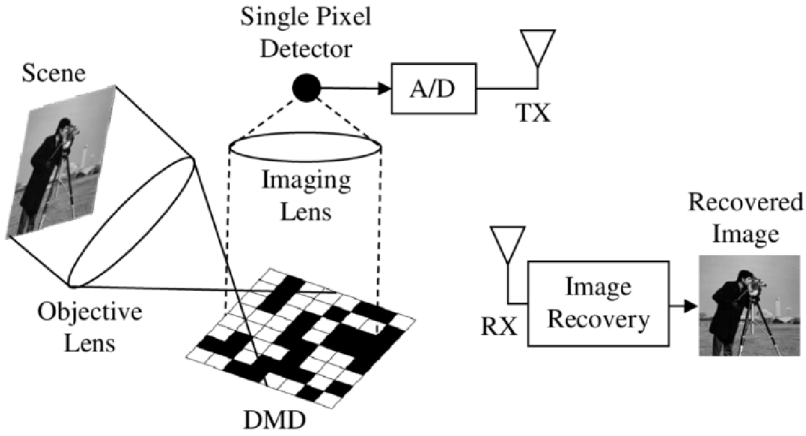

Figure 4: Scheme of the single-pixel camera principle. Adapted from Don et al. [35], Fig. 6.

2.3 Compressed sensing and deep learning in PL dynamics measurements and FLIM

Compressed sensing (CS) has expanded into many applications, but it has been successful, especially in the fields where it is difficult to access a 2D detector (see Section 2.2). Since, in this work, we are interested mostly in the visible region of the spectrum, it may seem that high-speed cameras would be enough. However, available frame rates for high-speed cameras reach tens of kHz, which is by far inappropriate for PL decays in nanosecond and microsecond timescales. Moreover, the number of emitted PL photons depends on a measured sample and most often, the intensity is not detectable with standard CCD or CMOS detectors. Therefore, gated 2D array detectors, such as SPAD or iCCD are widely used in FLIM implementations. Nevertheless, it is a highly costly solution and is not implementable to all-time resolved methods.

To eliminate the demands of the cost, it is possible to substitute a 2D array detector with a single fast and sensitive detectors like an avalanche diode or photomultiplier (PMT). Both are frequently reachable as a 0D detector, i.e. a single-pixel detector. The most straightforward option is to measure in a raster mode

that is, however, time-consuming – particularly for the long integration time required for the low intensities. Nevertheless, using the principles of CS, such as a single-pixel camera, it is necessary to acquire a lower number of measurements given by the compression ratio. Hence, the total acquisition time is shortened.

One of the first ideas of CS application in time-resolved measurement is connected with compressive hyperspectral fluorescence microscopy research, where CS was used for fluorescence imaging extended to a spectral domain, i.e. reconstruction of a spectral 3D datacube (x,y,$\boldsymbol{\lambda}$). Nevertheless, the similarity of the reconstruction of a spectral 3D datacube (x,y,$\boldsymbol{\lambda}$), i.e. hyperspectral imaging, and time domain 3D datacube (x,y,t) was discussed [36].

The idea of 3D datacube reconstruction (x,y,t) was implemented and optimized in combination with hyperspectral imaging, where FLIM was performed on a 16-channel time-resolved spectrometer (each channel represented one PMT). Each channel was taken as one SPC, so the reconstruction took place in parallel on each channel [37]. This approach effectively created a 4D dataset, where for each pixel, one attains the PL decay in 16 different spectral regions.

The same research group subsequently states that reconstruction (post-processing) is time-consuming, reaching about 4 hours. This large data post-processing is caused by the fact that in each temporal frame are 16 images, which need to be retrieved separately. Therefore, the authors came up with a solution using a neural network, which has a compression-scanned 3D datacube as an input. The neural network is called Net-FLICS and it was trained on simulated data. Nevertheless, it was proved to perform well even in a real experiment. The Net-FLICS training took 4.5 h, but, in the end, it shortens the total reconstruction results to the order of seconds [38]. This example illustrates the power of using neural networks to process CS-based datasets.

However, the above-mentioned approaches can only capture a repetitive phenomenon with a stable repetitive PL decay over the acquisition time since each mask needs to be scanned ideally under the same conditions. In the above-mentioned articles, the total measurement time is stated to reach tens of minutes [37,38]. For some less stable samples, such acquisition times can be problematic. Therefore, in parallel to the given approach, the possibility of using a compressive method based on shearing in the time domain called Single-shot compressive ultrafast photography CUP was investigated [39,40]. This experiment is based on a different CS approach, where a 3D datacube can be captured in a single snapshot by using a 2D detector. CUP implementation to FLIM is connected with a principle of a streak camera. The key property is that an image encoded by a single mask is sheared in the time domain on a 2D detector. Thus, in each time point, we have one mask imaged on a different area of a detector, and the total intensity is given by the sum of overlaying encoded images from all time points. The reconstruction of the scene is therefore possible from a single 2D image encoded by a single pattern (mask). Therefore, it is possible to measure unstable PL samples using the CUP approach and assuming a sufficiently recurring phenomenon (PL

decay) is not necessary. Due to the nature of the CUP experiment, the method is well suited for simple scenes featuring a high-intensity level.

Apart from FLIM spectrogram (2D scene) reconstruction, CS makes it possible to directly determine the parameters of multi-exponential decays. So far, the direct determination of lifetimes via CS has been verified only via simulations for the TCSPC method [41]. The direct reconstruction of decay parameters (amplitudes and lifetimes) is possible in TCSPC due to the principle of the method (see Section 2.1.3). Namely, the idea of a reconstruction algorithm uses the properties of the Poisson distribution when it is assumed that the photon detection is sparse at a given time channel [41]. The approach primarily replaces standard PL decay fitting because it can be imprecise and often needs an experimenter's input to ensure a physically correct solution.

However, the paradigm of replacing fitting with a CS algorithm has gradually begun to be substituted by deep learning and neural networks (NN). The NNs can be efficiently trained using artificially simulated data and provide FLIM with a fast alternative to the previously used lifetime and image retrieval. The first possibility is to analyze the time signal (PL decay). This was reported by Zickus et al. by using a time-gated SPAD camera when the lifetime τ for each pixel was determined using NN. However, the authors assumed a mono-exponential decay and considered a fully-connected system of NN [42]. Instead of analyzing individual time signals separately, another option is to insert a 3D image as the input of the NN. Since one attains a scene "photo" at each time point using TCSPC, the method creates a 3D image and the lifetime of each pixel can be determined from all voxels using convolutional neural networks (CNN). This approach was verified on real experimental data [43]. However, this approach requires using an expensive 2D SPAD detector to capture the temporal snapshot at each timepoint and, with respect to this thesis, this data processing is not primarily connected with CS.

To summarize the information, should the user need to measure unstable PL phenomena, it is necessary to use fast data acquisition. This can be achieved using the single-shot compressive ultrafast photography CUP implementation, which can only be implemented for the streak camera. Alternatively, TCSPC or gated-photon counting methods with the use of an expensive 2D array of SPAD detectors or iCCD (non-compressive method) are characterized by similarly fast acquisition. Here the acquisition of the 3D datacube allows for the possibility of extracting the PL decay parameters using trained NNs. Standard CS principles can hardly compete here due to the time of measurement and post-processing (reconstruction). Apart from CUP, there is no suitable way for single-shot measurement of unstable PL phenomena. In the case of studying stable PL phenomena or in instances where the 2D array of SPAD detectors cannot be used, it is advantageous to avoid raster mode and use the single-pixel camera principle (SPC).

SPC saves measurement time due to a lower number of measurements given by the compression ratio. At the same time, it reduces the SNR due to the fact that we measure a sum of light emitted from many pixels. The results can be consequently analyzed via frame-by-frame reconstructions, or they can be reconstructed as a 3D datacube (x,y,t). In the case of TCSPC, the aforementioned Net-FLICS can be also used for reconstruction.

Although the existing approaches seem to cover the issue of FLIM, there are several notable gaps in the current instrumentation and data processing. There is an ongoing search for more versatile methods able to (I) cover a broader range of photoluminescence timescales, (II) measure samples with long-lived PL decay, (III) measure samples without any prior knowledge about the PL decay, and (IV) keep a reasonable cost of the experimental setup.

The reconstruction CS algorithms are lively studied as well since the standard approach is often extremely computationally demanding. Therefore, it is still necessary to come up with new solutions that eliminate, for example, the need for reconstruction of the entire 3D datacube (x,y,t) or implement deep learning that would cover the outputs of the whole spectra of time-resolved methods (see Section 2.1).

3 Goals definition based on the analysis of the current state-of-the-art

Based on the issues identified in the previous chapter, we have set the goals for the thesis:

1. Design a robust approach to measuring PL dynamics that eliminates the need for prior knowledge of the PL sample.

   Considering the conclusions of Section 2.1, it is most often necessary to consider the appropriateness of the given time-resolved method before the actual measurement of the given sample. We also often need to have some prior knowledge about the PL of the sample and set the parameters of the measurement method accordingly. To provide an example, the presence of a long-lived PL component makes TCSPC measurement extremely time-consuming and such samples need to be measured by a different FLIM method. Therefore, finding an approach that eliminates these assumptions would mean a significant simplification of the field.

2. Apply the novel approach to 2D PL lifetime imaging (FLIM) using compressed sensing techniques and define a reconstruction algorithm of the FLIM spectrogram with low post-processing time.

   As stated in the conclusions of Section 2.3, it is beneficial to substitute a raster mode with an SPC configuration because of shortened measuring time (depending on the compression ratio). However, such an approach suffers from the time cost of post-processing (FLIM spectrogram reconstruction). Therefore, it is advisable to come up with a new solution in the form of an algorithm, where it will not be necessary to reconstruct the entire 3D datacube (x,y,t).

3. Analyze the method in terms of noise dependence and compare the stated reconstruction algorithms of the FLIM spectrogram.

   Noise dependency analysis is a crucial parameter of each method, giving an overview of its utilization. Describe possible ways to suppress noise effect to results and compare stated algorithms of FLIM reconstruction.

4. Analyze the possibility of using the compressed sensing technique to directly determine multi-exponential decay parameters (amplitudes, lifetimes).

   Direct determination of decay parameters would avoid fitting and refine FLIM spectrogram reconstruction. In accordance with the conclusion of Section 2.3, investigate direct parameters determination using an undetermined system and NN.

In the following Chapters of the text are presented only the own results solved within the Ph.D. studies that pursue the above-stated goals.

4 RATS method

4.1 Introduction

In general, all methods for detecting PL dynamics can be divided into two groups -- those that measure in the time domain and those that measure in the frequency domain. Time-domain methods require a light source that generates corresponding short pulses that excite the PL. At the same time, fast detection or gating electronics are needed. The frequency-domain measurement of PL decay requires a controllably modulated light intensity, such as an acoustic-optical modulator or an intensity-modulated laser. In order to capture PL decay at different time intervals, intensity must be possible to modulate over a wide range of frequencies.

The core of this thesis lies in creating a novel RATS method which can bypass some of these requirements and represents a robust and low-cost solution. The basic idea of this method is to excite the measured sample with randomly fluctuating light intensity. Such a random excitation signal is characterized by a wide range of frequencies, which is a primary advantage in PL decay reconstruction.

In this section, we describe the basic principles behind this method and propose two possible ways of random signal generation, which lead to an entirely different character of the random excitation signal. Based on the choice of the generator, possible optical setups for single-point measurement (0D-RATS) will be shown. The following parts of Section 4.5 then present basic properties of the RATS method, such as the method's robustness towards mutual shift or offset of excitation and PL signals. It is also necessary to discuss the effect of excitation signal periodicity and the parameters affecting the impulse response function (IRF) of the measurement system. All the mentioned properties are freely transferable to 2D-RATS, which will be the subject of the next Chapter.

4.2 Principles of the RATS method

The principles of the RATS method consist of the excitation of the measured sample with a random excitation signal I_{EXC}, which generates a PL signal on the sample, which we designate as I_{PL}. The I_{PL} signal also has a random character because it is given by the convolution of I_{EXC} and I_D according to Eq.(2), where I_D represents the PL decay curve:

$$I_{PL} = I_{EXC} * I_D. \tag{2}$$

It is necessary to mention that Eq.(2) is valid only for the PL intensity, which is linearly proportional to the excitation intensity.

Because of using a signal with a random character, we get a wide range of frequencies in Fourier space. Therefore, an arbitrary shape of I_D can be calculated from a single measured dataset, including multi-

exponential or even non-exponential decay. Eq.(3) shows the deconvolution used with the so-called Tikhonov regularization [44]. The parameter ε controls the ill-conditioned cases where the denominator would approach zero.

$$I_D = Re\left\{ F^{-1}\left[\frac{F\left(I_{PL}\right) F^{*}\left(I_{EXC}\right)}{F\left(I_{EXC}\right)F^{*}\left(I_{EXC}\right)+\varepsilon\overline{F\left(I_{EXC}\right)F^{*}\left(I_{EXC}\right)}} \right] \right\}. \tag{3}$$

The RATS concept can be illustrated by the simulated data shown in Fig. 5. The excitation signal, plotted in blue in Fig. 5(A), was obtained by simulating speckle patterns created via a rotating diffuser using Fraunhofer diffraction [45]. The principle of random signal generation via a rotating diffuser is mentioned in Section 4.1.3 and described in the article attached to the thesis [46]. The photoluminescence signal I_{PL} plotted in Fig. 5(A) in red, was calculated using Eq.(2).

For the sake of clarity, the PL decay curve in Fig. 5 was chosen to be mono-exponential with a lifetime $\tau = 50$ µs, so that the difference between the excitation and PL signals is apparent both in the time domain (A) and in the Fourier space (B). The Fourier transforms of I_{EXC} and I_{PL} are shown in Fig. 5(B). Fig. 5(C) shows the PL decay curve I_D reconstructed using Eq.(3).

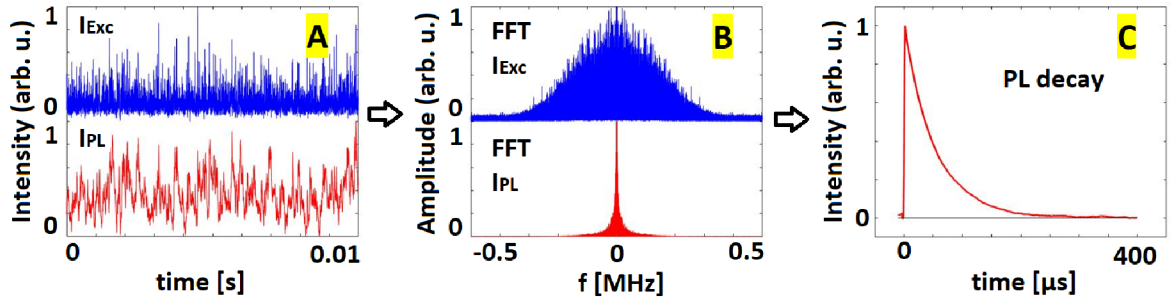

Figure 5: Sequence showing the principle of I_D evaluation by the RATS method. A) Simulated time-modulated I_{EXC} signal (marked in blue) and detected PL signal I_{PL} (marked in red) resulting from mono-exponential decay ($\tau = 50$ µs). B) Fourier transform amplitudes of I_{EXC} (marked in blue) and I_{PL} (marked in red). C) Reconstructed I_D using Eq.(3). Adapted from Junek et al. [47], Fig. 1.

4.3 Random signal generation

In the following subsection, two approaches to the generation of random excitation signals are presented. Since the two methods create a different character of the signal, simulated data are used to demonstrate that both approaches lead to the same retrieved PL decay.

4.3.1 Diffuser-based signal generator

One way to generate a random signal is to transmit a coherent beam of light through a rapidly changing scattering element (rotary diffuser). This approach creates randomly varying interference patterns (see Fig. 6), which we refer to as laser temporal speckles. The field of temporal speckles is cropped by the iris aperture, which gives rise to a random intensity fluctuation in time. This fluctuating signal can be then used to excite the sample. In the diffuser-based RATS experimental setup, any coherent light source can be used to excite the PL.

So far, the diffuser-based RATS technique has been successfully used to measure PL decay in the sub-microsecond region, where it has been verified with conventional approaches to measuring PL decay, such as a streak camera or TCSPC [46, 47]. This approach we call random analog signal.

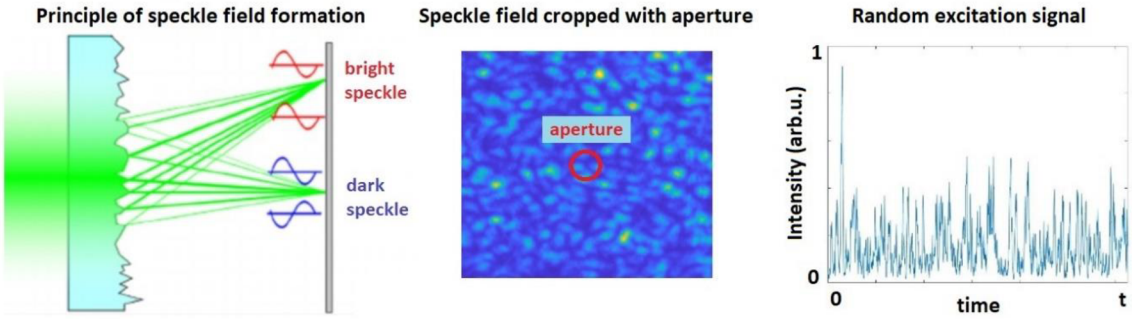

Figure 6: The principle of random signal generation. Left part: An interference speckle pattern formation behind the optical diffusor. Middle part: An example of a speckle pattern with an aperture indicated. Right part: An example of a randomly modulated signal generated by the generator described above.

4.3.2 Laser modulation-based signal generator

The second way to generate a rapid random signal is using a digital random laser modulation, where a rectangular signal with a random duty cycle is generated. The modulation signal is produced by the development kit Digilent Cmod A7 and was generated in the FPGA Xilinx Artix-7 (VIVADO software package). The bitstream is generated via Linear Feedback Shift Register (LFSR) from flip-flops and XNOR gate feedback, configured in FPGA. The output of the LFSR meets many randomness tests [48].

An example of a randomly modulated digital signal is shown in Fig. 8, where a short interval of 0.5 ms is zoomed. Using a modulatable diode laser (Cobolt S06-01 – modulation up to 150 MHz), it is possible to obtain the resolution in units of nanoseconds. Details of the digital random signal generation are presented in Junek et al. [49].

4.3.3 Verification of both random signal generators

Fig. 7 and Fig. 8 present a simulation that verified the possibility of applying both analog and digital random signals. The simulations used a bi-exponential decay I^0_D (see Eq.(4)) with parameters $A_1 = 1$, $A_2 = 15$, $\tau_1 = 40$ µs and $\tau_2 = 5$ µs.

$$I^0_D = A_1 e^{-t/\tau_1} + A_2 e^{-t/\tau_2}. \tag{4}$$

The width w (FWHM) of an impulse response function (IRF) for random digital signal was $w_D = 1.45$ µs and for random analog signal was $w_A = 2.07$ µs. In order to get a rigorous comparison, the I^0_D curve obtained using the random digital signal was convolved with the Gaussian function $G(w)$ with an FWHM w equal to the root mean square difference of w_A and w_D values:

$$I_D = I^0_D * G\left(\sqrt{w_A^2 - w_D^2}\right). \tag{5}$$

This step ensured that the resulting IRF width was the same for both analog and digital cases.

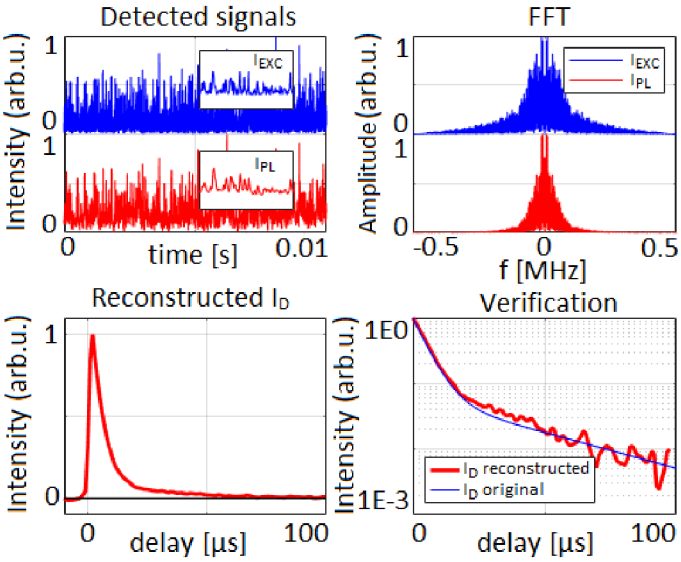

Figure 7: Left upper panel: Analog random excitation (blue line) and PL (red line) signal in time. Right upper panel: amplitudes of Fourier components in the excitation (blue line) and PL (red line). Left lower panel: retrieved PL decay curve in a linear scale. Right lower panel: retrieved PL decay (red line) compared to the original decay (blue line) in a semilogarithmic scale. Adapted from Junek et al. [49], Fig. 3.

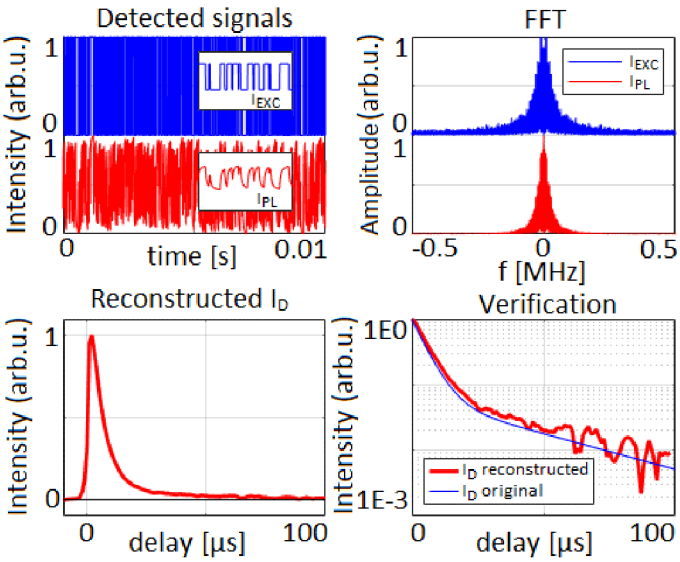

Figure 8: Left upper panel: Digital random excitation (blue line) and PL (red line) signal in time. Right upper panel: amplitudes of Fourier components in the excitation (blue line) and PL (red line). Left lower panel: retrieved PL decay curve in a linear scale. Right lower panel: retrieved PL decay (red line) compared to the original decay (blue line) in a semilogarithmic scale. Adapted from Junek et al. [49], Fig. 2.

Our results confirm that an arbitrary random signal can be used to excite the sample in the RATS method and both analog and digital forms of the random signal are able to successfully retrieve the PL decay.

4.4 Optical setup (0D-RATS)

In general, the RATS method does not require any significantly expensive elements, and due to its simplicity, there is no need for complicated adjustment or calibration of the optical arrangement. Moreover, the method is resistant to various experimental problems, such as signal delay or signal offset, described in the following Section 4.5. Experimental implementations of the RATS method were built with the vision of a simple, low-cost setup to preserve these major advantages of the method.

4.4.1 Diffuser signal generator-based optical setup

A diagram of the optical setup using a random analog signal is shown in Fig. 9. In general, any coherent light source suitable for sample excitation can be used as the excitation source. An essential part of the optical arrangement is the random signal generator, which consists of three components – a focusing lens, a rotating diffuser, and an aperture. The beam is focused onto a diffuser, generating a speckle pattern. The parameters of the used components affect the size of individual speckles and the rate of their variation.

Optimization can be achieved by controlling the focused beam spot size and choosing the grain size of the diffuser. The field of speckles is subsequently cropped with an aperture. The aperture size affects only the modulation depth of the resulting I_{EXC} signal, not its frequency range. The frequency of the rotary diffuser is directly proportional to the highest frequency of the I_{EXC} signal in Fourier spectra.

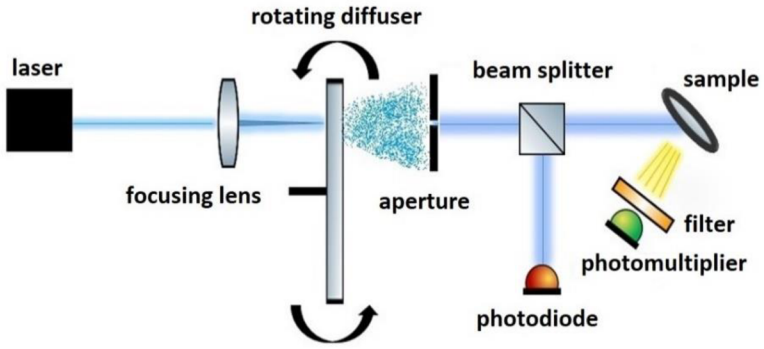

Figure 9: Schematic of the used optical arrangement for single-point 0D-RATS measurement. Adapted from Junek et al. [46], Fig. 2.

The output beam from the generator was divided by a beamsplitter into the reference branch, where the I_{EXC} was detected via a photodiode. The transmitted part of the beam was directed to the measurement branch. Here, the sample was excited by the random temporal signal and the emitted I_{PL} was detected using a photomultiplier. A colour filter was used to block the scattered excitation light not to reach the photomultiplier.

A significant drawback of the diffuser-based optical arrangement is the optical efficiency of using the excitation intensity, which reached in our setup 0.1% -- dominantly due to the random signal generator based on the diffuser, where the iris aperture blocks the vast majority of the excitation light.

More information about the properties of the optical setup used for the verification measurement can be found in the published article by Junek et al. [46].

4.4.2 Digital signal generator-based optical setup

In the case of using a random digital signal (see Section 4.3), the optical setup is significantly simplified, as can be seen from Fig. 10. In addition, the optical power efficiency is increased and depends purely on the properties of a used beamsplitter (BS). In the case of BS 50:50 and by using the digital random signal generation, we were able to improve the efficiency by 500 times compared to the analog case without any major optimization of the setup.

In the case of digital random signal generation, the laser was directly modulated, which we described in detail in Section 4.3.2. All other aspects of the setup remained the same as for the analog signal generation.

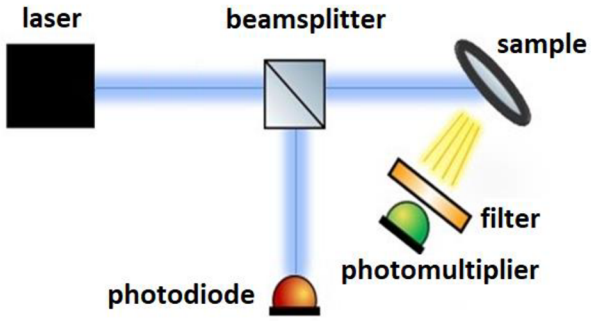

Figure 10: Schematic of 0D-RATS optical setup based on random digital modulation.

4.5 Properties of the RATS method

Due to the use of a random signal, the RATS method can be used to retrieve an arbitrary multi-exponential I_D curve or even a non-exponential PL decay. Both excitation and PL signals (I_{EXC} and I_{PL}, respectively) have to be detected to carry out the reconstruction of PL dynamics. Nevertheless, it is not necessary to attain careful timing of the signals. The mutual temporal shift of the so-called "zero time" between the PL and the excitation data will only cause the decay of the PL to be multiplied by a constant complex number $e^{-i\varphi}$, where the phase φ will be scaled according to the corresponding time difference.

At the same time, the offset value present in the signals (the shift along the y-axis) is only reflected at the zero frequency of the Fourier transform and can again be avoided by removing low frequencies from the extinction reconstruction. Both the temporal shift and offset of the signals are discussed in Section 4.5.1. It is worth noting that all presented results in the attached papers were obtained without any timing or background correction [46,47,49,50].

At the same time, the RATS method – as a method based on the deconvolution of a signal – is sensitive to the periodicity of the random excitation signal. This feature is discussed in detail in Section 4.5.2. Finally, we focus on the attainable temporal resolution of the setup in Section 4.5.3. There, we discuss the instrument response function width for both presented methods of signal generation and the major factors governing the attainable temporal resolution.

4.5.1 Influence of the mutual shift of the excitation and PL signal

We can demonstrate the robustness of the RATS method against the signal temporal shift and offset on simulated data. In Fig. 11, we depict the reconstruction of simulated data for τ = 1 ms, where the mutual delay between the PL and the excitation signal (see panel 11(A)) and the offset in the background of the I_{EXC} and I_{PL} signals (see panel 11(B)) have been added.

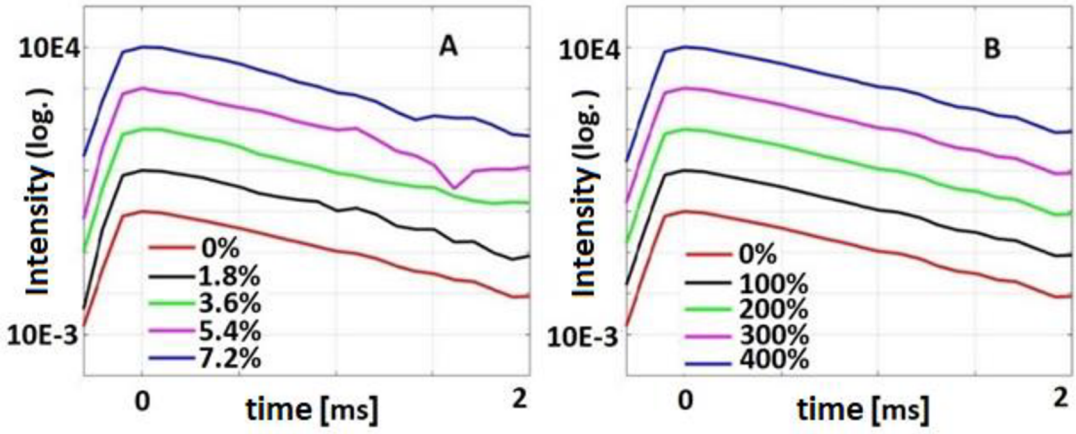

Figure 11: Effect of mutual delay and background offset of I_{EXC} and I_{PL} signals on the reconstructed I_D. The reconstruction was made for different delays between the PL and the excitation signal (panel A). Relative delay (0-7.2%). The same data were reconstructed for several offsets in the PL intensity signals (panel B). The relative offset (0-400%) is given relative to the amplitude of the PL signal. All curves are artificially vertically shifted and displayed on a semi-logarithmic scale for better comparison. Adapted from Junek et al. [46], Fig. 6.

The signals were delayed by up to 7.2% compared to the total acquisition time without any significant observable effect on the reconstructed decay curve (see panel 11(A)). Analogously, a signal shift of up to 400% of the original signal amplitude did not affect the reconstructed PL decay curve (see panel 11(B)). For the sake of comparison, the extinction curves are shown on a semi-logarithmic scale and stacked with a constant vertical shift.

4.5.2 Periodicity of the excitation signal

The approach to the generation of a random analog signal based on a rotary diffuser can be problematic due to the periodicity of the I_{EXC}. In particular, the excitation signal I_{EXC} periodicity can introduce artifacts due to the deconvolution properties. From the nature of the deconvolution in Eq.(3), it follows that the periodic waveform of the excitation leads to a periodic I_D signal with an amplitude distributed between the periodic replica of the PL decay. Therefore, the amplitude of the retrieved PL signal is correspondingly reduced, while the noise present in the data remains the same.

In Fig. 12, we compare the entire deconvolved I_D dataset in the case of a non-periodic I_{EXC} signal of duration 0.1 s (left side) and a periodic I_{EXC} signal (7 periods) with the same total duration of 0.1 s. Their comparison shows that the amplitude for the periodic signal I_{EXC} is about seven times smaller compared to the non-periodic case. If the result is normalized and if we are in a noise-free system, periodicity will not introduce any distortion in terms of the overall dynamics of PL decay. However, if we consider a noisy I_{PL}

signal (e.g., 3% as in Fig. 12), the periodicity of the signal will be reflected by the reduction of the signal-to-noise ratio in I_D, which will be reflected in the smoothness of the curve (see Fig. 13).

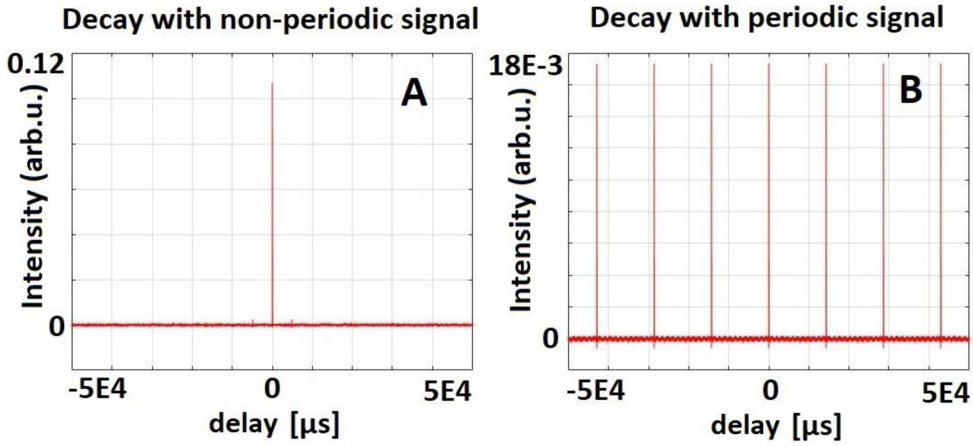

Figure 12: I_D reconstruction results using non-periodic I_{EXC} (panel A) and periodic I_{EXC} (panel B). Expected lifetime $\tau = 20$ µs. Image adapted from Junek et al. [50], Fig. 4.

Fig. 13 was created by zooming in on Fig. 12 on the time axis. As mentioned, the periodicity of the excitation signal results more noisy curve, which can be observed in Fig. 13(B). The root mean square error for the curve in Fig. 13(B) reaches RMSE = 29.7×10^{-3}. While in the case of a non-periodic excitation signal with the same noise level in I_{PL} (3%), it reaches RMSE = 12.9×10^{-3}, i.e., more than 2× lower (Fig. 13(A)). The results show that a higher signal-to-noise ratio can be achieved by using a non-periodic signal.

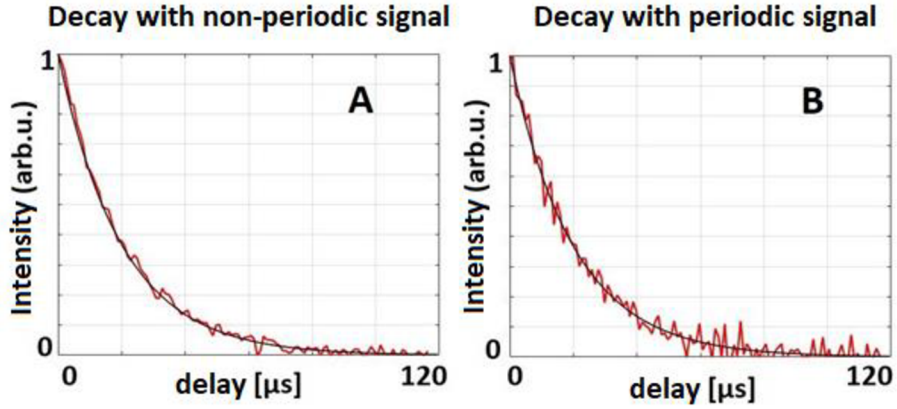

Figure 13: Zoomed I_D reconstruction from Fig. 12 ($\tau = 20$ µs). (A) I_{EXC} as a non-periodic signal. (B) I_{EXC} as a periodic signal (7 periods). The reconstructed data are shown in red; the reference data are in black. Reconstruction with a noise level of 3% in the I_{PL} signal (corresponding to an SNR of about 15.2 dB).

A non-periodic signal is difficult to achieve using the periodic rotation of the diffuser. However, the periodicity of the excitation signal can be entirely avoided by using a modulated laser (random digital

modulation), which can fully replace the analog generator of the random excitation signal (see Section 4.3.2).

4.5.3 Impulse response function

The decisive parameter of PL dynamics spectroscopy is the temporal resolution of the method. This is characterized by the width of the impulse response function (IRF) method. The IRF in a given optical system can be determined by measuring a sample where the PL decays much faster compared to the expected IRF width.

I. IRF of the diffuser-based optical setup

The IRF of the diffuser-based optical setup was measured using a solution of Rhodamine 6G, which has a PL decay time in units of nanoseconds [51]. This value is safely below the resolution of the method and can be considered as "infinitely" fast. The IRF width was then determined as the full width at half maximum (FWHM) of the calculated I_D.

In the case of the RATS method, the IRF width is mainly affected by the modulation rate of the I_{EXC} signal, which is related to the speed of temporal fluctuation of the speckles. It can be shown that the width of the IRF is inversely proportional to the peripheral velocity of the diffuser v. It can also be observed that the width of the IRF decreases with decreasing mean grain size g and also with decreasing laser spot size d, which can be affected, for example, by choice of the focusing lens. This fact can be represented by the function $h(g,d)$. The prescription of the function $h(g,d)$ has not yet been described in more detail. For clarity, Eq.(6) is presented.

$$FWHM_{(IRF)} \propto \frac{h(g,d)}{v}. \tag{6}$$

Fig. 14 demonstrates the dependence of the experimentally measured IRF width with respect to the increasing frequency of the rotary diffuser, which is inversely proportional to the peripheral speed of the diffuser.

The results presented in Fig. 14 were attained for the width of the focused beam at the diffuser surface was approximately 50 μm, the spot of the beam on the diffuser was 50 mm from its center, and the average grain size g was about 8 μm.

However, in the following experimental campaign, significant progress was achieved towards the optimization of the IRF of analog temporal speckles. The diameter of the focused beam was reduced to 2.3 μm, the diameter of the rotating diffuser was 125 mm, the average grain size was around 4 μm, and the rotating frequency of the diffuser reached 230 Hz. In such an arrangement, an IRF width = 45 ns was obtained.

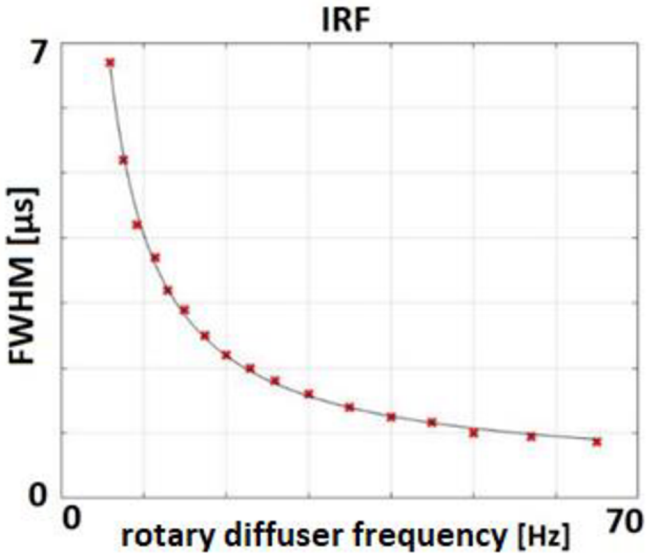

Figure 14: Experimentally measured FWHM dependence of the impulse response function for different diffuser rotation frequencies (red crosses) fitted with a reciprocal function (black line). Adapted from Junek et al. [46], Fig. 3.

II. IRF of the laser modulation-based optical setup

Since the digital modulation of the laser speckles aimed at reaching nanosecond timescale, we used scattered excitation light from white paper as the detected fast signal. The measurement was carried out at five laser modulation frequencies (12, 24, 48, 96, and 120 MHz) when the selected modulation frequency corresponded to the fastest bit of the random bitstream pattern. The change in the modulation frequency applies only to the duration of the duty cycle.

Since the digital modulation creates a rectangular signal, the signal contains, in addition to the carrier frequency, several significantly higher frequencies related to the steepness of the leading and falling edges. Therefore, when determining the IRF, the sampling frequency played an important role.

The sampling frequency was always chosen to fulfil the Shannon-Nyquist theorem for carrying frequencies of the fastest bit of the signal. Data were read using Handyscope TiePie HS6-1000XM with a maximum sampling frequency of 500MS/s for each channel (simultaneous measurement on two channels). In the case of the sampling frequency of 500 MS/s and the laser modulation frequency of 120 MHz, we achieved an IRF width of around 6 ns. The results for all modulation and sampling frequencies are summarized in Fig. 15.

The results reveal greater importance of the sampling frequency than the modulating frequency. By using a digitizer with even faster modulation than 500 MS/s, it might be possible to achieve smaller IRF width for the same modulation frequencies and thus get a better temporal resolution. By employing the best

settings within our setup, we were able to reach the IRF width of 6 ns, which is approximately an order of magnitude improvement compared to the analog mode of temporal speckles generation.

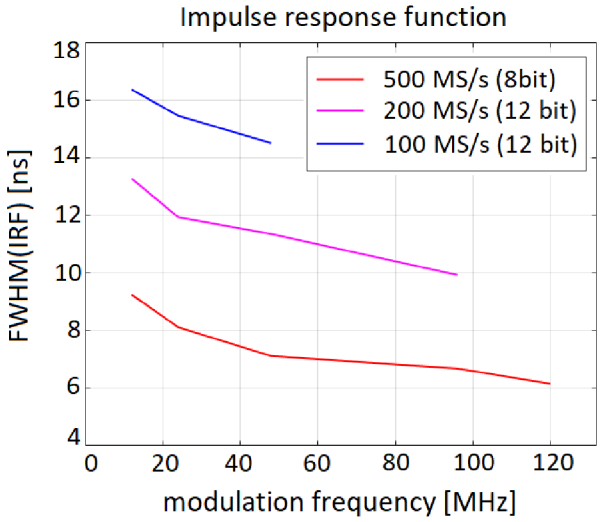

Figure 15: IRF measurement for different modulation frequencies and different sampling frequencies. Adapted from Junek et al. [49], Fig. 9.

5 2D-RATS

The RATS approach to the PL decay measurement can also be used for 2D fluorescence lifetime imaging (FLIM) via several possible implementations. This thesis was directed towards compressive imaging and the single-pixel camera (SPC) configuration, which provides the advantage of the reduced number of measurements. Therefore, the SPC implementation will be discussed in detail. Nevertheless, sample scanning or other approaches can be implemented with the RATS method as well. The SPC data can be processed and evaluated via two different approaches, which were introduced in recent papers by Junek et al. [47,49], and they are described in Sections 5.1 and 5.2.

In the SPC implementation of RATS, the sample is illuminated by a set of random excitation patterns (masks). The intensity of excitation masks fluctuates globally in time so that all pixels are excited with the same temporal waveform $I_{EXC}(t)$. The detected PL intensity corresponds to the sum of PL from all illuminated spots in the sample. Therefore, it can be detected by a single-pixel detector. The I_{PL} signal is then given as the sum of the sub-signals $I_{PL}(i)$ from individual pixels, and Eq.(2) can then be rewritten for the total PL intensity as:

$$I_{PL} = \sum_{i=1}^{n} I_{PL}(i) = I_{EXC} * \sum_{i=1}^{n} I_D(i). \tag{7}$$

The number of excitation masks M is given by the total number of image pixels N and the so-called compression ratio $k = M/N$. Since the masks are not coherent, i.e., they are random to each other, each mask illuminates a different combination of sample points, and therefore each individual mask leads to a specific I_{PL} signal. Following the 0D-RATS retrieval of the PL decay, here it is possible to extract the PL decay I_{DA} for each mask as:

$$I_{DA} = Re\left\{\mathbb{F}^{-1}\left[\frac{\mathbb{F}\left(\sum_{i=1}^{n} I_{PL(i)}\right)\mathbb{F}^{*}\left(I_{EXC}\right)}{\mathbb{F}\left(I_{EXC}\right)\mathbb{F}^{*}\left(I_{EXC}\right)+\varepsilon\overline{\mathbb{F}\left(I_{ECX}\right)\mathbb{F}^{*}\left(I_{EXC}\right)}}\right]\right\}. \tag{8}$$

As a result, we attain M different PL decays I_{DA}, which corresponds to M different masks.

Two different approaches to FLIM spectrogram reconstruction are described and demonstrated. Both approaches diverge in the steps following Eq.(8). The approach described in Section 5.1 is the originally used procedure, which was described in the article by Junek et al. [47] and is very similar to other works [37]. For the purpose of this work, this approach will be denoted as FLIM_B to follow the notation from Junek et al. [49].

The approach presented in Section 5.2 is an alternative approach with a direct reconstruction of PL amplitude maps corresponding to individual PL lifetimes τ. This alternative approach takes more advantage of compressed sensing and significantly saves postprocessing time. The approach was first time introduced in the article by Junek et al. [49] and, for the purpose of this work, will be denoted as FLIM_A.

5.1 FLIM_B reconstruction approach

As stated in Section 5 introduction, the number of calculated PL decay curves I_{DA} corresponds to the number of used masks M. By considering the data from the point of view of mask number, the set of all I_{DA}s provides us with the PL intensity fluctuations at any delay after excitation – see Fig. 16(B). By plotting the intensity fluctuation only at a single delay, we obtain the I_{SPC} signal, where the number of I_{SPC} values corresponds to the number of used masks M (Fig. 16(C)). Using the knowledge of I_{SPC}, the known pattern of the used masks, and compressed sensing algorithms, the PL image $m(t)$ corresponding to the given delay after excitation can be reconstructed. The reconstruction is done via minimization according to Eq.(9).

$$min\left\{\left\|Am(t) - I_{SPC}\right\|_2^2 + TV(m(t))\right\} \tag{9}$$

The matrix A is created from the vectorized random masks used for the sample excitation. TV stands for total variation.

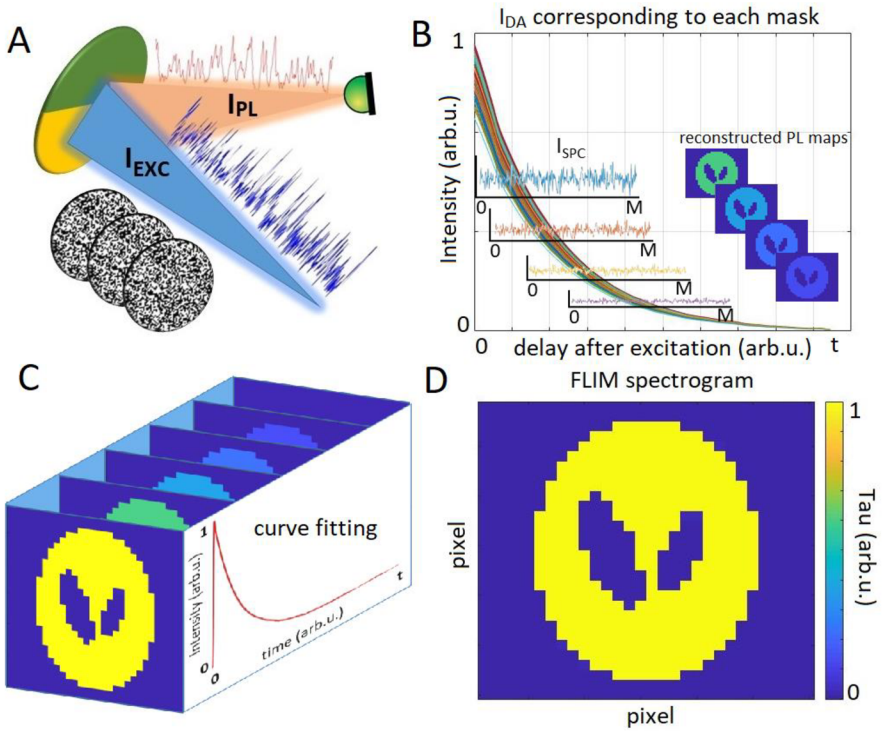

Figure 16: (A)Scheme of the 2D-RATS approach where the sample is illuminated by a set of random patterns (masks) fluctuating in intensity according to $I_{EXC}(t)$. The overall $I_{PL}(t)$ corresponding to the given mask is detected by a single-pixel detector. (B)Example of a set of calculated I_{DA}s for the corresponding set of masks – see Eq.(8) – and fluctuations I_{SPC} in intensity for each delay after excitation. (C)Knowledge of the I_{SPC} signal and the set of used masks will allow determining the PL map m(t) for a given time point t of the I_{DA} curve using reconstruction algorithms. (D)An example of a final FLIM spectrogram as a map of PL lifetimes. Adapted from Junek et al. [49], Fig. 1.

By reconstructing the temporal frame (a 2D image) for each time point of the I_{DA} curve, we obtain 3D datacube that contains the PL decay curve for each *i*-th pixel of the $I_D(i,t)$ sample. In each *i*-th pixel, it is, therefore, necessary to perform the fitting of the given curve to determine the lifetime τ. The whole concept is illustrated and summarized in Fig. 16.

5.2 FLIM$_A$ reconstruction approach

This approach is also based on the use of a single-pixel camera configuration. The assumption is made that if we illuminate the entire measured area with a homogeneous illumination, which still fluctuates in time according to I_{EXC}, we can reconstruct the total PL decay curve I_{DA0} according to Eq.(8). The I_{DA0} curve then contains all lifetimes τ present in the measured sample, which can be revealed via fitting. The extracted

lifetimes then create a cornerstone for the subsequent FLIM data processing. In practice, it is often appropriate to consider a bi-exponential curve, at most a tri-exponential one, mainly because of the similarity of individual multi-exponentials and the possibility of a wrong fit [1].

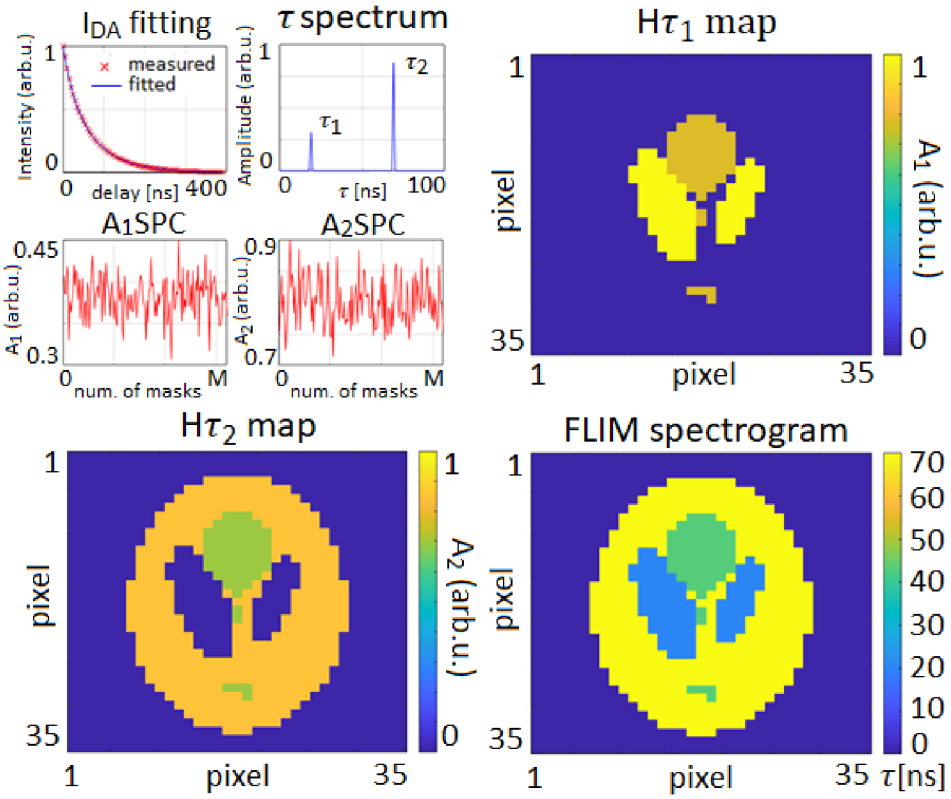

Figure 17: (A) Example of fitting I_{DA} curve amplitudes A_1 and A_2, where the distribution of τ_1 and τ_2 is already known from I_{DA0} fitting. The amplitude fitting provides vectors A_1SPC and A_2SPC. (B) Reconstructed amplitude map Hτ_1. (C) Reconstructed amplitude map Hτ_2. (D) Calculated FLIM spectrogram based on knowledge of Hτ_1 and Hτ_2. Adapted from Junek et al. [49]. Fig. 4.

In the following elucidation of the data processing, we will consider a bi-exponential curve (see Eq.(4)), where we would obtain parameters τ_1 and τ_2 via fitting I_{DA0}. Subsequently, the scene is illuminated by a set of M masks with N pixels. The two numbers are connected via the compression ratio $k = M/N$. For each mask, the corresponding I_{DA} is determined according to Eq.(8). Each I_{DA} is then fitted with the fixed parameters τ_1 and τ_2, which were obtained by the initial fitting of the total PL decay I_{DA0}. Therefore, the only fitting parameters are A_1 and A_2 (see Eq.(4)). Since the amplitudes connected to the PL lifetimes are extracted for each mask, two vectors, A_1SPC and A_2SPC, of size M are obtained. Vectors A_1SPC and A_2SPC contain information about PL amplitude connected to the PL lifetimes τ_1 and τ_2.

From the knowledge of A_1SPC and A_2SPC and the dataset of random masks B, it is possible to calculate the amplitude maps $H\tau$ corresponding to the individual lifetimes τ_1 and τ_2, where TV denotes the total variation, according to Eq.(10).

$$min\left\{\left\|BH_{\tau n}-A_nSPC\right\|_2^2+TV(H_{\tau n})\right\}. \tag{10}$$

The lifetime maps can be then evaluated individually, and an effective PL lifetime (FLIM spectrogram) is possible to calculate from them. There is no general approach to a correct calculation of a mean PL lifetime, and the particular solution depends on the studied system. In this thesis, we calculated the desired FLIM spectrogram by the weighted averaging of the present lifetimes. The weights in a given pixel are represented via $H\tau$ maps. In the general case of the n-exponential case, we then define the FLIM spectrogram $\tau(x,y)$ as:

$$\tau\left(x,y\right)=\frac{\sum_{i=1}^{n}H_{\tau i}\tau_i}{\sum_{i=1}^{n}H_{\tau i}}. \tag{11}$$

The principle of FLIM spectrogram determination using direct reconstruction of amplitude maps is summarized in Fig. 17. We would like to outline here a significant reduction of post-processing time because it is necessary to make just as many reconstructions as the n-exponential case is expected/found. The amount of the saved post-processing time compared to the standard algorithm ($FLIM_B$) depends on the number of expected/found lifetimes, scene resolution, compression ratio and temporal resolution of I_{DA}s. Nevertheless, for the typical experiments, the post-processing time decreased 10 times. More details can be found in Junek et al. [49].

5.3 Optical setup for 2D-RATS measurement

The optical arrangement of the 2D-RATS depends on the choice of the random excitation signal generator, which was presented in Section 4.3. By choosing an analog signal generator based on a rotary diffuser (see Section 4.4.1), we can expect significant losses in the intensity of the excitation energy compared to a digitally random modulated laser (see Section 4.4.2).

Another decisive parameter is the approach to random mask generation. The first implementation of 2D-RATS used a laterally sliding diffuser, by which it was possible to generate masks in grayscale and the attained spatial resolution was based on the properties of speckle patterns generated by the diffuser. Since the speckles do not inherently feature sectioning to pixels, the speckle masks needed to be scaled with a suitable parameter to a certain 2D array, which also determined the resolution. Various scaling parameters were tested as a part of simulations, but within a reasonable range of scaling where a pixel size was set close to the mean speckle size, no significant effect on the image quality was detected. A certain

trend was observed by using a more coarse of fine pixelation with respect to the mean speckle size. Using a lower resolution, i.e. choosing a pixel size larger than the mean speckle size, causes a loss of image quality. In the other direction, a higher resolution, i.e. choosing a pixel size smaller than the mean speckle size, cannot provide adequate fineness of information – see Junek et al. [47] for more details.

The second way of generating a random mask is using a digital micro-mirror device (DMD) to generate binary masks with the option of choosing a resolution limited by the chip parameters and imaging optics within the experiment.

Two optical arrangements based on the 2D-RATS method will be presented in the following subsections. The first one shows the possibility of FLIM measurement using two diffusers. The second optical setup shows the implementation of the RATS principle into microscopy using DMD and a digitally modulated signal.

5.3.1 FLIM via RATS method using double-diffused light

The optical arrangement using a double-diffuser spatiotemporal pattern generation is shown in Fig. 18. A continuous laser with a wavelength of 405 nm was used as a light source. The combination of a focusing lens A (f = 25.4 mm), a rotating diffuser (average grain size 4 μm) with a collimating lens B (f = 75 mm), and an aperture (diameter 1.5 mm) generated an intensity varying randomly in time $I_{EXC}(t)$. Random mask generation (for single-pixel camera purposes) was achieved using an additional focus lens C (f = 25.4 mm). The beam was focused onto a moving diffuser (average grain size 8 μm), and the scattered light was again collimated by lens D (f = 50 mm). The resulting mask pattern varied in intensity over time according to $I_{EXC}(t)$.

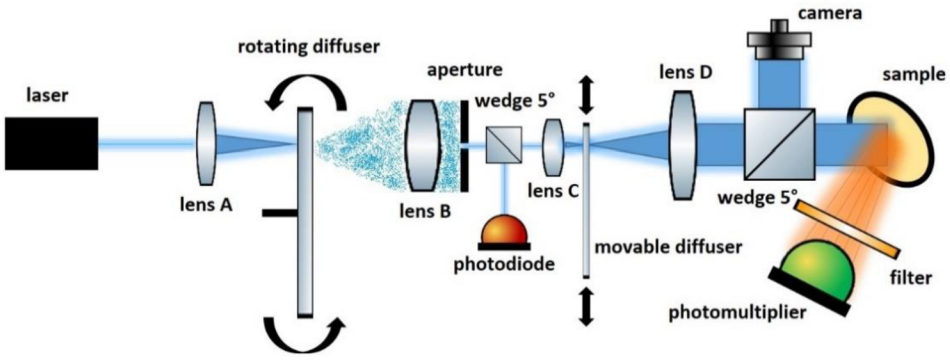

Figure 18: Schematic of the optical arrangement for 2D-RATS in a single-pixel camera configuration based on two optical diffusers. Adapted from Junek et al. [47], Fig. 4.

The beam was split twice by two 5° wedges N-BK7, which reflect about 6% of the incident intensity. The first reflection was used to detect $I_{EXC}(t)$ using a Si-amplified photodetector. The reflected beam from the second N-BK7 5° wedge was used to obtain the mask pattern using a CMOS chip. The

transmitted pattern was used to illuminate the measured sample. The PL emitted from the excited sample, i.e. the $I_{PL}(t)$ signal, was detected by a photomultiplier. The scattered excitation light was blocked by a cut-off filter with a pass edge of 500 nm so that the excitation wavelength (405 nm) did not reach the photomultiplier. The detected PL signal was amplified by an amplifier and read by a USB oscilloscope.

The intensity of the laser beam exiting the laser was 138.5 mW, while the full average intensity that illuminated the measured sample oscillated around 5.5 μW. The total efficiency of the system was about 0.003%, which, however, can be optimized through the parameters of the optical elements and by using an engineered diffuser scattering light more efficiently in a selected direction. The size of the measured area was approx. 18 mm^2 and was determined by the size of the generated spotted masks. The field of view can be changed by adjusting the collimation lens D.

5.3.2 FLIM via RATS method in a microscopy setup

The microscope setup was based on the principle of random digital signal modulation and the generation of illuminating masks using DMD. A time-modulated Cobolt S06-01 MLD laser (405 nm) was used as a light source. The modulation signal was produced by the development kit Digilent Cmod A7 and was generated in the FPGA Xilinx Artix-7 (VIVADO software package).

The optical beam was further enlarged by 20× using a beam expander and brought to the DMD chip (Texas Instruments DLPLCR65EVM) using mirrors M_1 and M_2 so that the beam propagated perpendicular to the surface of the DMD chip. However, the size of the chip's individual pixels (7.56 μm) generates the diffraction pattern corresponding to the rectangular grid. Therefore, the DMD was followed by a lowpass filter composed of lenses L_1 (f = 75 mm), L_2 (f = 50 mm), and iris aperture to use the zero diffraction order.

Another important component was the beam splitter BS (N-BK7, 50:50 ratio), which ensureed beam deflection for I_{EXC} detection on the photodiode and beam deflection in the opposite direction to the camera, thanks to which it was possible to determine the ideal focus.

The sample was then illuminated through a bandpass filter F_1 (405 nm), a dichroic filter DM (cut-off 425 nm), and through an achromatic objective (4X Olympus (0.10 NA, 18.5 mm WD)). The intensity of illuminating mask followed the temporal fluctuations of $I_{EXC}(t)$. The I_{PL} signal was collected by the objective lens and was reflected by the DM to the photomultiplier. The I_{PL} was spectrally filtered before the photomultiplier with a cut-off filter (500 nm) for complete shielding of parasitic scattering of I_{EXC}. The scheme of the optical setup is summarized in Fig. 19. More detailed information can be found in the attached article – Junek et al. [49].

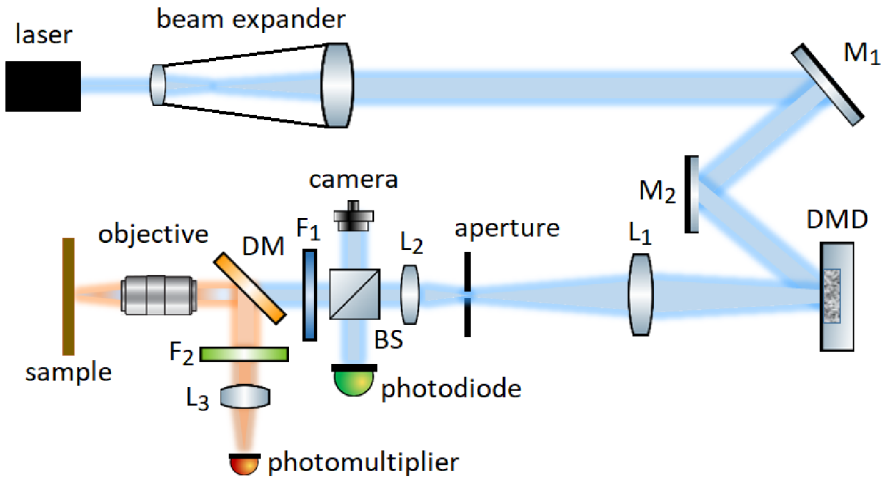

Figure 19: Schematic of a 2D-RATS optical setup implemented in a microscope setup using DMD narrowing and digital time modulation. Adapted from Junek et al. [49], Fig. 7.

5.4 Reconstruction parameters

In both reconstruction approaches, $FLIM_A$ and $FLIM_B$ (see Sections 5.1 and 5.2), we used the TVAL3 algorithm to calculate the undetermined systems [52,53]. The TVAL3 algorithm uses the total variation (*TV*) of reconstructed images as a regularization parameter. The minimization is governed by Eq.(9) or Eq.(10) [54]. The reconstruction parameters were set according to a number of test experiments and simulations.

In the case of grayscale speckle masks and the reconstruction principle $FLIM_B$, the reconstruction parameters were: *mu* (2^9), *beta* (2^6) (see Junek et al. [47]). The same parameters were also used in the case of binary masks and the reconstruction principle $FLIM_A$ see Junek et al. [49]. However, it has been shown that if we use binary scale masks and the reconstruction principle $FLIM_B$, it is more advantageous to use the reconstruction parameters: *mu* (2^{11}), *beta* (2^7) (see Junek et al. [49,50]).

5.5 Proof of principle experiments

The following section will present measurements of two different samples as proof of the principle experiments of both reconstruction routines, $FLIM_B$ and $FLIM_A$, described in Sections 5.1 and 5.2. More measurements and more detailed data can be found in the attached articles [47,49].

5.5.1 2D-RATS using the $FLIM_B$ reconstruction approach

The measured testing sample was an absorbing cut-off filter OG565, which was divided by an opaque tape into two regions with the same lifetimes. Such a situation corresponds, for example, to mapping one PL marker in the sample. The optical setup was based on two diffusers -- see Section 5.3.1.

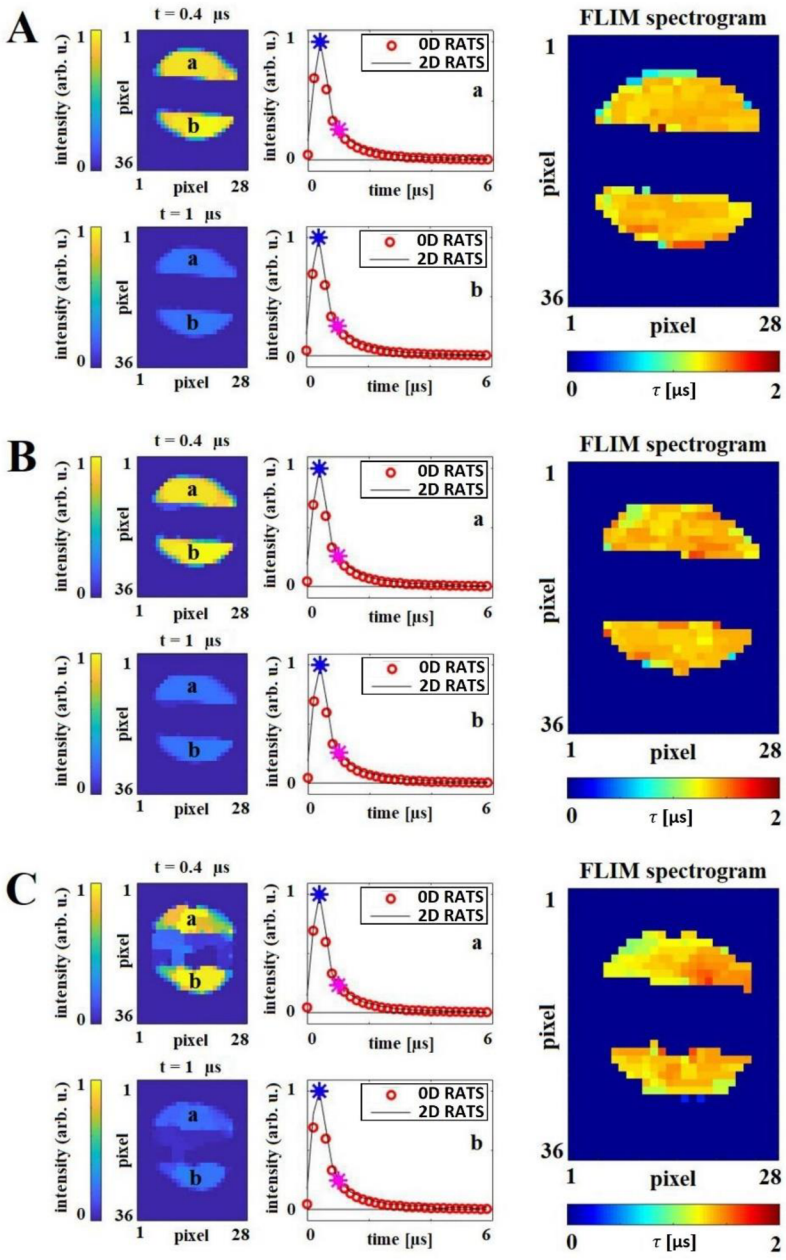

Figure 20: Measurement of divided filter OG565 – two areas with the same PL decay. (A) compression ratio 0.4, (B) compression ratio 0.2, (C) compression ratio 0.05. Left panels: PL map reconstruction for two different timepoints. Middle part: "a" and "b" plots of I_D reconstructed by 2D-RATS in a randomly selected pixel ("a" pix [14,10], "b" pix [16,25]) and I_D calculated by 0D-RATS; blue and purple stars indicate time points corresponding to the depicted PL maps in the left part of the image. Right part: FLIM spectrogram with pixels where the PL amplitude exceeded 10% of the maximum PL intensity of the sample. Adapted from Junek et al. [47], Fig. 8.

The illuminated area was ~18 mm^2, and the number of masks $M = 400$. The mask resolution was set according to the mean speckle size, resulting in an image resolution of 28 × 36 pixels ($N = 1008$).

Image reconstruction was tested for three different compression ratios k, where the number of pixels N always remained the same, and the number of used masks M was reduced accordingly. Specifically, the compression ratio $k = 0.4$ (see Fig. 20(A)), $k = 0.2$ (see Fig. 20(B)), and $k = 0.05$ (see Fig. 20(C)) were used. The corresponding measuring times were 47 minutes, 24 minutes, and 6 minutes, respectively.

The left part of each panel (A), (B), (C) in Fig. 20 shows the reconstruction of the PL map for two different times of PL decay. The middle part contains plots "a" and "b", which show the PL decay I_D of a randomly selected pixel that corresponds to the reconstructed region "a" or "b". Two timepoints of I_D (blue and purple stars) correspond to the reconstructed PL maps on the left part of the figure. The reconstructed I_D data via 2D-RATS (black lines) were compared with the 0D-RATS measurement (red circles). Although the reconstructed PL maps are noisier when using a low compression ratio of $k = 0.05$, the PL decay curves I_D of the 0D and 2D-RATS methods are still in perfect agreement.

The resulting FLIM spectrogram is shown on the right side of the figure for each panel. The individual values of the lifetimes τ were determined by PL decay fit. The reconstructed I_D curves at each pixel were fitted with a bi-exponential function, and the PL lifetime τ was then determined as the time when the intensity of the fitted bi-exponential decay decreased to 10% of the maximum of the curve. The width of the impulse response function of the given measurement was 0.47 µs.

The average lifetimes for the sample measured with compression ratios of 0.4, 0.2, and 0.05 were 1.31 µs, 1.29 µs, and 1.29 µs, respectively. The mean lifetimes shown vary with standard deviations of 0.09 µs, 0.10 µs, and 0.13 µs. Statistical data do not include points that did not show a luminescence intensity lower than 10% of the sample maximum, as well as data from the edge of the sample, which are distorted by signal dispersion and high noise levels.

5.5.2 2D-RATS using the $FLIM_A$ reconstruction approach

Here we present the test of the 2D-RATS experimental setup using a DMD-modulated spatial pattern and laser-modulated temporal excitation waveform. We picked the testing sample LuAG:Ce crystal as the testing sample. The material is mainly used for its scintillation properties but also has a strong PL [55]. We used a thin monocrystal polished on both sides, which suffered from visible scratches and cracks on the surface. One of these cracks was analyzed using the setup presented in Section 5.3.2. Since it was a monocrystal, a significant increase in PL intensity at the crack location was expected due to the efficient outcoupling of the PL light at this spot. In other words, we expected a higher amplitude value in $H\tau$.

The mapped area (shown in Fig. 21) was 450x450 µm with a pixel size of 12.6 µm (35 x 35 pixels). The compression ratio was set to $k = 0.4$ (490 measurements). The scanning time for one mask took 10 ms.

Nevertheless, the resulting measurement time reached tens of minutes, primarily due to data storage and processing, which can be undoubtedly improved.

The sampling frequency was set to 200 MS/s, and the modulation frequency of the fastest bit of the random signal reached 98 MHz, which resulted in IRF = 9.9 ns.

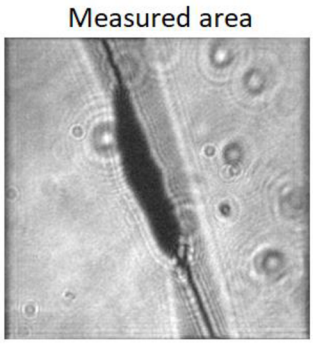

Figure 21: Mapped surface area of LuAG:Ce captured by a monochromatic camera (see Fig.19). Adapted from Junek et al. [49], Fig.11.

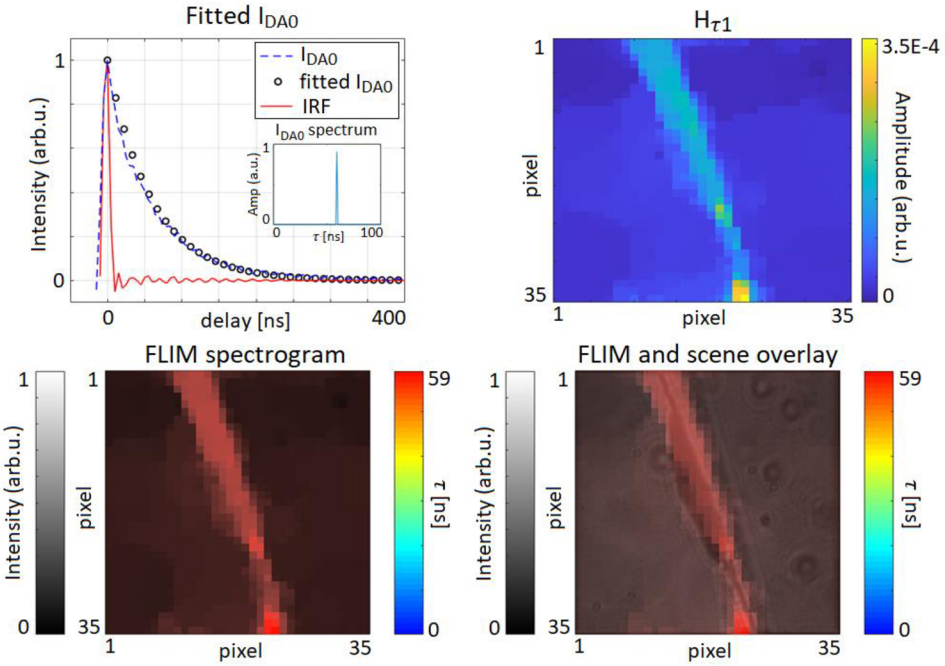

Figure 22: (Upper part) Fitted I_{DA0} with mono-exponential curve and reconstructed area $H\tau_1$ for corresponding τ_1. (Lower part) FLIM spectrogram determination and its overlay with the measured scene. Adapted from Junek et al. [49], Fig. 13.

During I_{DA0} analysis, we found that it is sufficient to represent the PL dynamics via mono-exponential decay. Therefore, the obtained $H\tau$ directly represents the FLIM spectrogram. The decay of the given

region was determined as 59 ns, which corresponds well with the PL lifetime of LuAG:Ce [56]. In this case, we achieved a clear image of the crack with a high PL intensity together with low-intensity PL regions surrounding the cracks, where the PL is outcoupled from the monocrystal inefficiently.

6 Noise effect analysis

Since the RATS method is a novel approach to FLIM measurement, it is appropriate to analyze the method from the point of view of noise stability. In order to maintain constant conditions, this analysis was performed using simulations that faithfully copied real experimental data. The primary I_{EXC} signal was simulated using temporal speckle patterns [45], the random analog signal generator presented in [46]. White noise was added to the dataset, initially only to the I_{EXC} signal, while the I_{PL} signal remained absolutely noiseless and vice versa. The amount of noise added to the assembly was SNR 23 dB (0.5%), 20 dB (1%), 18.2 dB (1.5%), 15.2 dB (3%), which corresponds to real experimental conditions. The duration of the simulated I_{EXC} signal was 0.1 s with an impulse response function FWHM of 2.07 µs. I_D was considered with τ = 20 µs. The I_{EXC} excitation signal was simulated as non-periodic. Unless otherwise stated further, the regularization parameter ε (Eq.(3) and Eq.(8)) is kept as $\varepsilon = 0.1$.

Within the following sections, only a brief overview of the most important results is presented. A general description of all investigated parameters can be found in Junek et al. [50]. Due to the timeline of the research of the RATS method, the noise analysis is aimed mainly at the original approach ($FLIM_B$) of reconstruction (see Section 5.1), where the lifetimes are extracted by fitting the PL decay curve in each pixel. Therefore, the quality of reconstructed PL maps for every delay after excitation is crucial.

Nevertheless, most of the knowledge, especially the optimization of the effect of noise on the reconstruction of the PL decay curve for a single random mask I_{DA}, is also freely transferable to the alternative $FLIM_A$ reconstruction approach. We remind the reader that the $FLIM_A$ approach is based on the direct reconstruction of amplitude maps corresponding to lifetimes τ (see Section 5.2).

A comparison of the noise effect on both reconstruction approaches, $FLIM_A$ and $FLIM_B$, is provided in Section 6.4.

6.1 0D-RATS

To demonstrate the fundamental behaviour of the RATS method, we will start with a non-imaging RATS method, i.e., 0D-RATS. Excitation I_{EXC} and PL I_{PL} signals are used for the PL decay I_D reconstruction. Therefore, the effect of the present noise is simulated in both excitation and PL datasets. Firstly, the noise was added to the I_{EXC} signal while the I_{PL} remained absolutely noiseless (Fig. 23(A)) and vice versa (Fig.

23(B)). In both cases in Fig. 23, the signal-to-noise ratio (SNR) was 15.2 dB, corresponding to 3% noise in the system.

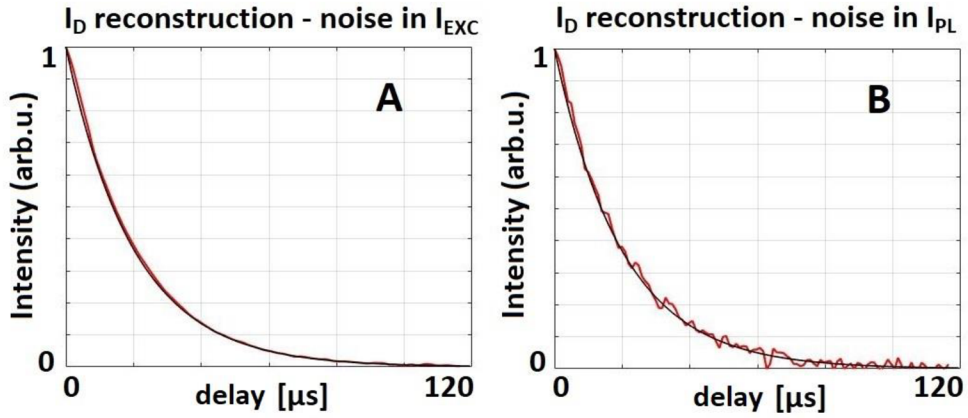

Figure 23: (A) I_D reconstruction with a noise level of 3% in the I_{EXC} signal, corresponding to an SNR of 15.2 dB. I_{PL} was considered noiseless. (B) I_D reconstruction with a noise of 3% in the I_{PL}, corresponding to an SNR of 15.2 dB. I_{EXC} was considered noiseless. Adapted from Junek et al. [50], Fig. 2.

It can be observed in Fig. 23 that the added noise had an effect on the I_D reconstruction (red line) in both cases, but the shape of the I_D PL decay curve was not distorted, i.e. the overall shape of the PL decay was in perfect agreement with the expected output (black line). However, it can also be seen that the noise in the I_{PL} dataset had a significantly higher effect on the resulting noise in the obtained I_D (Fig. 23(B)), despite using the same relative noise level in both panels.

We can quantify the noise of the I_D curve using the root mean square error, which reaches $RMSE_{PL} = 12.9\times10^{-3}$ for the noise in the PL signal and $RMSE_{EXC} = 2.8\times10^{-3}$ for the noise in the excitation signal. This apparent difference originates from the deconvolution step used to calculate the PL decay curve – see Eq.(3). This result suggests that the Tikhonov regularization in the denominator of Eq.(3) has a more pronounced effect on I_{EXC} than I_{PL}, which becomes the dominant noise source in the obtained I_D.

6.2 Noise effect on PL map reconstruction using the FLIM$_B$ approach

The next step was to simulate the effect of the presence of noise in the I_{PL} and I_{EXC} signal on the data reconstruction in the 2D-RATS experiment. Here the situation is more complicated because the noise present in the I_{PL} and I_{EXC} datasets is first transposed into the noise of the $I_{DA}(t)$ curve (Eq.(8)). The noise present in these curves is then propagated into the I_{SPC} signals, which are then used to obtain a set of $m(t)$ PL images (Eq.(9)).

All simulated reconstructions were performed assuming binary masks. The TVAL3 algorithm was used as the reconstruction algorithm, where the main parameters of the TVAL3 algorithm were set as *mu*

(2^{11}), *beta* (2^7). A predefined Phantom image was used as the measured sample in Matlab, where a mono-exponential I_D with PL lifetime τ = 20 µs was set over its entire "body".

Below are the obtained PL images $m(t)$ at the maximum I_{DA} intensity, i.e. t = 0 µs, where the contrast of I_{SPC} signal fluctuations is the highest. The case was studied for three different compression ratios k = 0.4, 0.6, 0.8 and four signal-to-noise ratios *SNR* = 15.2, 18.2, 20, 23 dB, corresponding to 3%, 1.5%, 1%, 0.5% noise level in the signal.

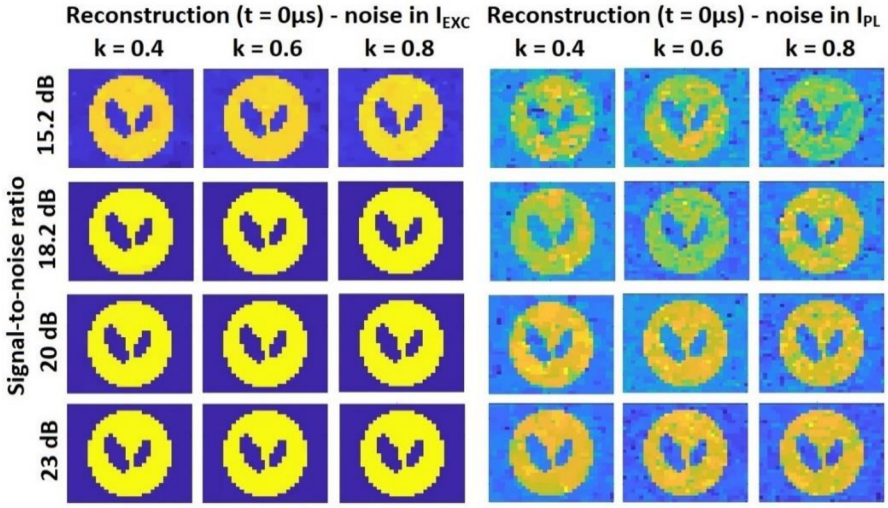

Figure 24: Left part: reconstruction of PL map m(t) at the I_D timepoint of maximal intensity (t = 0 µs) in the case of noise in I_{EXC}. Right part: reconstruction of the PL map m(t) at the timepoint (t = 0 µs) in the case of the noise in the I_{PL}. Rows: signal-to-noise ratios SNR = 15.2, 18.2, 20, 23 dB (rows). Columns: compression ratios k = 0.4, 0.6, 0.8. Adapted from Junek et al. [50], Fig. 3.

The results of the simulations are summarized in Fig. 24, where the reconstruction with noise in the I_{EXC} signal is on the left side, while the reconstruction with noise in the I_{PL} signal is on the right side. The corresponding parameters are listed in Table 1.

Similar to 0D-RATS, the noise present in the I_{PL} has a significantly higher effect on image reconstruction than the noise in the I_{EXC} signal. By comparing the different noise levels (rows of Fig. 24), it is clear that the SNR in the I_{PL} signal is a key factor in data acquisition. On the other hand, the effect of the compression ratio (columns of Fig. 24) does not play an essential role for values of k > 0.4. This means that it is not practical to compensate for the noise in the measured signal by simply increasing the number of measured excitation masks.

To quantify the overall impact of the noise, three different criteria are introduced. First, we can assess the quality of the image reconstruction, where we compare the reconstructed PL map m (at the I_{DA}'s timepoint t = 0 µs) with the reference U using the Frobenian norm:

$$r = \frac{\|m - U\|_F}{\|U\|_F}. \tag{12}$$

Second, we focused on the secondarily affected SNR of the I_{SPC} signal, which is used to acquire the image $m(t)$ at the timepoint t = 0 µs. It can be seen that the I_{SPC} signal indicates the fluctuation of the I_{DA} curves. This fluctuation (I_{SPC}) is affected by the noise of both I_{EXC} and I_{PL}. By extracting the resulting noise in I_{SPC}, we provide a comparison for other SPC experiments. Thus, we define *SPC-SNR*$_{EXC}$, which stands for the noise level in the I_{SPC} when the noise was in I_{EXC}. Similarly, we also define *SPC-SNR*$_{PL}$ indicates the case when the noise was added to the I_{PL}. Analogously, the indices "PL" and "EXC" have the same meaning for r_{EXC} and r_{PL}.

Table 1: The quality of the reconstructed image (r, lower number = higher reconstruction quality) and the noise level in the I_{SPC} signal (*SPC-SNR*, higher number = lower amount of noise). Corresponding to Fig. 24.

	noise source	k	amount of noise			
			SNR 15.2dB	SNR 18.2dB	SNR 20dB	SNR 23dB
r	EXC	0.4	0.177	0.158	0.150	0.142
		0.6	0.175	0.155	0.149	0.142
		0.8	0.175	0.155	0.149	0.142
	PL	0.4	0.328	0.265	0.242	0.191
		0.6	0.312	0.264	0.215	0.192
		0.8	0.326	0.261	0.224	0.181
SPC-SNR	EXC	0.4	38.01	43.80	48.14	54.97
		0.6	38.06	43.84	48.05	55.04
		0.8	37.98	43.90	48.25	55.16
	PL	0.4	34.67	37.52	39.53	43.24
		0.6	34.86	37.45	40.01	43.10
		0.8	34.84	37.83	39.48	42.72

Finally, we can focus on the quality of PL dynamics reconstruction at each pixel i, where the reconstructed decay $I_{DREC}(i)$ is normalized and compared to the reference decay $I_D(i)$. The comparison was made from t_0 = 0 µs to t_τ = 120 µs, which is a sufficient time range for a decay comparison with a lifetime of τ = 20 µs. We refer to this error as the decay deviation σ, which can be determined according to Eq.(13).

$$\sigma = \frac{1}{N}\sum_{i=1}^{N}\sum_{t=t_0}^{t_\tau}\sqrt{\left(I_{DREC}(i,t) - I_D(i,t)\right)^2}. \tag{13}$$

This parameter is of the greatest importance in characterizing the quality of the FLIM reconstruction and will be investigated in detail in the following section, where some optimization steps will be also proposed.

6.3 Optimization of noise effect on PL map reconstruction

The noise in the optical system is determined by the properties of the optical assembly, which characterizes the number of detectable photons on the detector. For an optimized optical arrangement, these properties cannot be easily improved.

On the other hand, it is possible to increase the quality of the acquired I_D or I_{DA} by increasing the acquisition time. This option is described in the following section. Since the RATS method is based on signal deconvolution, we used a non-periodic excitation signal I_{EXC} (see Section 4.5.2). In addition, the influence of the choice of the regularization parameter ε from Eq.(3) and Eq.(8), respectively, was investigated.

Due to the random nature of the signals, no mathematical filtering of the signal was intentionally applied, as important frequencies would easily be eliminated. Mathematical signal filtering could certainly be optimized for one random pattern of signal, but at the expense of the general applicability of the results.

6.3.1 Data acquisition time prolonging

Prolonging the acquisition time favours the frequencies representing the real signal in the Fourier spectrum and suppresses the contribution of artificially added white noise. Simulations of the 2D-RATS measurement were done for 5 different acquisition times t_{acq} = 0.1 s, t_{acq} = 0.2 s, t_{acq} = 0.4 s, t_{acq} = 1 s and t_{acq} = 2 s (see Fig. 25). Other conditions, such as reconstruction parameters, regularization parameter ε, and signal properties, remained the same as in Section 6.2.

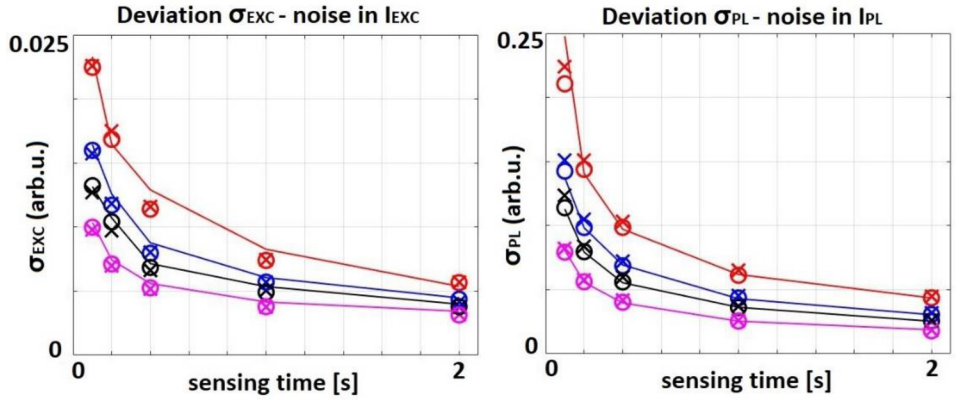

Figure 25: Dependence of the acquisition time on the deviation σ_{EXC} – noise considered in I_{EXC} (left part) and σ_{PL} – noise considered in I_{PL} (right part). SNR: 15.2 dB (red), 18.2 dB (blue), 20 dB (black), 23 dB (magenta) for three different compression ratios k = 0.4 (solid line), k = 0.6 (circle), k = 0.8 (cross). Adapted from Junek et al. [50], Fig. 9.

Unlike Section 6.2, this section focuses on the deviation of the entire reconstructed PL decay in each sample pixel, where the subscripts "PL" and "EXC" denote the noise source (σ_{EXC}, σ_{PL}). The

dependences of individual noise characteristics on acquisition time are shown in Fig. 25. In this figure, the colour of the line/symbol indicates the given SNR (red: 15.2 dB, blue: 18.2 dB, black: 20 dB, and magenta: 23 dB); line/symbol type represents compression ratio k (cross: 0.8, circle: 0.6, solid line: 0.4).

All the results in Fig. 25 confirm that the effect of the noise level (different colours) is much more pronounced than the compression ratio (different line/symbol type), i.e. increasing the number of excitation masks compared to the number of pixels has a negligible effect on the image quality.

The decay curve reconstruction is improved for both noise in I_{EXC} and I_{PL}, and the deviation σ decreases with increasing acquisition time (see Fig. 25). Although both errors are of a different order, by increasing the acquisition time from 0.1 s to 2 s, both errors, $\sigma_{EXC,}$ and σ_{PL} decreased by the same ratio.

6.3.2 Choice of the regularization parameter ε

Another way to eliminate the effect of noise is the choice of the regularization parameter ε in Eq.(3) or Eq.(8). The regularization parameter makes it possible to solve ill-conditioned problems where "division by zero" could occur, i.e. for frequencies with low amplitude in the I_{EXC} signal [44]. The regularization parameter adds a specific amount of the averaged spectrum power to the denominator (see Eq.(3) and Eq.(8)). Thus eliminating the influence of less frequent frequencies in the signal (white noise). As a result, the calculated I_D or I_{DA} course is smoothed.

All simulations were performed with an acquisition time of t_{acq} = 0.1 s and ε ranging from 0.05 to 1. Reconstruction parameters and signal properties were kept as in Section 6.2. Fig. 26 has an analogous colour and symbol marking as in the previous part of Fig. 25 - SNR (colour) and compression ratio (line/symbol type).

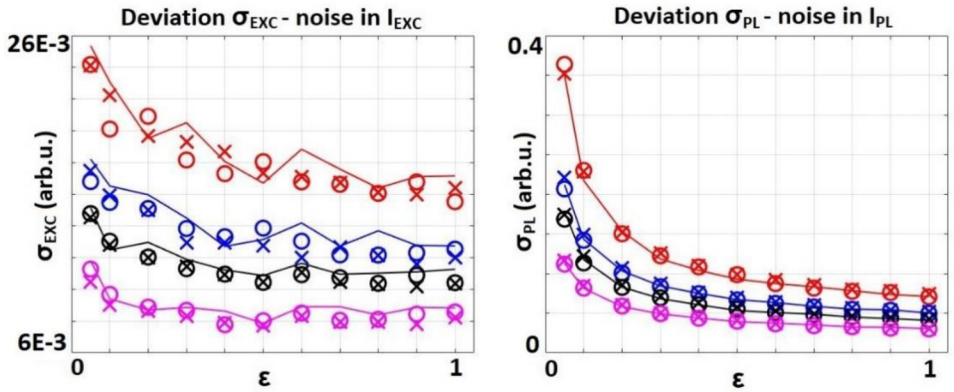

Figure 26: Dependence of ε on deviation σ_{EXC} – noise considered in I_{EXC} (left part) and σ_{PL} – noise considered in I_{PL} (right part). SNR: 15.2 dB (red), 18.2 dB (blue), 20 dB (black), 23 dB (magenta) for three different compression ratios k = 0.4 (solid line), k = 0.6 (circle), k = 0.8 (cross). Adapted from Junek et al. [50], Fig. 12.

Choosing a higher ε smooths the I_D/I_{DA} but also causes a certain distortion of I_D/I_{DA}, affecting $m(t)$ reconstruction. These two effects always go against each other. The issue is discussed in an article by Junek et al. [50]. It follows from the findings that for less noisy systems, it is advisable to keep the regularization parameter at a value of 0.1 to 0.2, but for systems with higher noise, it is advisable to increase ε proportionally to the noise level. As can be seen from Fig. 26, the dependence of both σ_{EXC} and σ_{PL} on ε is affected by the amount of noise in the system. The most significant improvement is made in the noisy PL signal (15.2 dB, 3%), where increasing ε from 0.05 to 1 reduced σ_{PL} by 79%. Analogously to the previous results, increasing the regularization parameter has a smaller effect on the noise introduced by the I_{EXC} signal -- see the σ_{EXC} curve.

6.4 Noise stability of reconstruction approaches $FLIM_A$ and $FLIM_B$

In the previous section, we focused on the noise effect on the retrieved PL decay curves I_{DA} and PL maps reconstruction, which influence the resulted decay in each i-th pixel $I_{DREC}(i,t)$ and affect the final FLIM spectrogram.

Now, we can focus directly on the effect of noise on FLIM spectrogram quality, i.e. to compare the precision of the retrieved PL lifetimes. By doing this, we can compare both approaches, $FLIM_A$ and $FLIM_B$, which feature significantly different data processing, but both lead to a PL lifetime map.

Based on the results presented in the previous chapters and the results presented by Junek et al. [50], we focused only on the compression ratio $k = 0.4$; the noise is present only in the measured PL signal I_{PL}, while the excitation dataset I_{EXC} was assumed to be noiseless. The level of noise was set to relative values of 0%, 0.5%, 1%, and 1.5%. The resulting FLIM spectrogram labelled F was evaluated by the percentage deviation R when compared to the simulated reference U.

$$R = \frac{\sum \sqrt{(F-U)^2}}{\sum \sqrt{U^2}} \times 100. \tag{14}$$

We carried out simulations on a bi-exponential PL decay based on the Phantom image. The simulated scene considered mono-exponential and bi-exponential regions with parameters $\tau_1 = 20$ ns and $\tau_2 = 70$ ns and corresponding amplitudes $A_1 = 1$ and $A_2 = 1$.

The simulation results are summarized in Fig. 27, where the individual row represents the different noise levels in the I_{PL} signal, while the columns indicate (from the left) the amplitude maps of two PL components: $H\tau_1$, $H\tau_2$; resulting PL lifetime map composed from the amplitude maps: $FLIM_A$; finally, the map was compared to the PL lifetime map attained by fitting each individual pixel independently: $FLIM_B$. The dependence of the deviation R on the noise level is then provided in Fig. 28. Reconstructed pixels that were below 10% of the PL amplitude were removed from the statistics for both $FLIM_A$ and $FLIM_B$ in Fig.

27 and also in Fig. 28. The fitting curves for both $FLIM_A$ (I_{DA}'s) and $FLIM_B$ (3D-datacube) cases were always in the range of 0 ns to 400 ns, which is sufficient for the entered parameters τ_1 and τ_2.

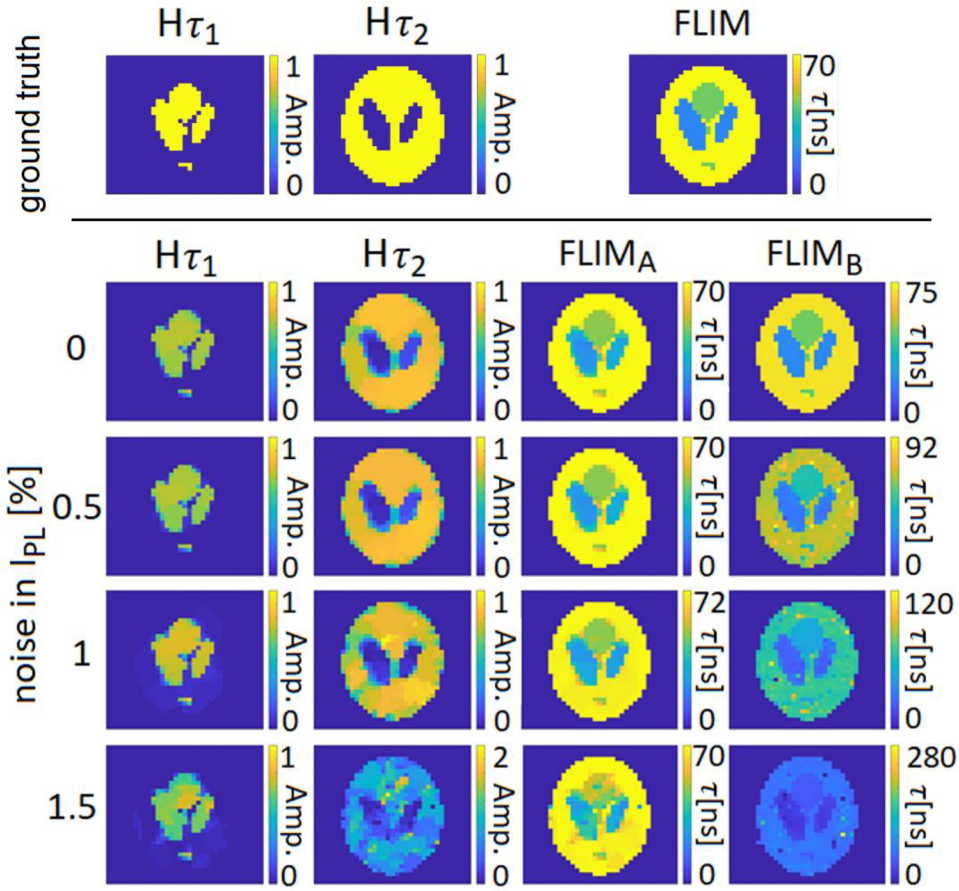

Figure 27: Above the line is the ground truth, which can be compared to the simulated results below the line. The results of simulations of noise effect on both post-processing approaches. The $FLIM_A$ approach is represented in the third column - supplemented by reconstructions of partial amplitude maps $H\tau_1$ (the first column) and $H\tau_2$ (the second column). The results of the $FLIM_B$ approach are presented in the fourth column. Each row corresponds to the chosen noise level in the system (0-1.5%). Adaptet form Junek et. al [49]. Adapted from Junek et al. [49], Fig. 5.

To better understand the results, it should be noted that $FLIM_B$ depends mainly on noise in I_{SPC}, i.e. the intensity dataset, which is used to retrieve the scene via the TVAL3 algorithm. The noise in I_{SPC} affects the quality of PL map reconstruction in the 3D-datacube. As a result, fitting in individual $FLIM_B$ pixels can be distorted by these inaccuracies and cause local errors in the spectrogram.

On the other hand, the approach to obtaining $FLIM_A$ can affect the overall result already in the zeroth step when we extract the PL lifetime component via I_{DA0} fitting of the overall PL dynamics. Although

the inaccuracy of the I_{DA0} fit will not directly affect the quality of the reconstruction of the $H\tau$ amplitude map image, it will systematically affect the final error of the FLIM spectrogram, where the obtained life-times from the zeroth step are directly considered.

In view of Fig. 27 and Fig. 28, the $FLIM_A$ approach is more stable in terms of noise, while the $FLIM_B$ approach may experience local errors. Only in the 0% noise case was the $FLIM_B$ approach more accurate than $FLIM_A$ because the overall $FLIM_A$ spectrogram distortion was reflected by a slight deviation in the I_{DA0} fit (zeroth step).

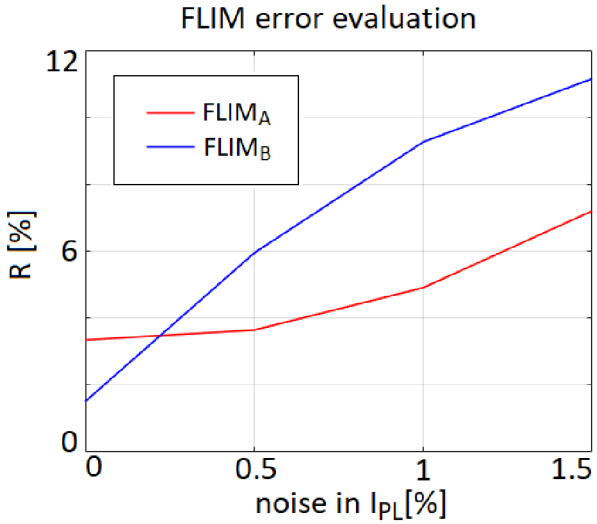

Figure 28: Evaluation of FLIM spectrogram reconstruction error – see Eq.(14) - via $FLIM_A$ (direct PL lifetime map) and $FLIM_B$ (frame-by-frame PL maps reconstruction) approach for a different amount of noise in a system (I_{PL} signal). Adapted from Junek et al. [49], Fig. 6.

Considering the exponential functions fitting issue, it is still important to deal with the problematics and find new approaches for determining function parameters, especially in noisy systems [57]. The possibility of accurately determining exponential parameters in the presence of noise would further improve the quality of both considered approaches. Nevertheless, the $FLIM_A$ approach is less time-consuming in post-processing than the $FLIM_B$. A more detailed description can be found in Junek et al. [49]. Based on our findings, we directed our work towards the search for methods to effectively extract individual PL components from the measured data. This effort is described in the following sections.

7 Direct determination of PL decay parameters

As mentioned in the previous text, the RATS method can be used to obtain the dynamics of PL decay I_D, which typically has a multi-exponential character in time (mono-exponential, bi-exponential, tri-exponential, …). For the sake of data interpretation, the PL lifetimes τ needs to be determined —typically through additional data processing by regression of a suitable exponential function (see Eq.(15), Eq.(16), and Fig. 29). In the case of multi-exponential decay, the overall lifetime can be determined via weighted averaging of partial lifetimes of decay (see right part of Eq.(16)). The regression process can be very time-consuming, especially for a 2D scene. Often, it depends on the experimenter, which exponential function (mono-, bi-, tri-) is used for the regression. Therefore, it is advisable to avoid this step and obtain precise information about the lifetime of PL τ directly from the measured data (random I_{EXC}/I_{PL} signals).

$$I_D = Ce^{-t/\tau}, \tag{15}$$

$$I_D = C_1 e^{-t/\tau_1} + C_2 e^{-t/\tau_2} \Rightarrow \tau = \frac{C_1\tau_1 + C_2\tau_2}{C_1 + C_2}. \tag{16}$$

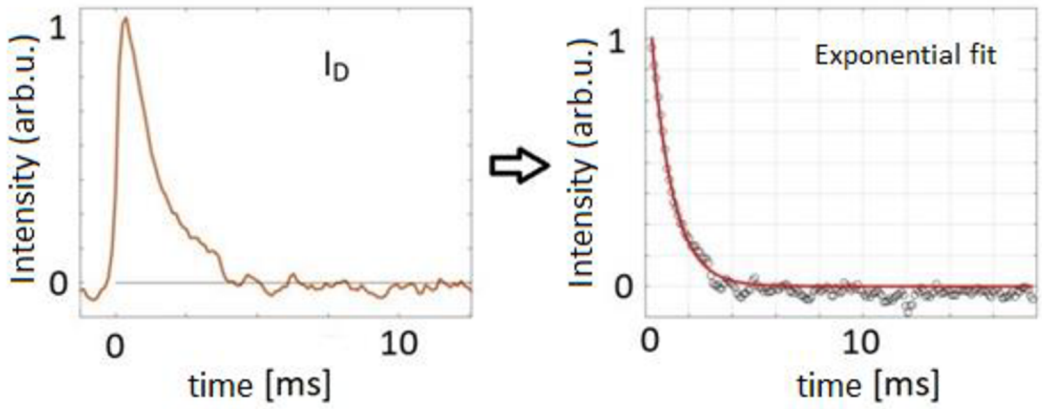

Figure 29: Left part: An example of I_D data by the RATS method. Right part: Fit of the I_D using a bi-exponential curve.

Moreover, it should be kept in mind that in general multi-exponential cases, the shape of the PL decays with two different multi-exponential components can be very similar [58]. This is summarized in Fig. 30, where the waveforms of two different bi-exponentials are compared. Then, even a small amount of noise can significantly distort the result. Therefore, the development of an algorithm that accurately determines the given parameters of the curve is of great importance.

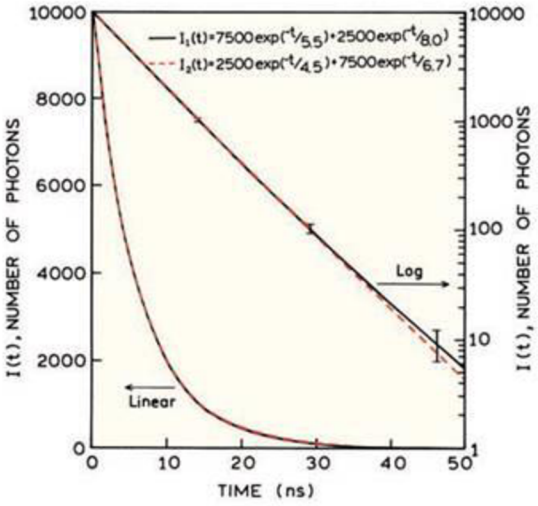

Figure 30: Comparison of the course of two bi-exponential curves in a linear scale (left part) and in a logarithmic scale (right part). Adapted from Lakowicz et al. [58].

7.1 Direct determination of decay parameters via undetermined system

The decay parameters (lifetimes, amplitudes) can be determined directly from the measured I_{EXC}/I_{PL} signals, i.e. without fitting the data, using computational algorithms for solving an undetermined system of linear equations when the sparse representation of τ is sought.

We state a matrix B, where each column of the matrix represents a single exponential:

$$B = \begin{pmatrix} \exp\left(\frac{t_1}{\tau_1}\right) & \cdots & \exp\left(\frac{t_1}{\tau_N}\right) \\ \vdots & \ddots & \vdots \\ \exp\left(\frac{t_n}{\tau_1}\right) & \cdots & \exp\left(\frac{t_n}{\tau_N}\right) \end{pmatrix}. \tag{17}$$

Let us also state the vector x, which has the number of elements N, with k-sparsity ($k \leq 3$) and has the meaning of the amplitude of the exponential. The result of B and x multiplication then has the meaning of I_D.

$$I_D = Bx\,. \tag{18}$$

After application of the Fourier transform to Eq.(2) and substitute Eq.(18) we get Eq.(19):

$$\mathbb{F}(I_{PL}) = \mathbb{F}(I_{EXC})\mathbb{F}Bx. \tag{19}$$

Let us denote the $\mathbb{F}B$ as the matrix V and consider that $\mathbb{F}(I_{PL})$ can be understood as a vector with n elements, denoted by w. We then multiply the vector w member by the member (element-wise product) by each of the N columns of the matrix V and obtain the measurement matrix A:

$$A = \begin{pmatrix} w_{(1)}V_{(1,1)} & \cdots & w_{(1)}V_{(1,N)} \\ \vdots & \ddots & \vdots \\ w_{(n)}V_{(n,1)} & \cdots & w_{(n)}V_{(n,N)} \end{pmatrix}. \tag{20}$$

All that remains is to denote the $\mathbb{F}(I_{PL})$ vector of size n as y, and we obtain the fundamental linear Eq.(21), where the vector x is assumed to be sparse:

$$y = Ax. \tag{21}$$

For simulation purposes, we define an exponential I_D and calculate the I_{PL} using the known I_{EXC}:

$$I_D = C_1 e^{-t/\tau_1} + C_2 e^{-t/\tau_2} + C_3 e^{-t/\tau 3}, \tag{22}$$

$$I_{PL} = \mathbb{F}^{-1}\left(\mathbb{F}\left(I_{EXC}\right)\mathbb{F}\left(I_D\right)\right). \tag{23}$$

7.1.1 Simulation of undetermined system-based algorithm

Before starting the simulation process, it is necessary to define the assumed set τ of N members and generate the matrix B. Furthermore, the known (measured) signal I_{EXC} and the calculated I_{PL} are used to obtain the matrix A and the vector y. Then the following steps proceed:

1. In order to obtain an undetermined system, we randomly select M rows of matrix A and the corresponding M elements of the vector y ($M<N$). Since the algorithm used is intended for calculations with real numbers, we create a vector $y'=[Re(y); Im(y)]$. We do the same with the measurement matrix A, so we get $A'=[Re(A); Im(A)]$. However, then it must be satisfied that $N>2M$. Thus, an undetermined system, according to Eq.(24), enters the algorithm:

$$y' = A'x. \tag{24}$$

2. As a reconstruction algorithm, we used ROLS (Regularized Orthogonal Least Squares for sparse reconstruction). The ROLS belongs to the group of Greedy algorithms and searches for columns (atoms) with maximum energy [59, 60]. This algorithm was written by Angshul Majumdar (2009) and is available at Mathworks [61].

3. If no solution is found with k-sparsity ($k \leq 3$), it goes back to step 1. A new random selection of y (components of Fourier domain) and A of size M is defined.

In all cases, different M Fourier domain components of the I_{PL} signal enter into step 2 of the algorithm above. However, it has not yet been possible to find an ideal distribution of frequencies that

would guarantee convergence to the solution after the first iteration of the process. Nevertheless, after a few iterations, the process converges to the correct result within a few seconds of computational time. The duration depends on the number of lifetimes in the I_D. Results are shown in Fig. 31 and Fig. 32.

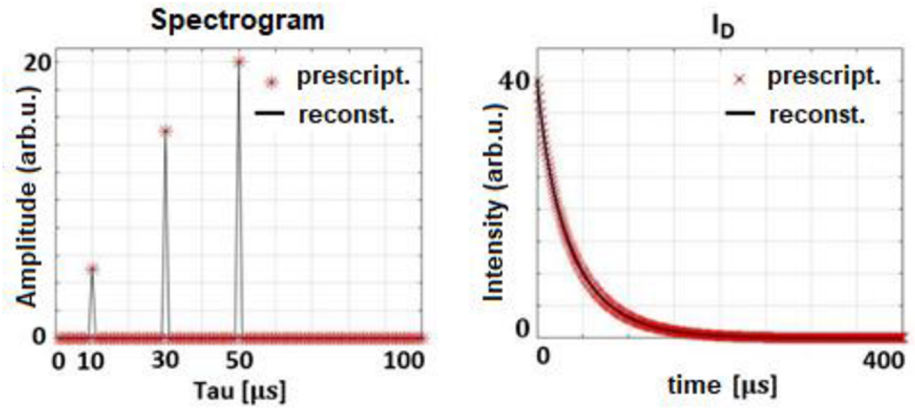

Figure 31: I_D reconstruction consisting of three exponentials with amplitudes - 5, 15, 20 and PL lifetimes τ - 10, 30, 50 µs.

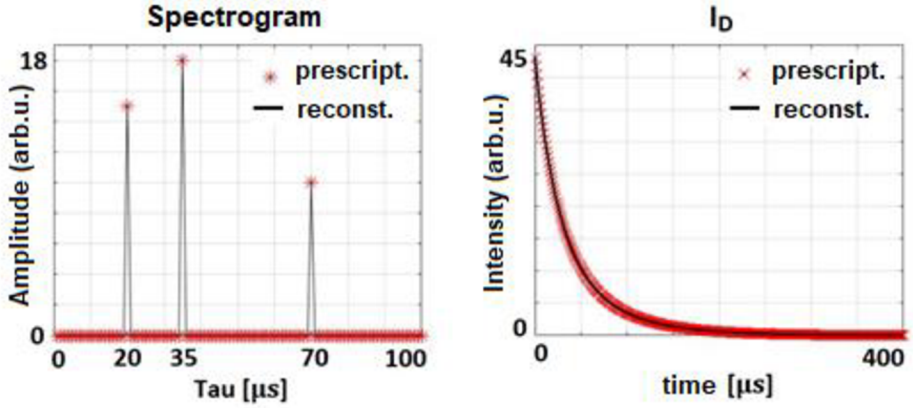

Figure 32: I_D reconstruction consisting of three exponentials with amplitudes - 15, 18, 10 and PL lifetimes τ - 20, 35, 70 µs.

Although many strategies of M Fourier domain components selection were tried, e.g., to favour the components with high amplitude in the Fourier spectrum, i.e. a higher signal-to-noise ratio – yet it was not possible to obtain a solution for systems with a realistic amount of noise. The solutions were obtained for systems with SNR > 78 dB. Once we simulate more noisy data, the algorithm fails to converge to the correct result.

The failure of the algorithm with noisy data is apparently caused by the inappropriateness of matrix A, whose randomness is lost due to the character of matrix B. In the ideal case of matrix A, a completely different I_{EXC} (different w) for each τ (column of matrix B) should be ensured. However, this is apparently

impossible to ensure in realistic experimentation conditions. Therefore, we turned to a different approach to retrieve the PL lifetimes.

7.2 Direct determination of PL decay parameters using neural network

The issue of PL lifetime retrieval was also investigated using deep learning and neural networks (NN) as an alternative to the previous algorithms. The problem can be defined as a search for the correct lifetimes from a list of possible options. Therefore, the so-called "multi-task learning" approach was implemented. The multi-task learning is typically used to recognize multiple objects in the image -- e.g. during image analysis in autonomous vehicles [62]. Since the extensive topic of NN reaches far beyond the scope of the thesis, we present the solution as a possible way of investigation, which adequately represents proof of principle.

The training and testing datasets in this subsection are purely synthetic simulated data which reliably copy the real experiment. Nevertheless, the results show that the introduced NN solution can provide satisfying results despite its simplicity.

7.2.1 Problem definition and datasets interpretation

In this part, we describe our search for direct determination of PL lifetimes of two decay components in a noisy dataset using NN. The retrieval was carried out from the RATS I_{PL} signal with a random character without prior knowledge of the spectrum of lifetimes τ.

Data (I_{PL} signals) were generated according to Eq.(2), assuming the same I_{EXC} pattern for all simulations. White noise was then added to the I_{PL} so that the noise level corresponded to a random 1/SNR value selected from the 0-1% range. In training and testing datasets, we considered only bi-exponential decays, i.e. two present lifetimes τ_1 and τ_2, with a random distribution of amplitudes A_1 and A_2 (see Eq.(4)).

For the sake of simplicity and as proof of the principle, the NN was always trained for a set of 5 lifetimes τ, picked from the interval 1-100 μs. The choice of units does not play here an important role as the temporal scaling of data can be arbitrary in the simulations. The output of NN was 6 neurons. Neurons 1-5 represented the investigated lifetimes, and the sixth neuron represented any other lifetime. The training dataset consisted of X = 216 000 simulated traces, where X/6 traces from the data belonged to each investigated lifetime. The same amount of data (X/6) also belonged to the I_{PL} with a different lifetime (6th neuron). The data in the testing dataset was distributed according to the same logic, where the total number of data was Y = 24 000.

Two cases were explored. In the first case, the training and testing datasets contained closely spaced lifetimes from a selected interval (τ_1 = 20 μs τ_2 = 21 μs τ_3 = 22 μs τ_4 = 23 μs τ_5 = 24 μs). In the second case, the datasets contained more distinct lifetimes within the interval 1-100 μs, namely τ_1 = 5 μs τ_2 = 23 μs τ_3 = 40 μs τ_4 = 58 μs τ_5 = 75 μs. Due to the facts mentioned in the previous sections, determining adjacent

lifetimes (the first case) in noisy data is a significantly more difficult task, and it is often problematic or impossible to solve using commonly used methods [57, 58].

The training of the NN in this work was based on the assumption that the same random excitation pattern I_{EXC} is used all the time, which might be approached in practice using a digital modulation of the laser. Therefore, a random digital signal (see Section 4.3) was used for generating the training and testing datasets. The signal featured a length of 10 ms and a width of IRF = 2.5 μs.

7.2.2 NN architecture

Keras and Tensorflow libraries were used to create the NN model based on 1D convolutional neural networks (1D-CNN). In each layer of 1D-CNN, it is possible to choose a number of filters with an optional convolutional kernel size. Several different architectures were tested. Nevertheless, the best results were achieved for the configuration sketched in Fig. 33, which is used throughout this section. We applied three convolutional layers with a descending number of filters, i.e. 12, 6, 3 using kernel size s = 3. After the individual convolutional layers, an average pooling is always implemented with a pooling size p matching the convolutional kernel size $p = s$. The functionality of the average pooling layer lies in averaging p consecutive inputs. The output is a list of averaged values so that the number of output values is p-times reduced compared to the input. Therefore, e.g., the first average pooling layer reduces 12 288 inputs to 4 096 outputs (see Fig. 33).

The combination of convolutional and average pooling layers is repeated three times in a sequence. Then, the application of flatten function creates a so-called fully connected (FC) layer from the convolution block. The penultimate FC layer has 100 neurons, while the output FC layer has 6 neurons (the number matches the number of searched lifetimes - see 7.2.1). Between the last layer of average pooling and flatten, as well as between flatten and the penultimate FC layer were implemented a dropout function with a rate of 0.2. The dropout function with a rate of 0.2 disables the input of 20% of randomly selected neurons in the following layer in each iteration. Dropout serves as a regularization element that prevents NN overlearning [63].

Overlearning is an unwanted effect, which manifests itself in the fact that the accuracy of the training and testing datasets significantly differs. The NNs then usually feature high accuracy on the training dataset, while the testing dataset is significantly worse. The difference in the accuracy of the training and testing dataset is called variance.

The ReLu function was selected as an activation function within the entire NN model except for the output layer, where a sigmoid activation function was applied. A binary cross-entropy loss function is chosen for the classification and evaluation of the problem, where each neuron within the last layer indicates the presence or absence of the corresponding lifetime.

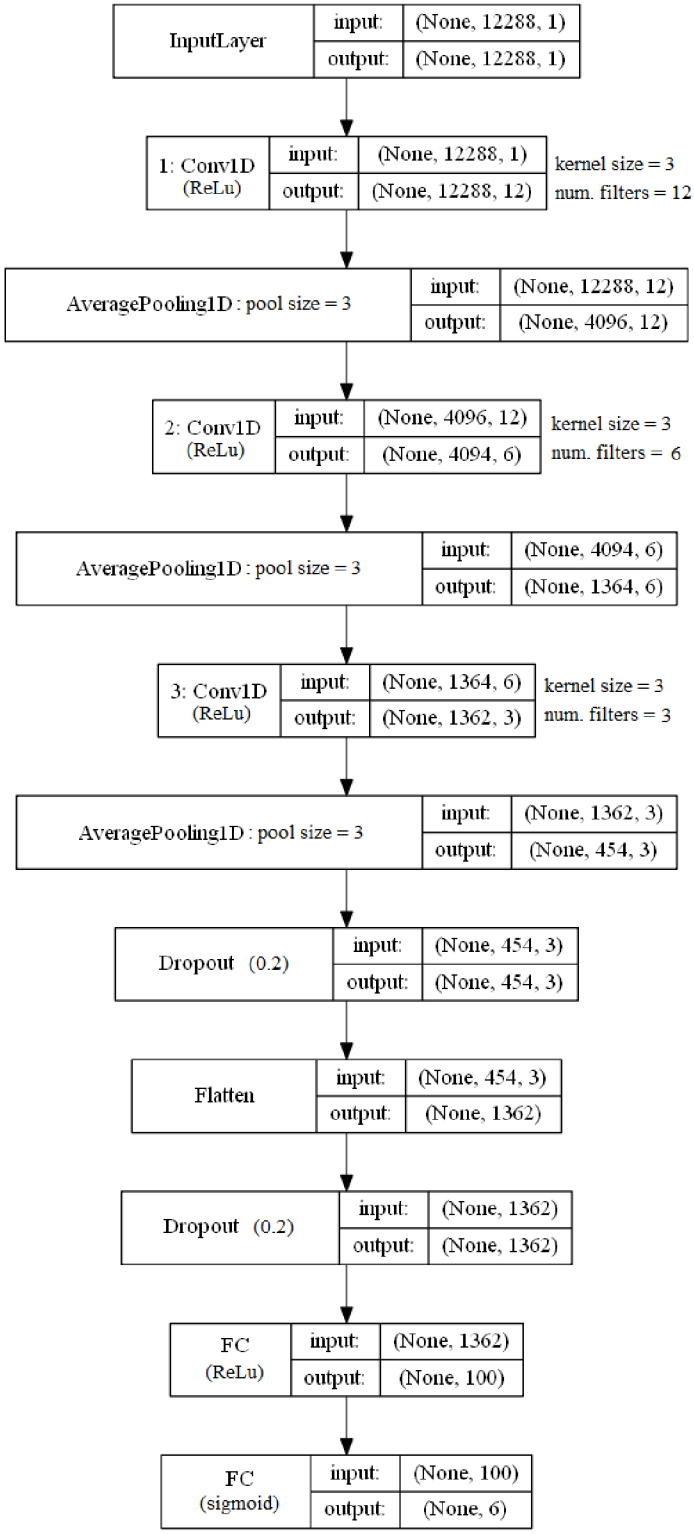

Figure 33: Architecture of used NN

NN training was performed using a mini-batch learning technique, which enables faster NN training [64]. This approach divides the entire dataset into small chunks (i.e. mini-batches) of a selected size. In our case, the batch size was chosen to be 16. The data corresponding to the batch size is then gradually submitted to the NN for training. One passage of all data through the training process is denoted as an epoch. The Adam optimizer with a learning rate of 10^{-3} was selected as a minimization algorithm, which suitably combines the Gradient descent with momentum and "RMSprop" (root-mean-square propagation) minimization methods [65].

7.2.3 NN results

The presented results were obtained after 20 epochs of training. As mentioned in the previous chapter, the training dataset always had 216 000 values and the testing 24 000 values.

The accuracy of the trained NN was evaluated by using two metrics following different approaches. The first one corresponds to the standard assessment of accuracy in multi-task learning, where all correctly predicted classes are included, regardless of whether the other classes were mispredicted. We denote such accuracy as $\sigma_{A,}$ and can be expressed using Eq.(25). θ_A is equal to the number of mispredictions in each class, n is the number of output neurons (number of all classes), and N is the number of data in the testing dataset.

$$\sigma_A = 1 - \frac{\theta_A}{nN}. \tag{25}$$

However, for practical reasons regarding the PL lifetime analysis, we are more interested in cases where the whole decay curve, i.e. both partial PL lifetimes, are determined precisely. Therefore, the cases where at least one output class (lifetime) was mispredicted are also included in the incorrectly determined dataset θ_B. So we denote the accuracy as σ_B, where N is again the number of values in the test set:

$$\sigma_B = 1 - \frac{\theta_B}{N}. \tag{26}$$

The resulting accuracy of the NN evaluations with close PL lifetimes (τ_1 = 20 μs τ_2 = 21 μs τ_3 = 22 μs τ_4 = 23 μs τ_5 = 24 μs) are shown in Fig. 34. The σ_A [%] accuracy is shown on the left-hand side, and the σ_B [%] accuracy on the is shown on the right-hand side. In the case of σ_A [%], we achieved after 20 epochs the accuracy of 97.8% on the training set and 94.6% on the testing set. The accuracy of the complete PL decay lifetime retrieval (σ_B [%]) reached 90.9% for the training set and 80.5% for the testing set.

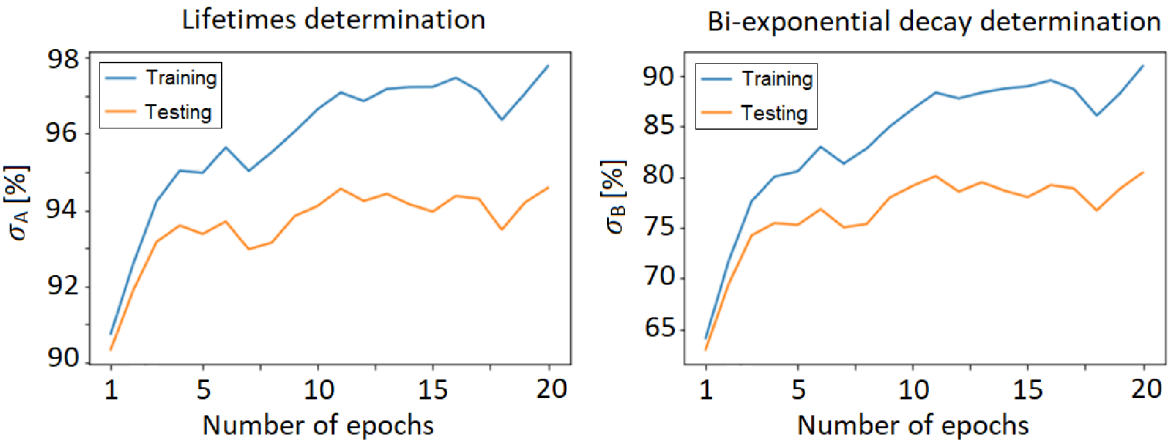

Figure 34: The case of close τ. Left side: σ_A [%] accuracy depending on the number of epochs. Right side: σ_B [%] accuracy depending on the number of epochs.

Fig. 35, on the left-hand and right-hand side, illustrates how the accuracy σ_A [%] and σ_B [%], respectively, depends on the amount of added noise. All of the accuracies in Fig. 35 are listed for the testing dataset only.

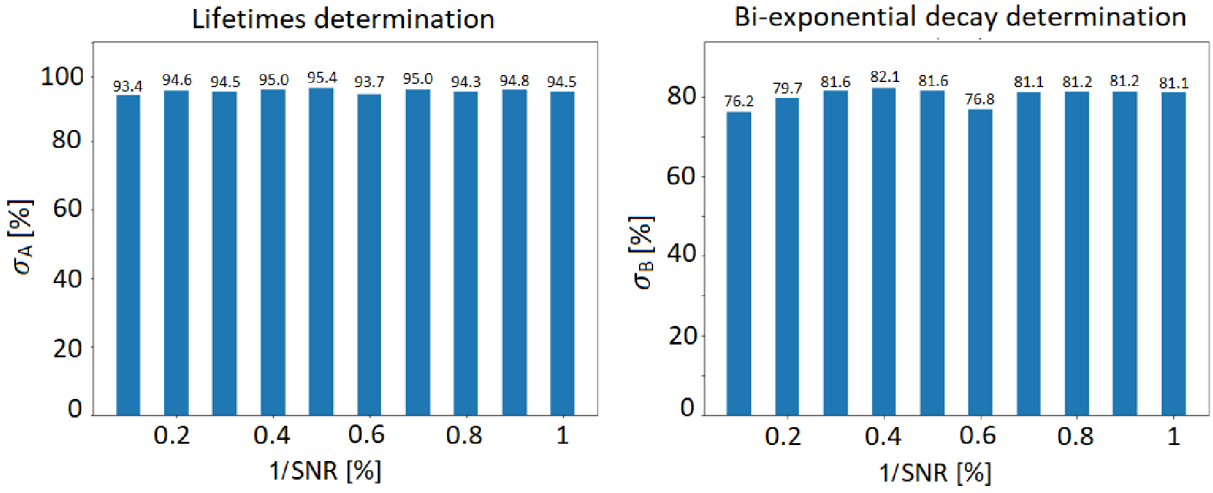

Figure 35: The case of close τ. Left part: The accuracy of individual lifetimes prediction (testing dataset) as a function of noise in the system. Right part: The accuracy of the exact determination of the decay curve (testing dataset) depends on the noise in the system.

The same simulations were carried out for the second above-stated dataset of more distinct PL lifetimes covering a large interval ($\tau_1 = 5$ µs $\tau_2 = 23$ µs $\tau_3 = 40$ µs $\tau_4 = 58$ µs $\tau_5 = 75$ µs). In the case of σ_A [%], we achieved after 20 epochs the accuracy of 96.2% on the training set and 95.3% on the testing set. The accuracy of the complete PL decay lifetime retrieval (σ_B [%]) reached 84.6% for the training set and 81.9%

for the testing set. Analogously, we also studied the role of noise on lifetime retrieval. The results are shown in Fig. 36 and Fig. 37.

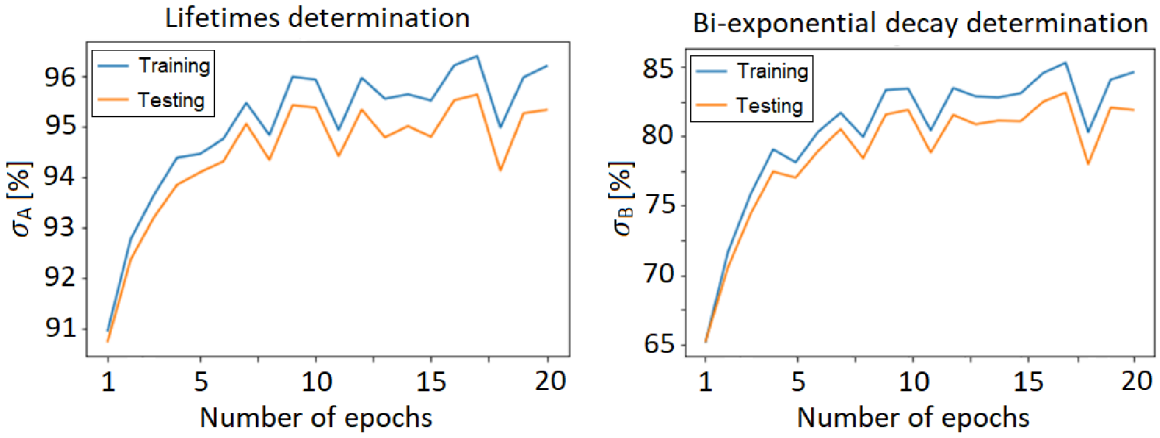

Figure 36: The case of remote τ. Left side: σ_A [%] accuracy depending on the number of epochs. Right side: σ_B [%] accuracy depending on the number of epochs.

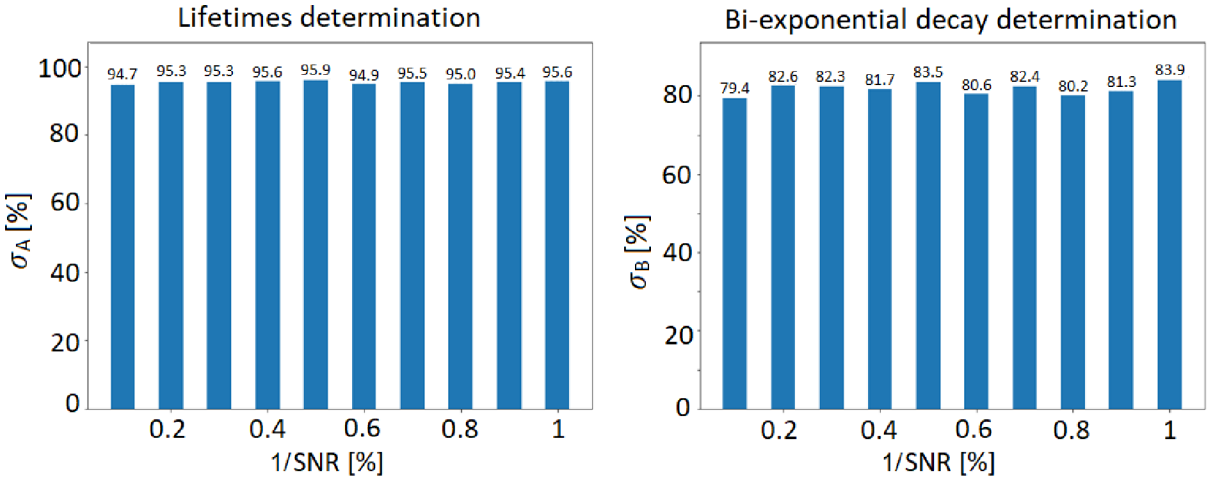

Figure 37: The case of remote τ. Left part: The accuracy of individual lifetimes prediction (testing dataset) as a function of noise in the system. Right part: The accuracy of the exact determination of the decay curve (testing dataset) depends on the noise in the system.

7.2.4 NN results discussion

Solving the problem using NN is presented as an alternative for determining the lifetimes τ in noisy I_{PL} data. It is worth mentioning that NN architecture can be further optimized and that better results can also be achieved by simply increasing the number of training datasets.

We are aware that it would be appropriate here to compare the obtained results of a given NN with the accuracy of regression using fitting algorithms depending on the noise. However, this is not a

simple task in the case of bi-exponential decay. It is necessary to realize that trained NN with the indicated accuracy of prediction points to completely accurate results. However, by fitting, we usually get an approximate result, which can greatly deviate from the prescription in situations with a high level of noise. The above-mentioned holds especially for a multi-exponential decay (see Fig. 30).

For a rigorous verification, it would be necessary to define the neighbourhood of the fitted value (interval), which would mark the approximate value that falls within the given neighbourhood as exact. That will be a valid verification approach if the activation function (sigmoid) of the output neuron has the same threshold as the neighbourhood of the fitted value. The threshold of the sigmoid activation function determines whether the given lifetime is present or not (that is, whether the output will be 1 or 0). However, determining the size of the neighbourhood of the value (interval) for fitting, based on the input values to the activation function or its threshold, is not a trivial task. Nevertheless, in the near future, we plan to deal with the issue and find out whether the given comparison is possible.

From the point of view of realistic measurement, it is clear that a broad interval of the lifetime spectrum needs to be covered for an arbitrary sample. Moreover, it is reasonable to expect a wider lifetime spectrum than we used in our simulations (1-100 μs)). This can be solved by expanding the number of output neurons (more searched lifetimes τ), which will change the NN architecture and increase the number of optimizable parameters. However, the situation can also be solved by training a higher amount of the same NN models, each covering a different part of the spectrum. Considering the above-reported results, training for remote lifetimes in the search spectrum (the second case) is more appropriate.

Overall, the results in both training cases (the first case expects close and the second remote lifetimes in the search spectrum) clearly show that by using NN, the accuracy of determining decay lifetimes does not necessarily deteriorate for the noisy cases (tested 0-1%), as it is with standard algorithms. These findings are important not only for spectrometry dealing with photoluminescence dynamics but also for a wide range of other disciplines where the exponential fitting is essential, e.g., cavity ring-down spectrometry or high reflectance coating measurements [66,67].

8 Conclusion

The RATS method was presented as a new method for PL decay measurement, which was fully developed during my Ph.D. study. The method can be used in a single-point measurement (0D-RATS) but also in the imaging mode (2D-RATS), which finds application in fluorescence lifetime imaging (FLIM). The method was successfully verified with the streak camera and TCSPC [46,47].

The demonstration experiments of two implementations of the RATS method were presented in this thesis. In the first implementation, a random excitation signal was generated using a rotary diffuser, and illuminating masks were produced using a laterally moving diffuser (grayscale speckle mask). This implementation is straightforward and incomparably low-cost with respect to standard FLIM approaches. Nevertheless, it is very ineffective in using the excitation light intensity. The second implementation of 2D-RATS was a microscopic setup. It used a DMD to generate illuminating masks (binary masks), and the excitation signal was based on a randomly modulated diode laser. With this approach, it is possible to achieve a temporal resolution in the order of units of a nanosecond and spatial resolution on the micrometer scale.

Nevertheless, the main strength of the 2D-RATS method still lies in the lifetime imaging in a microsecond or a sub-microsecond timescale. The RATS acquisition in this timescale is fast compared to commonly used FLIM methods, such as TCSPC. Among other reasons, the acquisition time is shortened, also thanks to the use of compressed sensing. In the nanosecond timescale, optimized TCSPC setups using SPAD detectors still provide superior performance – on the other hand, their cost is an order of magnitude above the cost of a 2D-RATS microscopic implementation. If the RATS method was further optimized using a SPAD detector, it could achieve similar acquisition times as TCSPC while featuring a better versatility of the setup.

The acquisition speed of 2D-RATS depends on several factors. The crucial factor is the resolution of the reconstructed image and the related compression ratio. Another important factor is the level of PL intensity. This comes into play since FLIM spectrogram error is highly dependent on the PL intensity itself. Therefore, for a high PL intensity, faster sensing can be achieved by significantly reducing the acquisition time. Under ideal conditions, with a highly emitting sample (OG565 filter), it was possible to complete a measurement within the time of 6 minutes. More notably, this time was achieved for a setup without any optimization regarding the time required for the instrument control and data transfer, which together took the dominating portion of the acquisition time.

The thesis also describes two approaches for obtaining a FLIM spectrogram, which we called as $FLIM_A$ and $FLIM_B$. The $FLIM_A$ approach is chronologically younger, and it succeeded in avoiding the need for determining the PL decay curve and lifetime (via fitting) in each pixel separately as in $FLIM_B$. Hence,

the postprocessing routine is significantly speeded up. In addition, using $FLIM_{A,}$ it is possible to display the amplitude map directly for each partial lifetime, i.e. the distribution of partial lifetimes of multi-exponential decay within the sample.

An important step in the optimization of the RATS method was the analysis of the noise effect on PL data reconstruction. The analysis revealed a significantly higher sensitivity of the results towards the noise corrupting the measured PL signal I_{PL}. In general, the noise level in data turned out to be a key parameter of reconstruction quality, which cannot be effectively compensated by simply increasing the number of measurements, i.e. by increasing the compression ratio.

The simulations showed that an efficient way to significantly increase the signal-to-noise ratio is either a straightforward prolongation of the acquisition time or the possibility of choosing a suitable regularization parameter ε. In the case of prolonging acquisition for one I_{DA} reconstruction, it is necessary to consider a significant increase in the total measurement time. The choice of the regularization parameter ε is related to the noise level in the system since it smoothes the I_D/I_{DA} curve but also causes a slight distortion. Therefore, in situations with low noise, it is convenient to keep the regularization parameter at values $\varepsilon = 0.1$ or $\varepsilon = 0.2$. In the case of higher noises, it is adequate to choose a significantly higher ε. Simulations have shown that with the correct choice of regularization parameter and acquisition time, the RATS method can achieve results that are not distorted and can accurately map a 2D scene even with a relatively high noise level (3%).

The periodicity of the excitation signal I_{EXC} was discussed as part of the noise analysis. The attained data showed that periodicity decreases the signal-to-noise ratio. This issue arises due to the application of the deconvolution step in the PL decay retrieval. Since the original means of generation of the random signal was based on a rotating diffuser, the periodicity effect could play a significant role. Therefore, we replaced the original method with a randomly modulated laser with a random seed, which became a cornerstone of the so-called second generation of the 2D-RATS setup. Direct laser modulation turned out to be a better solution for the RATS systems.

Most of the insights gathered through the detailed noise analysis could be applied to both $FLIM_A$ and $FLIM_B$ reconstruction approaches. Although $FLIM_A$ and $FLIM_B$ are different, it is necessary to reconstruct the PL decay curve in both cases. The two different approaches to data treatment were compared through their FLIM spectrograms for noise levels of 0-1.5%. The $FLIM_A$ approach showed more accurate results in situations with higher noise levels than 0%.

Finally, we pursued the idea of creating an algorithm for the direct reconstruction of the PL decay parameters with the assumption of an undetermined system. The algorithm searched for a sparse solution and worked successfully in noiseless systems. However, in a situation with noise > 78 dB, the algorithm failed to converge to correct results due to the similarity of the different multi-exponential decays.

Therefore, the possibility of using neural networks (NN) with a multi-task learning approach was investigated. The NN model was built on a 1D convolutional neural network (CNN), assuming a limited number of searched lifetimes τ, noise presence from 0-1%, and considering only a bi-exponential decay system. Considering the difficulty of the issue, NN shows high accuracy in precise determining of PL decay curve. In addition, on the tested area of noise (0-1%), the results did not show any significant dependence on the accuracy of lifetime determination with respect to arising noise level. These findings would be beneficial for a wide range of other disciplines of spectrometry, where the exponential fitting is a fundamental part of the analysis, including, for instance, cavity ring-down spectrometry [66,67].

Overall, the thesis presents a novel robust time-resolved method RATS for studying PL dynamics. The method can be easily implemented into a FLIM measurement based on SPC configuration. In the search for a noise-resistant FLIM analysis, we developed two reconstruction strategies, where the direct extraction of decay lifetimes shows better noise stability and significantly reduces post-processing time. We verified that using trained NN, it is possible to determine the lifetime distribution of the bi-exponential system without the result being significantly affected by the amount of present noise (0-1%).

Reference

[1] I. Pelant and J. Valenta, *Luminescence Spectroscopy of Semiconductors* (Oxford University, 2012).

[2] R. M. Clegg and P. C. Schneider, "Fluorescence Lifetime-Resolved Imaging Microscopy: A General Description of Lifetime-Resolved Imaging Measurements," in *Fluorescence Microscopy and Fluorescent Probes*, J. Slavík, ed. (Springer, US, 1996).

[3] L. Foglia, S. Vempati, B. Tanda Bonkano, L. Gierster, M. Wolf, S. Sadofev, and J. Stähler, "Revealing the competing contributions of charge carriers, excitons, and defects to the non-equilibrium optical properties of ZnO," Struct. Dyn. **6**(3), 034501 (2019).

[4] K. Žídek, F. Trojánek, P. Malý, L. Ondič, I. Pelant, K. Dohnalová, L. Šiller, R. Little, and B. R. Horrocks, "Femtosecond luminescence spectroscopy of core states in silicon nanocrystals," Opt. Express **18**(24), 25241–25249 (2010).

[5] A. Lavie-Cambot, C. Lincheneau, M. Cantuel, Y. Leydet, and N. D. McClenaghan, "Reversible electronic energy transfer: a means to govern excited-state properties of supramolecular systems," Chem. Soc. Rev. **39**(2), 506–515 (2010).

[6] K. Kůsová, O. Cibulka, K. Dohnalová, I. Pelant, J. Valenta, A. Fučíková, K. Žídek, J. Lang, J. Englich, P. Matějka, P. Štěpánek, and S. Bakardjieva, "Brightly Luminescent Organically Capped Silicon Nanocrystals Fabricated at Room Temperature and Atmospheric Pressure," ACS Nano **4**(8), 4495–4504 (2010).

[7] A. Fojtik and A. Henglein, "Surface Chemistry of Luminescent Colloidal Silicon Nanoparticles," J. Phys. Chem. B **110**(5), 1994–1998 (2006).

[8] K. Zheng, K. Žídek, M. Abdellah, M. E. Messing, M. J. Al-Marri, and T. Pullerits, "Trap States and Their Dynamics in Organometal Halide Perovskite Nanoparticles and Bulk Crystals," J. Phys. Chem. C **120**(5), 3077–3084 (2016).

[9] P. I. H. Bastiaens and A. Squire, "Fluorescence lifetime imaging microscopy: spatial resolution of biochemical processes in the cell," Trends Cell Biol. **9**(2), 48–52 (1999).

[10] J. M. Griffin, A. J. Miller, A. J. Berry, S. Wimperis, and S. E. Ashbrook, "Dynamics on the microsecond timescale in hydrous silicates studied by solid-state 2H NMR spectroscopy," Phys. Chem. Chem. Phys. **12**(12), 2989–2998 (2010).

[11] K. Dohnalová, L. Ondič, K. Kůsová, I. Pelant, J. L. Rehspringer, and R.-R. Mafouana, "White-emitting oxidized silicon nanocrystals: Discontinuity in spectral development with reducing size," J. Appl. Phys. **107**(5), 053102 (2010).

[12] D. Lin and W. Ma, "Single molecule fluorescence imaging within living cells," PHYSICS-BEIJING- **36**, 783 (2007).

[13] W. Becker, "Fluorescence lifetime imaging – techniques and applications," Journal of Microscopy **247**, 119–136 (2012).

[14] J. A. Levitt, D. R. Matthews, S. M. Ameer-Beg, and K. Suhling, "Fluorescence lifetime and polarization-resolved imaging in cell biology," Current Opinion in Biotechnology **20**, 28–36 (2009).

[15] Q. Wu, J. Qi, D. Lin, W. Yan, R. Hu, X. Peng, and J. Qu, "Simultaneous acquisition of trajectory and fluorescence lifetime of moving single particles," in *Multiphoton Microscopy in the Biomedical Sciences XVII* (SPIE, 2017), **10069**, 269–273.

[16] P. Knotek, L. Tichy, D. Arsova, Z. G. Ivanova, and H. Ticha, "Irreversible photobleaching, photorefraction and photoexpansion in GeS2 amorphous film," Materials Chemistry and Physics **119**, 315–318 (2010).

[17] X. Liu, D. Lin, W. Becker, J. Niu, B. Yu, L. Liu, and J. Qu, "Fast fluorescence lifetime imaging techniques: A review on challenge and development," J. Innov. Opt. Health Sci. **12**, 1930003 (2019).

[18] N. Krstajić, S. Poland, J. Levitt, R. Walker, A. Erdogan, S. Ameer-Beg, and R. K. Henderson, "0.5 billion events per second time correlated single photon counting using CMOS SPAD arrays," Opt. Lett., OL **40**, 4305–4308 (2015).

[19] J. V. Thompson, J. D. Mason, H. T. Beier, and J. N. Bixler, "High speed fluorescence imaging with compressed ultrafast photography," in *High-Speed Biomedical Imaging and Spectroscopy: Toward Big Data Instrumentation and Management II* (SPIE, 2017), **10076**, 74–79.

[20] J. Sytsma, J. M. Vroom, D. Grauw, and H. C. Gerritsen, "Time-gated fluorescence lifetime imaging and microvolume spectroscopy using two-photon excitation," J. Microsc. **191**(1), 39–51 (2008).

[21] R. V. Krishnan, H. Saitoh, H. Terada, V. E. Centonze, and B. Herman, "Development of a multiphoton fluorescence lifetime imaging microscopy system using a streak camera," Rev. Sci. Instrum. **74**(5), 2714–2721 (2003).

[22] S. Cheng, R. M. Cuenca, B. Liu, B. H. Malik, J. M. Jabbour, K. C. Maitland, J. Wright, Y.-S. L. Cheng, and J. A. Jo, "Handheld multispectral fluorescence lifetime imaging system for in vivo applications," Biomed. Opt. Express **5**(3), 921–931 (2014).

[23] A. D. Elder, C. F. Kaminski, and J. H. Frank, "ϕ^2FLIM: a technique for alias-free frequency domain fluorescence lifetime imaging," Opt. Express **17**(25), 23181–23203 (2009).

[24] W. Becker, A. Bergmann, G. Biscotti, K. Koenig, I. Riemann, L. Kelbauskas, and C. Biskup, "High-speed FLIM data acquisition by time-correlated single-photon counting," Proc. SPIE **5323**, 27–35 (2004).

[25] N. Krstajić, S. Poland, J. Levitt, R. Walker, A. Erdogan, S. Ameer-Beg, and R. K. Henderson, "0.5 billion events per second time correlated single photon counting using CMOS SPAD arrays," Opt. Lett. **40**(18), 4305–4308 (2015).

[26] E. P. Buurman, R. Sanders, A. Draaijer, H. C. Gerritsen, J. J. F. van Veen, P. M. Houpt, and Y. K. Levine, "Fluorescence lifetime imaging using a confocal laser scanning microscope," Scanning **14**, 155–159 (1992).

[27] R. V. Krishnan, H. Saitoh, H. Terada, V. E. Centonze, and B. Herman, "Development of a multiphoton fluorescence lifetime imaging microscopy system using a streak camera," Review of Scientific Instruments **74**, 2714–2721 (2003).

[28] S. Cheng, R. M. Cuenca, B. Liu, B. H. Malik, J. M. Jabbour, K. C. Maitland, J. Wright, Y.-S. L. Cheng, and J. A. Jo, "Handheld multispectral fluorescence lifetime imaging system for in vivo applications," Biomed. Opt. Express, BOE **5**, 921–931 (2014).

[29] C. Huber, I. Klimant, C. Krause, and O. S. Wolfbeis, "Dual Lifetime Referencing as Applied to a Chloride Optical Sensor," Anal. Chem. **73**, 2097–2103 (2001)

[30] R. Tibshirani, "Regression Shrinkage and Selection Via the Lasso," Journal of the Royal Statistical Society: Series B (Methodological) **58**, 267–288 (1996).

[31] S. G. Mallat and Z. Zhang, "Matching pursuits with time-frequency dictionaries," IEEE Transactions on Signal Processing **41**, 3397–3415 (1993).

[32] P. L. Combettes and J.-C. Pesquet, "Proximal Splitting Methods in Signal Processing," in *Fixed-Point Algorithms for Inverse Problems in Science and Engineering*, H. H. Bauschke, R. S. Burachik, P. L. Combettes, V. Elser, D. R. Luke, and H. Wolkowicz, eds., Springer Optimization and Its Applications (Springer, 2011), pp. 185–212.

[33] P. Sen, B. Chen, G. Garg, S. R. Marschner, M. Horowitz, M. Levoy, and H. P. A. Lensch, "Dual photography," in *ACM SIGGRAPH 2005 Papers*, SIGGRAPH '05 (Association for Computing Machinery, 2005), pp. 745–755.

[34] G. M. Gibson, G. M. Gibson, S. D. Johnson, S. D. Johnson, M. J. Padgett, and M. J. Padgett, "Single-pixel imaging 12 years on: a review," Opt. Express, OE **28**, 28190–28208 (2020).

[35] Don and M. L, *Designing for Compressive Sensing: Compressive Art, Camouflage, Fonts, and Quick Response Codes* (US Army Research Laboratory, 2018).

[36] V. Studer, J. Bobin, M. Chahid, H. S. Mousavi, E. Candes, and M. Dahan, "Compressive fluorescence microscopy for biological and hyperspectral imaging," Proc. Natl. Acad. Sci. U. S. A. **109**(26), E1679–E1687 (2012).

[37] Q. Pian, R. Yao, N. Sinsuebphon, and X. Intes, "Compressive hyperspectral time-resolved wide-field fluorescence lifetime imaging," Nat. Photonics **11**(7), 411–414 (2017).

[38] R. Yao, M. Ochoa, P. Yan, and X. Intes, "Net-FLICS: fast quantitative wide-field fluorescence lifetime imaging with compressed sensing – a deep learning approach," Light Sci Appl **8**, 26 (2019).
[39] L. Gao, J. Liang, C. Li, *W. Lihong,* "Single-shot compressed ultrafast photography at one hundred billion frames per second". Nature **516**, 74–77 (2014).
[40] J. V. Thompson, J. D. Mason, H. T. Beier, and J. N. Bixler, "High speed fluorescence imaging with compressed ultrafast photography," in *High-Speed Biomedical Imaging and Spectroscopy: Toward Big Data Instrumentation and Management II* (SPIE, 2017), **10076**, 74–79.
[41] S. Yang, J. Lee, Y. Lee, M. Lee, and B.-U. Lee, "Estimation of multiexponential fluorescence decay parameters using compressive sensing," JBO **20**, 096003 (2015).
[42] V. Zickus, M.-L. Wu, K. Morimoto, V. Kapitany, A. Fatima, A. Turpin, R. Insall, J. Whitelaw, L. Machesky, C. Bruschini, D. Faccio, and E. Charbon, "Fluorescence lifetime imaging with a megapixel SPAD camera and neural network lifetime estimation," Sci Rep **10**, 20986 (2020).
[43] J. T. Smith, R. Yao, N. Sinsuebphon, A. Rudkouskaya, N. Un, J. Mazurkiewicz, M. Barroso, P. Yan, and X. Intes, "Fast fit-free analysis of fluorescence lifetime imaging via deep learning," Proceedings of the National Academy of Sciences **116**, 24019–24030 (2019).
[44] A. N. Tikhonov and V. Y. Arsenin, "Solutions of ill-posed problems," SIAM Rev. **21**, 266–267 (1977).
[45] F. Gascón and F. Salazar, "A simple method to simulate diffraction and speckle patterns with a PC," Optik **117**(2), 49–57 (2006).
[46] J. Junek, L. Ondič, and K. Žídek, "Random temporal laser speckles for the robust measurement of sub-microsecond photoluminescence decay," Opt. Express, OE **28**, 12363–12372 (2020).
[47] J. Junek, and K. Žídek, "Fluorescence lifetime imaging via spatio-temporal speckle patterns in a single-pixel camera configuration," Opt. Express, OE **29**, 5538–5551 (2021).
[48] G. Marsaglia, "Xorshift RNGs," Journal of Statistical Software 8, 1–6 (2003).
[49] J. Junek and K. Žídek, " Nanosecond compressive fluorescence lifetime microscopy imaging via the RATS method with a direct reconstruction of lifetime maps," arXiv: 2208.13640v3 [physics] (2022).
[50] J. Junek, and K. Žídek, "Noise effect on 2D photoluminescence decay analysis using the RATS method in a single-pixel camera configuration," Opt. Express, OE **30**(8), 12654–12669 (2022).
[51] K. A. Selanger, J. Falnes, and T. Sikkeland, "Fluorescence lifetime studies of Rhodamine 6G in methanol," J. Phys. Chem. **81**(20), 1960–1963 (1977).
[52] C. Li, Wotao Yin, and Yin Zhang, TVAL3 Home, Rice University, 2009, Last updated 11/07/2013, (available from: https://www.caam.rice.edu/~optimization/L1/TVAL3/).
[53] C. Li, W. Yin, and Y. Zhang, "User's guide for TVAL3: TV minimization by augmented lagrangian and alternating direction algorithms," CAAM Rep.20, 46–47 (2009).
[54] C. Li, "An Efficient Algorithm For Total Variation Regularization with Applications to the Single Pixel Camera and Compressive Sensing," Master Thesis, Rice University (2009).
[55] Yu. Zorenko, V. Gorbenko, A. Voloshinovskii, G. Stryganyuk, V. Mikhailin, V. Kolobanov, D. Spassky, M. Nikl, and K. Blazek, "Exciton-related luminescence in LuAG:Ce single crystals and single crystalline films," physica status solidi (a) 202, 1113–1119 (2005).
[56] M. Nikl, "Energy transfer phenomena in the luminescence of wide band-gap scintillators," physica status solidi (a) 202, 201–206 (2005).
[57] A. A. Istratov and O. F. Vyvenko, "Exponential analysis in physical phenomena," Review of Scientific Instruments 70, 1233–1257 (1999)
[58] J. R. Lakowicz, *Principles of Fluorescence Spectroscopy* (Springer US, 1983).
[59] T. Blumensath and M. Davies, "On the difference between orthogonal matching pursuit and orthogonal least squares," (2007).
[60] D. Needell and R. Vershynin, "Signal Recovery From Incomplete and Inaccurate Measurements Via Regularized Orthogonal Matching Pursuit," IEEE Journal of Selected Topics in Signal Processing **4**, 310–316 (2010).

[61] Orthogonal Least Squares Algorithms for Sparse Signal Reconstruction [Accessed 25 January 2021]. Available from: [online].
[62] S. Chowdhuri, T. Pankaj, and K. Zipser, "MultiNet: Multi-Modal Multi-Task Learning for Autonomous Driving," in *2019 IEEE Winter Conference on Applications of Computer Vision (WACV)* (2019), pp. 1496–1504.
[63] Baldi and P. J. Sadowski, "Understanding Dropout," in *Advances in Neural Information Processing Systems* (Curran Associates, Inc., 2013), Vol. 26.
[64] M. Li, T. Zhang, Y. Chen, and A. J. Smola, "Efficient mini-batch training for stochastic optimization," in Proceedings of the 20th ACM SIGKDD International Conference on Knowledge Discovery and Data Mining, KDD '14 (Association for Computing Machinery, 2014), pp. 661–670.
[65] D. P. Kingma and J. Ba, "Adam: A Method for Stochastic Optimization," in (2014).
[66] K. Lehmann, "An Introduction to Cavity Ring-Down Spectroscopy," Cavity Ring-Down Spectroscopy (2009).
[67] H. Zu, B. Li, Y. Han, and L. Gao, "Combined cavity ring-down and spectrophotometry for measuring reflectance of optical laser components," Opt. Express, OE **21**, 26735–26741 (2013).

Annexes

Here we provide the original prints of the manuscripts described in the Chapter: List of included publications. These four articles are the core of the thesis. The articles are in the following order - A, B, C, D. In the same order, they were also completed and published.

The first three articles were published in the journal Optics Express - [A] in 2020, [B] in 2021, and [C] in 2022. The last of the articles [D] is now available as a preprint, but at the same time, it is in Peer review in Optic Express journal.

List of annexes

Research Article Vol. 28, No. 8 / 13 April 2020 / Optics Express 12363
Optics EXPRESS

Random temporal laser speckles for the robust measurement of sub-microsecond photoluminescence decay

J. JUNEK,[1,2] L. ONDIČ,[3] AND K. ŽÍDEK[1,*]

[1]Regional Center for Special Optics and Optoelectronic Systems (TOPTEC), Institute of Plasma Physics, Czech Academy of Science v.v.i., Za Slovankou 1782/3, 182 00 Prague 8, Czech Republic
[2]Technical University in Liberec, Faculty of Mechatronics, Informatics and Interdisciplinary Studies, Studentská 1402/2, 461 17 Liberec, Czech Republic
[3]Institute of Physics, Czech Academy of Sciences v.v.i., Cukrovarnická 10, 162 53, Prague 6, Czech Republic
*zidek@ipp.cas.cz

Abstract: Time-resolved photoluminescence (PL) is commonly used to track dynamics in a broad range of materials. Thus, the search for simplification of the acquisition of PL kinetics attracts continuous attention. This paper presents a new robust and straightforward approach to the measurement of PL decay, which is based on randomly fluctuating excitation intensity. The random excitation waveform is attained by using laser speckles generated on a rotating diffuser. Owing to this, the presented technique is able to utilize any coherent excitation source without the necessity to generate short pulses or to controllably modulate the light. PL decay can be computationally reconstructed from the Fourier image of the PL trace. The paper demonstrates the performance of the method, which is able to acquire sub-microsecond dynamics as the impulse response function reaches 300 ns. The reconstructed PL decays were compared to streak camera measurements to verify the method. Finally, potential limitations and applications of the technique are discussed.

1. Introduction

Photoluminescence (PL) spectra and dynamics provide a vast amount of information about the emitting material – revealing energy levels of charge carriers [1,2], resolving processes governing the excited energy routes [3,4], even resolving lifetimes of the processes [5]. All the information can be extracted in a non-contact experiment, even in opaque samples. Therefore, PL time-resolved spectroscopy counts among the most used characterization methods in the fields of chemical physics [6,7], biochemistry [8], and material sciences in general.

All reported methods for time-resolved PL measurements require an excitation source able to provide us with a short pulse or to be controllably modulated [9–11]. In general, all the methods can be divided into two groups, which measure PL kinetics in the time and the frequency domains. Methods working in the time domain need a source producing correspondingly short pulses. The pulses excite PL, which is either detected by a speedy detection system, is spatially swept (streak camera), or the PL signal is gated (by up-conversion technique, iCCD). Measurements of PL decay in the frequency domain demand using a controllably modulated light intensity, for instance, an acousto-optic modulator or a modulated laser. In order to capture PL decay stretched over different timescales, the intensity modulation has to be facilitated over a broad range of frequencies.

In this article, we present a method that, in contrast, can use any source of coherent light to measure PL dynamics on the microsecond and sub-microsecond timescales. The core of this method lies in the excitation of the measured sample with a randomly fluctuating intensity of light. This can be achieved by transmitting a coherent light source through a rapidly varying scattering

#382811 https://doi.org/10.1364/OE.382811
Journal © 2020 Received 14 Nov 2019; revised 24 Mar 2020; accepted 26 Mar 2020; published 10 Apr 2020

Optics EXPRESS

element creating fluctuating speckle patterns, which we denote as temporal speckles. The field of temporal speckles is cropped with an aperture, providing us with a random signal for sample excitation. Such a random excitation signal features a broad range of frequencies, which can be used to reconstruct back the PL decay from the measured fluctuations of the PL intensity. We demonstrate that this technique can be used to attain PL decay with sub-microsecond temporal resolution without the need for a pulsed excitation. We also prove that the attained decay is in agreement with conventional approaches to PL decay measurement.

Moreover, as we show later, this method is remarkably robust against various experimental conditions such as signal delay or offset. Owing to its simplicity, no elaborate setup alignment or calibration is needed.

2. Methodology and experimental setup

2.1. Principles of the method

For the sake of brevity, we will hereafter denote the method as RATS (RAndom Temporal Speckles). The goal of the RATS method is to excite the tested sample with temporal speckles, i.e., randomly fluctuating intensity of light. To reconstruct the PL decay I_{decay} we need to acquire the excitation signal I_{Exc} and the PL signal I_{PL}. We can illustrate the RATS concept on simulated data depicted in Figs. 1(A)–1(B). The excitation signal was attained by simulating the generation of laser speckles from a rotating diffuser via Fraunhofer diffraction (far-field speckle pattern) [12]. Following the real experimental setup, which is described later, the resulting random pattern was cropped with an aperture and the total intensity of light within the aperture is plotted in Fig. 1(A) as a random signal for the excitation I_{Exc}. The photoluminescence signal I_{PL} plotted in Fig. 1(B) was calculated via the convolution of I_{Exc} and I_{decay}:

$$I_{PL} = I_{Exc} * I_{decay} \tag{1}$$

It is worth noting that Eq. (1) holds only for PL intensity which is linearly proportional to the excitation intensity, as we discuss later.

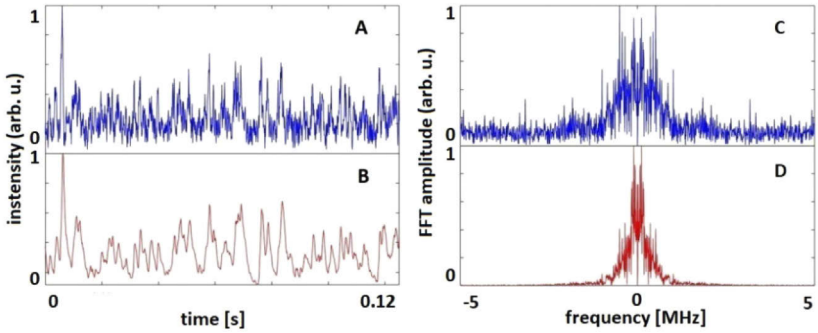

Fig. 1. Simulated intensity of the fluctuating temporal speckles (panel A) which are used to calculate a PL waveform (panel B). We assume a single-exponential PL decay with $\tau = 1$ ms. Fourier transform of intensity of fluctuating temporal speckles (panel C) and Fourier transform of PL waveform (panel D).

For the sake of clarity, the PL decay lifetime in Fig. 1 was chosen to be mono-exponential with the lifetime in the millisecond range ($\tau = 1$ ms), so that the difference between the excitation and the PL waveform is apparent both in the time domain and in the Fourier space. The Fourier transformations of I_{Exc} and I_{decay} are depicted in Figs. 1(C) and 1(D), respectively.

By using a fluctuating random signal for excitation, we get a wide range of frequencies in the Fourier space. This is important because the I_{decay} can be determined on the timescale

Optics EXPRESS

corresponding to the highest available frequency. The I_{decay} can be simply calculated via the convolution theorem. Equation (2) shows the used deconvolution applying the so-called Tikhonov regularization [13]. The regularization prevents cases from being ill-conditioned, which can happen when the denominator approaches zero due to data corrupted by noise.

$$I_{decay} = Re\left\{F^{-1}\left[\frac{F(I_{PL})\ F^{*}(I_{Exc})}{F(I_{Exc})F^{*}(I_{PL}) + \varepsilon\overline{F(I_{Exc})F^{*}(I_{Exc})}}\right]\right\} \tag{2}$$

We, therefore, attain the full PL decay dynamics I_{decay}, analogously to the other methods. The decay can be subsequently fitted with a set of exponential functions to determine the characteristic PL lifetimes.

Naturally, since the temporal speckle pattern is formed by a rotating diffuser, excitation and PL waveforms repeat with every period of rotation. Nevertheless, for the purpose of the PL decay retrieval, we do not need to determine the frequency of the diffuser and its timing, i.e., phase. This is owing to the fact that the shift in the "zero time" between the PL and the excitation data will cause the PL decay to be multiplied with a constant complex number $e^{(-i\varphi)}$, where the phase φ will scale with the timing difference. Such a problem can be easily eliminated.

2.2. Optical setup

A scheme of the optical setup used is presented in Fig. 2. In the setup, we used a cw laser (Sapphire, Coherent) at the wavelength of 488 nm, intensity 6 mW. But it should be stressed that one can use any coherent light source which is suitable for excitation of a sample. A diffuser (ground glass, diameter 10 cm, average grain size 1.52 µm) was mounted on a Mitsumi DC motor, which rotated up to the frequency of 65 Hz.

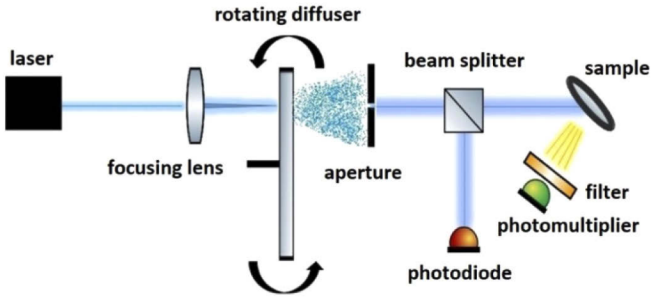

Fig. 2. Scheme of the experimental setup used.

The laser beam was focused onto the diffuser with a lens with a focal length of 30 mm. The laser beam hit the spinning diffuser 4.8 cm from the center and the beam spot size on the diffuser was approximately 50 µm. Under those conditions, we generated speckle patterns in the so-called far-field regime, which means that the generated intensity pattern does not change with distance.

The field of speckles was cropped with an iris aperture at the distance of 110 mm from the diffuser. As a result, we attained a randomly fluctuating intensity of light behind the aperture, which was used to excite the sample of interest. The best results were achieved when the aperture diameter was set to the same size as the mean size of speckles. A larger size of the aperture decreases the contrast of the temporal speckles; a smaller size reduces the excitation light intensity.

A small fraction of the excitation intensity was divided by a thin BK7 window and directed onto a biased Si photodiode (Thorlabs, 35 ns rise time) to acquire the excitation signal. The remaining part was used to excite a sample. Samples were excited by a fluctuating excitation intensity

Optics EXPRESS

with the typical mean value of 5 μW, hence the efficiency of the excitation light extraction is approximately 0.1%. The PL signal was detected with a Hamamatsu photomultiplier (PMT) module type H10721-20 (rise time 0.6 ns). The module was placed close to the sample so that no collecting lens needed to be used. A cut-off color filter (OG 515) was placed in front of the PMT to shield out the excitation wavelength. Both the excitation and the PL signals were amplified by an SRS amplifier model SR445A and read out by a TiePie Handyscope HS3 USB oscilloscope.

In order to compare the results of the RATS method with a commonly used technique, we measured the same test samples on the RATS setup and on a Hamamatsu StreakScope C10627-11 streak camera coupled with a spectrograph. In the streak-camera measurements, we excited the sample with 515 nm pulses featuring a low excitation energy of 15 nJ/pulse and 190 fs pulse length. The spectrally resolved PL dynamics were attained with the central detection wavelength of 650 nm.

The modulation frequency of a generated random excitation signal is proportional to the peripheral speed of the diffuser and increases when the mean grain size on the diffuser is reduced. The mean size of speckles is given by the size of the focused laser spot on the diffuser and we set accordingly the diameter of the iris aperture in order to crop the speckle pattern (see Fig. 2). It is possible to improve the modulation frequency of the random excitation signal by reducing both the speckle size and the iris aperture diameter. However, a significant improvement in the modulation frequency also leads to a vast reduction of the excitation intensity and this effect was not used in our experiments.

3. Results and discussion

3.1. Instrument response function

A crucial parameter of time-resolved spectroscopy is the attainable temporal resolution of a method. This is characterized by the impulse response function (IRF) of the method. The IRF can be determined as a reconstruction of scattered excitation light, or by measuring a sample, where PL decays very rapidly compared to the expected IRF width. We measured IRF by using PL from Rhodamine 6G solution, which has got PL lifetime in units of nanoseconds [14], and evaluated its full width half maximum (FWHM) for each experimental parameter. The IRF width is affected by several factors, which we discuss in the following paragraphs.

Analogously to standard methods, the presented method can be limited by the available bandwidth of the used photodetectors and amplifier. Since we used detection systems and electronics with a bandwidth exceeding 300 MHz, this fact did not limit the performance of the RATS setup.

As the method is based on the use of Fourier transform, it holds that the detection acquisition rate is the principal limitation of the shortest attainable lifetime and the total acquisition time is the principal limitation of the longest measurable lifetime. Nevertheless, the detected signal in the RATS experiment has to be sampled on a level where no aliasing occurs. Aliasing can cause severe distortion of the reconstructed PL decay. Therefore, it is essential to adjust the sampling rate according to the highest available frequency in the temporal speckle fluctuation or to use a low-pass frequency filter before the signal sampling.

Finally, it transpired that the main limiting factor in the RATS method case is the rate of temporal speckle fluctuation. The width of the IRF is inversely proportional to the maximum frequency present in the temporal speckle waveform. The frequency of speckles is directly proportional to the peripheral speed of the diffuser v. The frequency of speckles increases when the mean grain size is reduced and also when the beam spot size is reduced. This fact can be represented by function $h(g,d)$. Dependence of $h(g,d)$ will be described in our future work. For clarity, Eq. (3) can be written:

$$FWHM_{(IRF)} \propto \frac{h(g,d)}{v} \tag{3}$$

Optics EXPRESS

To test this fact, we evaluated the IRF for an increasing frequency of the rotating diffuser. The beam spot size was approximately 50 µm. The diffuser was 100 mm in diameter, featuring the mean grain size g of 1.52 µm. Since the frequency of the temporal speckles is proportional to the peripheral speed of the diffuser, the IRF becomes inversely proportional to the diffuser rotational frequency, as one can also observe in Fig. 3. For a diffuser frequency reaching 65 Hz, the FWHM of the IRF decreased to 870 ns. Hence, the presented setup allowed us to measure PL dynamics with the microsecond and sub-microsecond resolution. On the other hand, the longest measurable PL lifetime is only limited by the acquisition time.

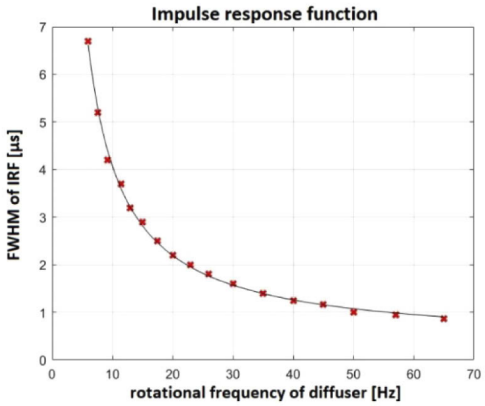

Fig. 3. Experimentally measured impulse response function width (FWHM) for different rotation frequencies of diffuser (red crosses) fitted with a reciprocal function (black line). Laser wavelength 488 nm, diffuser diameter 100 nm, grain size 1.52 µm.

3.2. Test measurements

To test the presented method, we used an orange color filter (SCHOTT, OG 565, glass matrix containing CdS_xSe_{1-x} nanoparticles), which absorbs all wavelengths below 550 nm and can be therefore excited with the used laser (488 nm). Another test sample was a layer of nanoporous silicon, which was prepared by electrochemical etching of Si wafer in hydrofluoric acid and ethanol solution. Details of the porous silicon preparation process and its optical properties can be found in previous publications, see [2,15].

Figure 4 summarizes the detected random signals (top panels), their Fourier representation (middle panels), and the determined PL decay for both samples (black crosses in bottom panels). The PL decay of the OG 565 filter was fitted with a sum of two exponentials convolved with a Gaussian IRF (FWHM 1.2 µs), which shows good agreement between measured IRF for corresponding rotation frequency (55 Hz) and fitted IRF when the PL decay was evaluated (see Fig. 4(A), left panel). The PL fitted decay of the OG 565 filter (red line) was $Ae^{t/\tau_1} + Be^{t/\tau_2}$, where A = 0.14, B = 0.006, $\tau_1 = 0.6$ µs (sub-IRF), $\tau_2 = 4.8$ µs.

Nanoporous silicon PL features a broad range of lifetimes, as it decays via the so-called stretched exponential function $A.\exp[-(t/\tau)^{\beta}]$ [16]. The measurement of this sample was done for the frequency of the diffuser of 23 Hz (IRF FWHM of 1.9 µs). The determined PL decay [see Fig. 4(B), right panel] was fitted with the stretched exponential function convolved with the Gaussian IRF (red line). The attained fitted parameters of the PL decay were $\tau = 0.7$ µs, $\beta = 0.35$.

The performance of the RATS method was verified by measuring the PL decay of the two test samples using a streak camera [17]. We picked the streak camera, as it is a commonly used device with a PL resolution very well below the RATS setup. The streak camera spectrograms were acquired on several timescales for each test sample. Figure 5(A) shows a selected spectrogram of

Optics EXPRESS

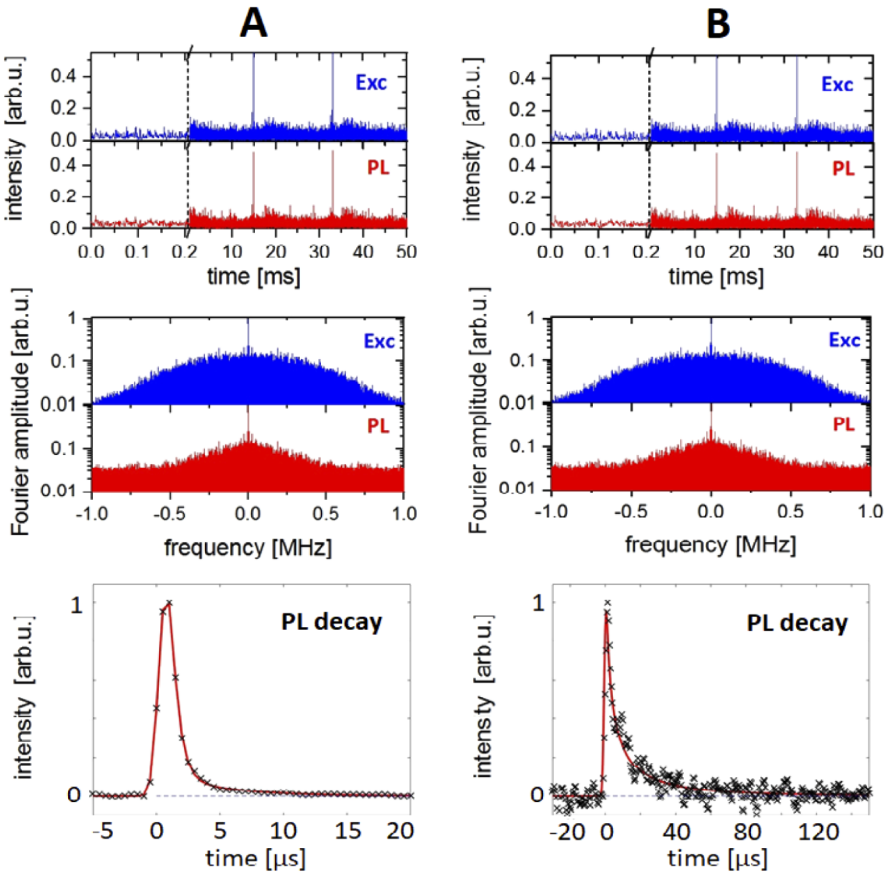

Fig. 4. Results of the RATS method for the orange filter OG565 (A) and nanoporous Si (B). Top panels: measured excitation and PL waveforms – note that the first 0.2 ms is zoomed in; middle panels: Fourier amplitudes of the signals – note the logarithmic y-axis; bottom panels: reconstructed PL kinetics (black crosses) fitted with PL decay convolved with Gaussian IRF (red lines). λexc = 488 nm. IRF width: OG565: 1.2 μs; nanoporous Si: 1.9 μs. Note that the sharp peaks in the temporal signals originate from a highly scattering spot on a diffuser.

Optics EXPRESS

the orange filter, in which the vertical axis represents the time axis, whereas the horizontal axis represents various wavelengths.

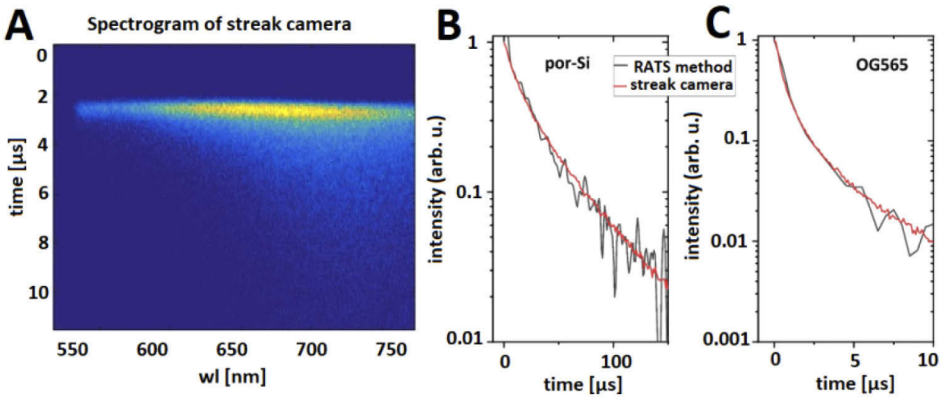

Fig. 5. Streak camera spectrogram of the orange filter sample (A). Excitation wavelength: 515 nm; energy 15 nJ/pulse; 190 fs pulse length. Comparison of PL decays of nanoporous silicon (B) and OG 565 filter (C) acquired by the RATS method (black curves) and integration of the streak camera data (red lines). For the sake of comparison, the data were normalized.

The attained PL decay curves are plotted in Figs. 5(B) and 5(C), where the red lines correspond to the streak camera curves, and the black lines were measured with the RATS method. The PL decays are in perfect agreement. The negligible difference could arise due to the fact that the PMT used in the RATS setup and the streak camera feature different spectral sensitivities. Since PL decay depends on PL wavelength (as can be clearly seen in Fig. 5), the total decay can vary for distinct sensitivities.

4. Method potential and limitations

The presented method has several advantages compared to its standard counterparts. Firstly, as we stressed previously, the excitation source can be any coherent light source without the necessity to be modulated controllably. Instability of the source is not an issue since it will only positively contribute to the random fluctuations.

Moreover, the method is very robust against signal offsets both in the temporal and detector background sense. A temporal offset between the PL and the excitation intensity will lead to a constant offset in the complex phase in the reconstructed decay, i.e., the resulting curve will be the actual decay curve multiplied by $e^{-i\varphi}$. This can be corrected easily. At the same time, the background offset of the signals will manifest only on the zero-frequency edge of the Fourier transform and can again be avoided by removing the low frequencies from the decay reconstruction. It is worth noting that all presented results were acquired without any timing or background correction.

In order to demonstrate the robustness of the method, we provide in Fig. 6 a reconstruction of the simulated data from Fig. 1, where we applied the mutual delay between the PL and the excitation signal (see panel A) and the offset of excitation and the PL signal (see panel B). Signals were delayed up to 7.2% compared to the total acquisition time without any observable significant effect on the reconstructed decay curve. Analogously, the signal offset reaching 400% of the original signal amplitude did not affect the reconstructed PL decay curve. For the sake of better comparison, the PL decay curves are presented vertically stacked in a semi-logarithmic scaling.

The method has specific advantages compared to both the time-domain and the frequency-domain methods. Although the phase-based measurement in the frequency domain is well

Optics EXPRESS

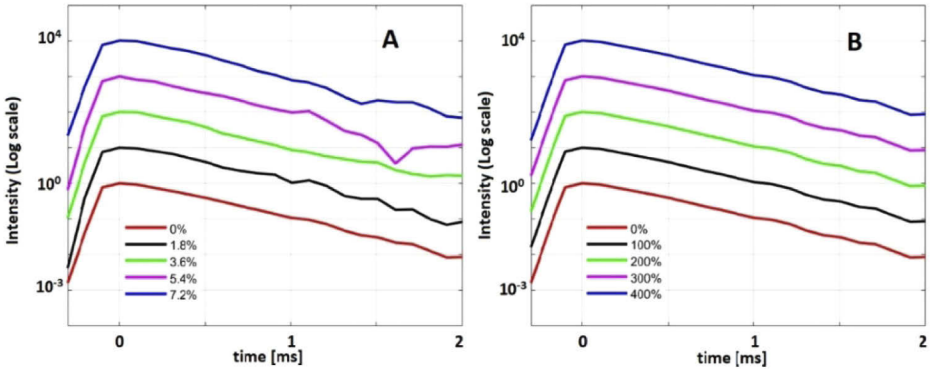

Fig. 6. Effect of temporal and background detection signal offset on the PL decay reconstruction. The simulated data from Fig. 1 were reconstructed for various delays between PL and excitation signal (panel A). The relative delay (0-7.2%) is given with respect to the total acquisition time. The same data were reconstructed for several offsets in the PL intensity signals (panel B). The relative offset (0-400%) is given with respect to the PL signal amplitude. Note that all curves are vertically stacked in a semilogarithmic scale in order to allow a better comparison.

developed on the sub-microsecond timescales, PL decay with a broad range of lifetimes – for instance, nanoporous silicon – requires scanning of the modulation frequencies. On the contrary, the RATS method, owing to the random sample excitation, extracts the PL decay from a single dataset. This is caused by the fact that the randomness of the signal covers a wide set of frequencies which is needed for proper reconstruction of PL decay.

The PL decay measurements in the time domain can be carried out efficiently at a low cost by using LED pulsed excitation sources [18]. However, the proposed method raises the term "low-cost" to a different level, as the excitation source can essentially be any laser module combined with a rotating diffuser (or any different means of random modulation).

The RATS method provides a very simple means of signal averaging. Experiments with pulsed excitation sources often rely on the measurements of many sequential excitations, where the detection has to be triggered with a corresponding precision. This part is entirely skipped in our setup, as the PL signal can be acquired for any period sufficient for the desired signal-to-noise ratio and the detection timing has no impact on the signal reconstruction.

At first sight, the proposed method uses inefficiently the excitation light, which is scattered by a diffuser. The ratio between the laser power and the mean excitation power in our experiments was 0.1%. Nevertheless, the sample is continuously excited by the source, whereas pulsed excitation uses a short flash of light from an LED. As a result, the LED provides a significantly lower number of excitation photons.

The presented method shares with the other methods for the measurement of PL decay in the temporal domain the need for a fast detection system and electronics. Nevertheless, such devices are widely available on the market, providing bandwidth of several hundreds of MHz. Therefore, the real limiting factor in our case lies in the properties of the diffuser, i.e., its peripheral speed and its grain size. The principal limitation of the method lies in the fact that the intensity of the PL emission must be linearly proportional to the excitation intensity. Under this condition, the measured PL waveform follows Eq. (1) and the convolution theorem can be used. Nevertheless, since the method relies on using a weak excitation intensity, this condition is satisfied for the majority of materials. Moreover, the method can be extended to be used for more general PL properties, namely, by changing the approach to PL decay reconstruction, where PL properties and lifetimes would be fitted to agree with the measured data.

Optics EXPRESS

The presented method can be simplified even more by pre-calibrating the I_{Exc} waveform. For a fixed position of the diffused beam and the diffuser center of rotation, the waveform will remain the same and does not need to be measured for each sample. Therefore, the entire optical setup can become even simpler by avoiding using a beam splitter and a reference photodiode.

5. Conclusions

We present a new approach to measuring PL decay, which can be used as a simple means of material characterization. The RATS (RAndom Temporal Speckles) method generates sample excitation by using a rotating diffuser without any need for a dedicated light source. With that approach, the method overcomes the need for advanced optical equipment and becomes a low-cost option for PL decay measurement.

By using this entirely different approach to the excitation signal, we can benefit from several advantages. Namely, no special requirements are put on the excitation source and its stability, and the method uses a low-cost setup enabling rapid data acquisition. Moreover, the random character of the excitation signal allows us to bring in advanced methods for computational reconstruction of PL decay, which will be addressed in our future work.

It should be mentioned that we optimized the diffuser and its peripheral speed so that the IRF width of 300 ns was achieved. Further reduction of the IRF width can be attained with a finer diffuser, a better-focused beam, or higher peripheral speed. However, the optimized diffuser was produced by using one of the finest abrasives (SiC 1000) and further increase in the peripheral speed is demanding with respect to the balancing of the diffuser disc. But e.g. using a proper microscope objective, it is still possible to reduce the size of the focused spot on the diffuser and thus reduce the width of IRF.

Nevertheless, the power of the idea of using a random signal for excitation of the measured sample can be, in principle, implemented by using any means of random modulation.

Funding

Akademie Věd České Republiky (ERC-CZ/AV-B, project RUSH); Grantová Agentura České Republiky (Project 17-26284Y); Ministerstvo Školství, Mládeže a Tělovýchovy (Reg. No. CZ.02.1.01/0.0/0.0/16_026/0008390); Grantová Agentura České Republiky (Project 19-14523S).

Acknowledgments

We gratefully acknowledge Jakub Junek and Jakub Nečásek for their help with improving the diffuser rotation speed.

Disclosures

The authors declare no conflicts of interest.

References

1. L. Foglia, S. Vempati, B. Tanda Bonkano, L. Gierster, M. Wolf, S. Sadofev, and J. Stähler, "Revealing the competing contributions of charge carriers, excitons, and defects to the non-equilibrium optical properties of ZnO," Struct. Dyn. **6**(3), 034501 (2019).
2. K. Žídek, F. Trojánek, P. Malý, L. Ondič, I. Pelant, K. Dohnalová, L. Šiller, R. Little, and B. R. Horrocks, "Femtosecond luminescence spectroscopy of core states in silicon nanocrystals," Opt. Express **18**(24), 25241–25249 (2010).
3. A. Lavie-Cambot, C. Lincheneau, M. Cantuel, Y. Leydet, and N. D. McClenaghan, "Reversible electronic energy transfer: a means to govern excited-state properties of supramolecular systems," Chem. Soc. Rev. **39**(2), 506–515 (2010).
4. K. Kůsová, O. Cibulka, K. Dohnalová, I. Pelant, J. Valenta, A. Fučíková, K. Žídek, J. Lang, J. Englich, P. Matějka, P. Štěpánek, and S. Bakardjieva, "Brightly Luminescent Organically Capped Silicon Nanocrystals Fabricated at Room Temperature and Atmospheric Pressure," ACS Nano **4**(8), 4495–4504 (2010).

Optics EXPRESS

5. R. M. Clegg and P. C. Schneider, "Fluorescence Lifetime-Resolved Imaging Microscopy: A General Description of Lifetime-Resolved Imaging Measurements," in *Fluorescence Microscopy and Fluorescent Probes*, J. Slavík, ed. (Springer, US, 1996), pp. 15–33.
6. A. Fojtik and A. Henglein, "Surface Chemistry of Luminescent Colloidal Silicon Nanoparticles," J. Phys. Chem. B **110**(5), 1994–1998 (2006).
7. K. Zheng, K. Žídek, M. Abdellah, M. E. Messing, M. J. Al-Marri, and T. Pullerits, "Trap States and Their Dynamics in Organometal Halide Perovskite Nanoparticles and Bulk Crystals," J. Phys. Chem. C **120**(5), 3077–3084 (2016).
8. P. I. H. Bastiaens and A. Squire, "Fluorescence lifetime imaging microscopy: spatial resolution of biochemical processes in the cell," Trends Cell Biol. **9**(2), 48–52 (1999).
9. M. J. Booth and T. Wilson, "Low-cost, frequency-domain, fluorescence lifetime confocal microscopy," J. Microsc. **214**(1), 36–42 (2004).
10. H. Szmacinski and J. R. Lakowicz, "Fluorescence lifetime-based sensing and imaging," Sens. Actuators, B **29**(1-3), 16–24 (1995).
11. H. Wang, Y. Qi, T. J. Mountziaris, and C. D. Salthouse, "A portable time-domain LED fluorimeter for nanosecond fluorescence lifetime measurements," Rev. Sci. Instrum. **85**(5), 055003 (2014).
12. F. Gascón and F. Salazar, "A simple method to simulate diffraction and speckle patterns with a PC," Optik **117**(2), 49–57 (2006).
13. A. N. Tikhonov and V. Y. Arsenin, "Solutions of ill-posed problems," (1977).
14. K. A. Selanger, J. Falnes, and T. Sikkeland, "Fluorescence lifetime studies of Rhodamine 6G in methanol," J. Phys. Chem. **81**(20), 1960–1963 (1977).
15. K. Dohnalová, L. Ondič, K. Kůsová, I. Pelant, J. L. Rehspringer, and R.-R. Mafouana, "White-emitting oxidized silicon nanocrystals: Discontinuity in spectral development with reducing size," J. Appl. Phys. **107**(5), 053102 (2010).
16. J. Linnros, N. Lalic, A. Gelackas, and V. Grivickas, "Analysis of the stretched exponential photoluminescence decay from nanometer-sized silicon crystals in SiO 2," J. Appl. Phys. **86**(11), 6128–6134 (1999).
17. I. Pelant and J. Valenta, *Luminescence Spectroscopy of Semiconductors* (Oxford University, 2012).
18. M. Sulkes and Z. Sulkes, "Measurement of luminescence decays: High performance at low cost," Am. J. Phys. **79**(11), 1104–1111 (2011).

Research Article | Vol. 29, No. 4 / 15 February 2021 / Optics Express 5538
Optics EXPRESS

Fluorescence lifetime imaging via spatio-temporal speckle patterns in a single-pixel camera configuration

J. JUNEK[1,2,*] AND K. ŽÍDEK[1]

[1]Regional Center for Special Optics and Optoelectronic Systems (TOPTEC), Institute of Plasma Physics, Czech Academy of Science v.v.i., Za Slovankou 1782/3, 182 00 Prague 8, Czech Republic
[2]Technical University in Liberec, Faculty of Mechatronics, Informatics and Interdisciplinary Studies, Studentská 1402/2, 461 17 Liberec, Czech Republic
*junekj@ipp.cas.cz

Abstract: Photoluminescence (PL) spectroscopy offers excellent methods for mapping the PL decay on the nanosecond time scale. However, capturing maps of emission dynamics on the microsecond timescale can be highly time-consuming. We present a new approach to fluorescence lifetime imaging (FLIM), which combines the concept of random temporal speckles excitation (RATS) with the concept of a single-pixel camera based on spatial speckles. The spatio-temporal speckle pattern makes it possible to map PL dynamics with unmatched simplicity. Moreover, the method can acquire all the data necessary to map PL decay on the microsecond timescale within minutes. We present proof-of-principle measurements for two samples and compare the reconstructed decays to the non-imaging measurements. Finally, we discuss the effect of the preprocessing routine and other factors on the reconstruction noise level. The presented method is suitable for lifetime imaging processes in several samples, including monitoring charge carrier dynamics in perovskites or monitoring solid-state luminophores with a long lifetime of PL.

1. Introduction

Fluorescence lifetime imaging (FLIM) is an essential spectroscopic method in various fields, including medicine, biology, and material science. Interest in FLIM and its broad applicability stimulate its development. Therefore, FLIM has many different implementations based on a variety of fundamental methods for measuring photoluminescence (PL) decay, which include gated photoluminescence counting [1], streak camera [2], time-domain analog recording technique [3], or frequency-domain analog recording technique [4]. However, the most commonly used method is time-correlated single-photon counting (TCSPC) [5,6].

TCSPC is a powerful method to trace PL decay with a lifetime in the order of nanoseconds. However, due to the principle of TCSPC operation, data acquisition can take several hours for samples with a PL lifetime on the microsecond timescale. Therefore, the reduction of the acquisition time in FLIM has become a topic discussed in the literature in its own right [7]. A possible way to reduce the acquisition time is to apply so-called compressed sensing, where the image can be reconstructed from a highly reduced dataset [8,9]. However, these works rely on TCSPC and, despite reducing the acquisition times, FLIM of the samples with a long-lived PL decay still represents an issue. It is also worth noting that standard FLIM methods usually require costly setups.

In this paper, we present an entirely new concept of FLIM. The concept is based on the use of speckle patterns, both in the spatial and temporal sense, to map the PL decay of a sample. We combine compressive imaging, namely the concept of a speckle-based single-pixel camera [10], with our recent work [11], where random temporal speckles (abbr. RATS) make it possible to trace PL dynamics. In the presented concept, we employ spatio-temporal speckles, which are

#413650 https://doi.org/10.1364/OE.413650
Journal © 2021 Received 29 Oct 2020; revised 15 Jan 2021; accepted 20 Jan 2021; published 5 Feb 2021

Optics EXPRESS

generated by using two diffusers. The speckles can be generated with any coherent excitation source, i.e., without the need for a pulsed laser. At the same time, the detector is a standard single-pixel detector, e.g., a photomultiplier. The setup is, therefore, very simple, robust, and low-cost. Owing to the novel approach to PL decay acquisition, the method is highly suitable for mapping PL dynamics on the microsecond timescale, where the FLIM dataset can be acquired within minutes. We demonstrate this on proof-of-principle measurements by imaging PL decay of selected scenes (colour filters and Si nanocrystal layers) and we also discuss the effect of speckle properties on the resulting noise level.

The presented method can serve as a simple approach to characterizing the morphology of samples with prominent PL decay in the order of microseconds, which include halide perovskite samples, solid-state luminophores, or Si nanocrystals [12–14].

2. Principle of the method

2.1. Concept of RATS method

The cornerstone of the presented FLIM concept is the RATS method, which is described in detail in our previous work [11]. This novel method for the measurement of PL decay uses randomly fluctuating intensity I_{EXC} to excite a sample. The PL signal I_{PL} is then given as a convolution of I_{EXC} and PL decay I_D:

$$I_{PL} = I_{EXC} * I_D. \tag{1}$$

Therefore, I_D can be extracted via the convolution theorem using the Fourier transform, where we apply the so-called Tikhonov regularization weighted with the factor ε [15]:

$$I_{decay} = Re\left\{\mathbb{F}^{-1}\left[\frac{\mathbb{F}(I_{PL})\,\mathbb{F}^*(I_{Exc})}{\mathbb{F}(I_{Exc})\mathbb{F}^*(I_{PL}) + \varepsilon\overline{\mathbb{F}(I_{Exc})\mathbb{F}^*(I_{Exc})}}\right]\right\}. \tag{2}$$

The random character of I_{EXC} allows us to measure a broad range of frequencies. Thus, a single measurement of I_{EXC} and I_{PL} provides information sufficient for the complete I_D reconstruction. Since the original method acquires PL decay for a single spot only, we will hereafter denote the method as 0D-RATS. The principle of the method is described in Fig. 1, based on simulated data. In order to get a randomly-fluctuating excitation signal, the demonstrated 0D-RATS method uses temporal speckles generated via a rotating diffuser. However, the presented approach can use any principle of random temporal signal generation, which means the RATS method can be understood in more general terms as the RAndom Temporal Signals method.

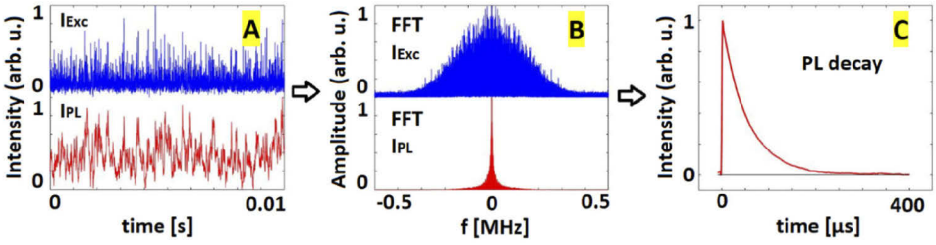

Fig. 1. Sequence showing the principle of I_D evaluation using the 0D-RATS method. A) Simulated temporally fluctuating intensity I_{EXC} (blue) and detected photoluminescence signal I_{PL} (red) arising due to a monoexponential decay (lifetime $\tau = 50$ µs). For clarity, a shorter time section is shown, than was used for reconstruction (0.1 s). B) Amplitudes of Fourier transform of I_{EXC} (blue) and I_{PL} (red). C) Reconstructed I_D via convolution theorem, Eq. (2).

Optics EXPRESS

New approaches to generating a temporally random light signal are likely to be found. This could mean an improvement both in terms of excitation intensity and higher frequency of the excitation signal.

2.2. Concept of proposed 2D-RATS method

An efficient approach to converting the 0D-RATS method to the imaging mode is to use the single-pixel camera. The principle of a single-pixel camera can be seen in many review articles [16]. In a single-pixel camera experiment, the measured sample is illuminated by a set of masks (see Fig. 2), which, in our experiment, were speckle patterns. Each illuminating random mask excites PL in different parts of the sample. After illuminating the sample with a sufficient number of masks, it is possible to retrieve the spatial information by detecting the overall level of the emitted PL and by using dedicated algorithms, as we will describe below. However, the condition that must always be met is the linear dependence between the measured and the reconstructed data.

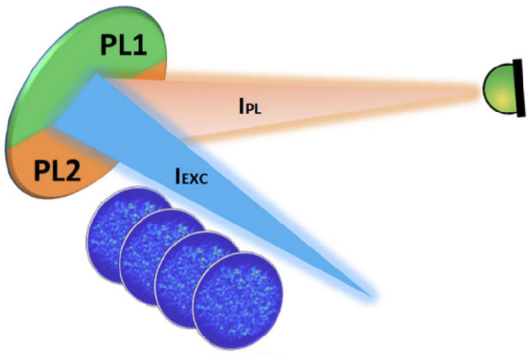

Fig. 2. Scheme of single-pixel camera image acquisition by using speckle patterns – see text for details.

In our FLIM approach, the illuminating masks are generated with a movable diffuser, which is placed behind the source of light with randomly fluctuating intensity in time, i.e., temporal speckles. Thus, we attain spatio-temporal speckles, which retain the same spatial pattern $S(x,y)$, while the overall intensity is blinking rapidly as $I_{EXC}(t)$. In other words, the measured sample is illuminated with a blinking pattern $P(x,y,t) = S(x,y)I_{EXC}(t)$. To map the PL decay I_D, i.e., to retrieve I_D (x,y,t), it is necessary to detect I_{EXC} (t) with a diode, I_{PL} (t) with a photomultiplier, and the speckle pattern $S(x,y)$ with an array 2D detector (e.g., CMOS camera).

Equation (1) can be rewritten for a 2D sample into a more general case, where n areas with different I_D are measured. The total emitted I_{PL} is the sum of the contributions from all sample spots:

$$\sum_{i=1}^{n} I_{PL(i)} = I_{EXC} * \sum_{i=1}^{n} I_{D(i)}. \tag{3}$$

For a given mask, we can evaluate from the measured data an average PL decay of the entire illuminated area I_{DA}:

$$I_{DA} = Re\left\{\mathbb{F}^{-1}\left[\frac{\mathbb{F}\left(\sum_{i=1}^{n} I_{PL(i)}\right)\ \mathbb{F}^{*}(I_{Exc})}{\mathbb{F}(I_{Exc})\mathbb{F}^{*}\left(\sum_{i=1}^{n} I_{PL(i)}\right) + \varepsilon\overline{\mathbb{F}(I_{Exc})\mathbb{F}^{*}(I_{Exc})}}\right]\right\}. \tag{4}$$

Optics EXPRESS

A different I_{DA} will be detected for each mask, as illustrated in Fig. 3(A). The variation of the I_{DA} value, i.e., PL decay, for a selected time and different masks will be denoted as d. See Fig. 3(B) for an example of a short subset of seven masks and four different times. We can vectorize each illumination mask into a single row of the so-called observing matrix A and we can also vectorize the map of the PL intensity into a vector m. In this case, we can express their relation as a simple matrix multiplication:

$$d = Am. \tag{5}$$

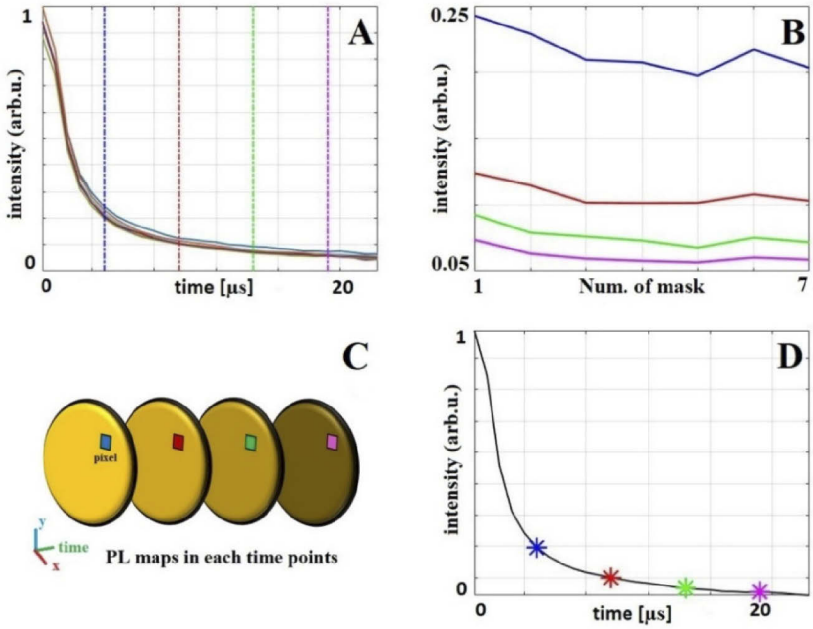

Fig. 3. (A) Examples of simulated I_D curves, which differ due to the change of the illuminating mask. (B) Varying intensity for the seven different masks in selected time-points of simulated I_D curves – see dashed lines in panel A. (C) Example of reconstructed PL maps. Selected pixels are marked with a colour corresponding to the time point. (D) A simulated example of reconstructed I_D in four time points. Reconstruction at multiple points would copy the entire I_D (solid black line).

Matrix A has a number of columns corresponding to the number of map pixels N, while the number of rows follows the number of used masks M, i.e., the number of measurements. The ratio between M and N determines the compression ratio $k = M/N$.

We aim at solving an underdetermined system, which can be accomplished by means of a compressed sensing algorithm where we employ a regularization. In this work, we used the algorithm TVAL3 [17,18], which is based on the minimization of total variation TV of reconstructed images and follows Eq. (6) [19].

$$\min\{||d - Am||_2^2 + TV(m)\}. \tag{6}$$

Using Eq. (6), it is possible to reconstruct the PL map $m(x,y)$ for each time point t [see Fig. 3(C)]. Knowing that we are reconstructing a PL image, we can constrain the solution to $m \in R$ and $m \geq 0$. If we stack the individual $m(x,y)$ behind each other, we create a 3D matrix $m(x,y,t)$

Optics EXPRESS

that corresponds to the appropriate PL intensity I_D (x,y,t) of the sample. Therefore, we can also extract PL decay for any selected spot of the sample [see Fig. 3(D)] and we can fit the obtained PL dynamics I_D with a single- or multi-exponential decay to get the lifetime map.

3. Optical setup

The used optical setup is depicted in Fig. 4. We used a CW laser at wavelength 405 nm (IO matchbox laser diode, free-space) as a light source. The combination of a focusing lens *A* (f = 25.4 mm), a rotating diffuser (average grain size 3.87 µm) with a collimating lens *B* (f = 75 mm), and an aperture (diameter 1.5 mm) generated intensity randomly fluctuating in time I_{EXC} (t).

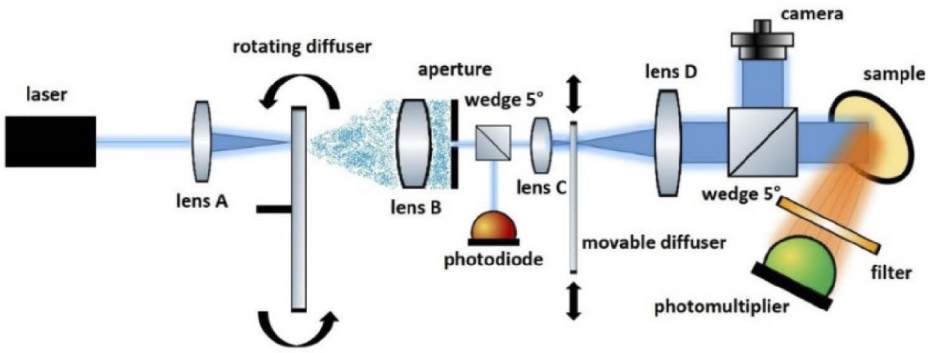

Fig. 4. Scheme of the used optical setup – see text for details.

The generation of a random mask (spatial speckles) is achieved with another focusing lens *C* (f = 25.4 mm). The beam is focused on a movable diffuser (average grain size 8.06 µm) and the diffused light is again collimated with lens D (f = 50 mm). The resulting mask pattern was blinking, according to I_{EXC} (t).

The patterned beam is split twice with two N-BK7 glass wedges (5°), which reflect about 6% of the incident intensity. The first reflection is used to detect I_{EXC}(t) with a Si amplified photodetector (Thorlabs PDA8A2, rise time 7 ns). The second reflected beam is used to acquire the mask pattern with a camera (CMOS, IDS UI-3240ML-M-GL). The transmitted pattern is used to illuminate the measured sample. The PL emitted from the excited sample, i.e., the $I_{PL}(t)$ signal, was detected with a type H10721-20 Hamamatsu photomultiplier (PMT) module (rise time 0.6 ns). The scattered excitation light was blocked by a cut-off filter at 500 nm (Thorlabs, FEL0500). The detected PL signal was amplified by a model SR445A SRS amplifier and read out by a TiePie Handyscope HS5-110XM USB oscilloscope.

The laser beam intensity entering the setup is 138.5 mW, while the full average intensity that illuminates the measured sample oscillates around 5.5 µW. The overall efficiency of the system is about 0.003%, which can be, however, improved approximately 10 times by optimizing the parameters of the optical elements. The size of the measured area was about 18 mm^2 and is given by the size of the generated speckle masks. It is possible to scale the field of view by adjusting the collimating lens D.

The TCSPC setup which was employed for the reference measurements used a picosecond laser at 405 nm, 100 kHz repetition rate, and 0.2 nJ/pulse. The laser pulses excited a PL signal detected by a PMT. The decay data were acquired by a PicoHarp 300 module. The impulse response function (IRF) of the TCSPC setup was negligible (< 1 ns) in comparison with the lifetimes of the measured samples, and, therefore, it has not been taken into account.

Optics EXPRESS

4. Results and discussion

As a proof-of-principle experiment, we carried out imaging of a combination of an OG565 orange absorbing cut off filter and a Si wafer with a nanoporous surface prepared by electrochemical etching of the Si wafer in hydrofluoric acid and ethanol solution [14,20]. Both samples had been measured previously by the 0D-RATS method and the resulting PL decay shapes had been verified with a standard method, namely the streak camera, and can be found in a previously published article [11].

In order to compare the data with methods commonly used for FLIM, we verified the 0D-RATS method with a reference TCSPC method. The comparison depicted in Fig. 5 confirms the correctness of the RATS approach. The 0D-RATS data (symbols) were measured in the same configuration and with the excitation light parameters described in Section 3. For the sake of this comparison, the detected spectral region in both setups (RATS and TCSPC) was restricted by colour filters to 500–800 nm. To compare the decays from the zero time, the TCSPC data were convoluted with the IRF of the 0D-RATS method, i.e., Gauss function with a full width half maximum (FWHM) equal to 0.59 µs. This convolution caused the depicted TCSPC curves (blue curves in Fig. 5) to be very smooth, in spite of the significant noise level in the raw data.

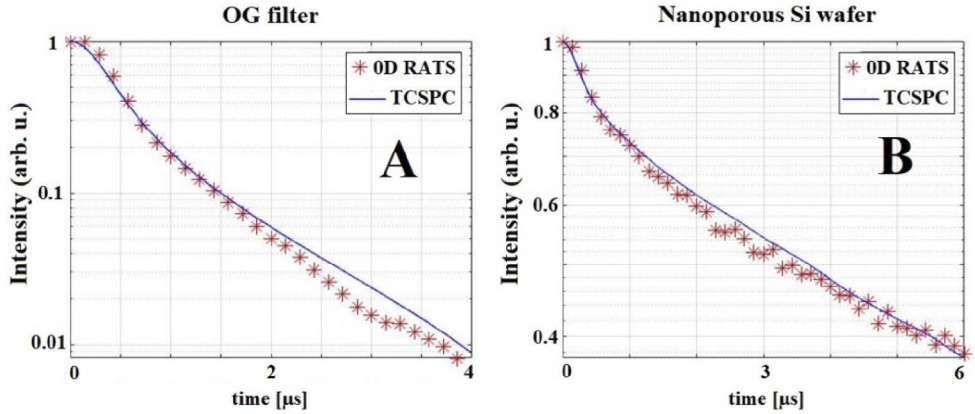

Fig. 5. 0D-RATS method verification with TCSPC method. Excitation wavelength: 405 nm; energy 19 µW/pulse, 100 kHz repetition rate. Comparison of PL decays of OG 565 filter (A) and nanoporous Si wafer (B) acquired by 0D-RATS method (blue lines) and TCSPC data convoluted with impulse response function of RATS measurement (red marks). See text for details. For the sake of comparison, the data have been normalized.

For the benefit of the comparison of the two methods, it is worth noting that, due to the long PL lifetimes, it was necessary to use a low excitation repetition rate (100 kHz) in the TCSPC setup. This led to the TCSPC acquisition time of 20 minutes (used for data in Fig. 5). In contrast, the 0D-RATS method acquired the PL decay data within 2 seconds. This value is proportionate to the acquisition time of the methods commonly used for microsecond PL measurement, such as direct PMT decay acquisition. Nevertheless, as we showed in the previous section, the RATS method allows a simple and low-cost implementation of FLIM based on the use of a single-pixel camera.

4.1. *Single-pixel camera PL map reconstruction*

Our method is based on compressive imaging and requires iterative image reconstruction, which was described in Eq. (6). The crucial parameters (together with their set value) were: *mu* (2^9),

Optics EXPRESS

beta (2^6). The reconstruction parameters were set according to the reconstruction of the testing experiments and simulations, and the same parameters are used for all the presented images.

4.2. Mask preprocessing

We captured the speckle mask on a CMOS chip and, prior to its use, we carried out a set of operations to convert the speckle image into a form suitable for our calculation.

The first part of preprocessing was cropping of the mask. Since the mask did not occupy the entire camera chip, the image was cropped so that the information value remains and at the same time we reduce the number of reconstructed pixels N.

The second part was the mask rescaling. A laser speckle pattern is a natural random pattern, where the dimensions of each speckle vary around a certain mean value. For this reason, it is unclear how the high-resolution camera image of laser speckles a_M should be rescaled into the image a_M' used in the measurement matrix A while retaining the useful information. An example of such rescaling is presented in Fig. 6.

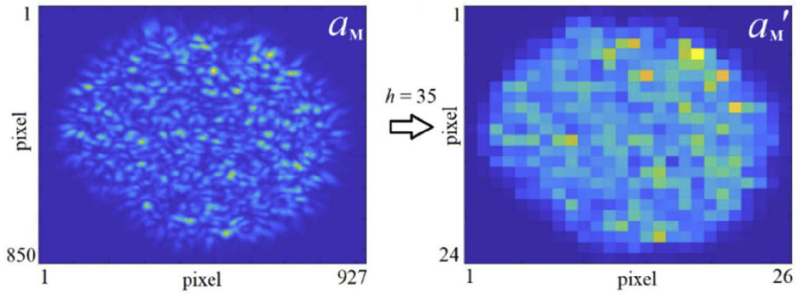

Fig. 6. Cropped original camera image of speckle patterns (a_M, left-hand side) compared to the processed mask pattern (a_M', right-hand side) with a scaling factor h = 35 pixels, which corresponds with the mean speckle size of the a_M pattern.

4.2.1. Mask rescaling effect

By using a set of simulations, we examined how the image reconstruction quality is affected by a varying mask scaling factor. The set of masks employed in the simulations, i.e., camera images of speckles, was acquired in the real measurements. The mean speckle size h for the examined set of masks is $h = 35$ pixels, which was calculated as the full width half maximum (FWHM) of the speckle pattern autocorrelation function [21]. The compression ratio k was set for the purpose of the simulations to 0.4, and the noise level of the PL intensity was set to the $\sigma = 0.5\%$.

The reconstruction error of the PL maps was calculated as an l_2 norm of the vectorized reconstructed image m and the original image U. To normalize the error for the image intensity, we calculate the relative error r:

$$r = \frac{||m - U||_2}{||U||_2}. \tag{7}$$

Since the scaling factor changes the number of pixels of a mask, the number of reconstructed image pixels N changed accordingly. The straightforward evaluation of the reconstruction quality by using residues was not meaningful because a smaller number of pixels leads to a lower level of residues despite worse image quality since we are solving a highly underdetermined system.

The simulations based on two different PL maps in Figs. 7(A)–7(B) show that the relative error r does not have a strong systematic dependence on the scaling factor [see Fig. 7(C)]. It is only possible to observe a slightly decreasing trend of the error towards smaller scaling values.

Optics EXPRESS

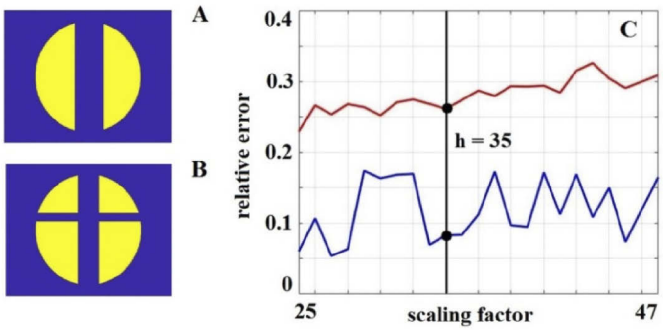

Fig. 7. Effect of scaling factor h on relative error in image reconstruction of two different PL maps depicted in panel A (red line in C) and panel B (blue line in C). The black line in panel C denotes the scaling factor according to the mean speckle size.

However, maintaining a given compression ratio for a higher resolution implies increasing the number of scanned masks, thus increasing the total acquisition time. Therefore, as a reasonable compromise, we used the scaling factor $h = 35$ that corresponded to the average speckle size of the used patterns. The effect of this scaling is illustrated in Fig. 6, which was processed based on this value.

4.3. *Proof-of-principle measurements*

The first analyzed sample was an OG565 orange absorbing cut-off filter, which was divided with an opaque line into two regions with the same PL decay dynamics I_D. Such a situation corresponds, for instance, to a mapping of a single PL marker in a sample. The illuminated spot was the size of $\sim$ 18 mm^2, the number of masks $M = 400$. The mask resolution was rescaled according to the speckle size ($h = 35$ pixels), leading to the image resolution of 28×36 ($N = 1008$).

We tested image reconstruction for three different compression ratios k, where the number of pixels N remained the same and the number of used masks M was decreased accordingly. Namely, we employed the compression ratio $k = 0.4$ [see Fig. 8(A)], $k = 0.2$ [see Fig. 8(B)], and $k = 0.05$ [see Fig. 8(C)]. The corresponding data acquisition times were 47 min, 24 min, and 6 min, respectively. The results are summarized in Fig. 8 and divided into areas A, B, and C, correspondingly.

The left part shows the reconstruction of the PL map for two different times. The middle part includes graphs "a" and "b", which show the I_D of a randomly selected pixel, which corresponds to the reconstructed area "a" or "b". The graphs include two time points (blue and violet), which correspond with time points of the PL maps from the left part of the figure. The reconstructed I_D data (lines) were compared to the 0D-RATS method (red circles). In all cases, the PL decays obtained by the 2D-RATS method are in perfect agreement with the data from the 0D-RATS method. Although the reconstructed PL maps for the compression ratio $k = 0.05$ are noisy compared to the higher compression ratios, the PL decays from 0D and 2D RATS methods are still in perfect agreement.

The FLIM spectrogram is shown on the right side of the image. Individual τ values were determined by the fitting algorithm. The reconstructed I_D curves for each pixel were fitted with a bi-exponential function. Lifetime τ was then determined as the time when the intensity of the fitted bi-exponential decay decreased to 10% of the curve maximum. The impulse response function of the measurement was 0.47 µs.

Optics EXPRESS

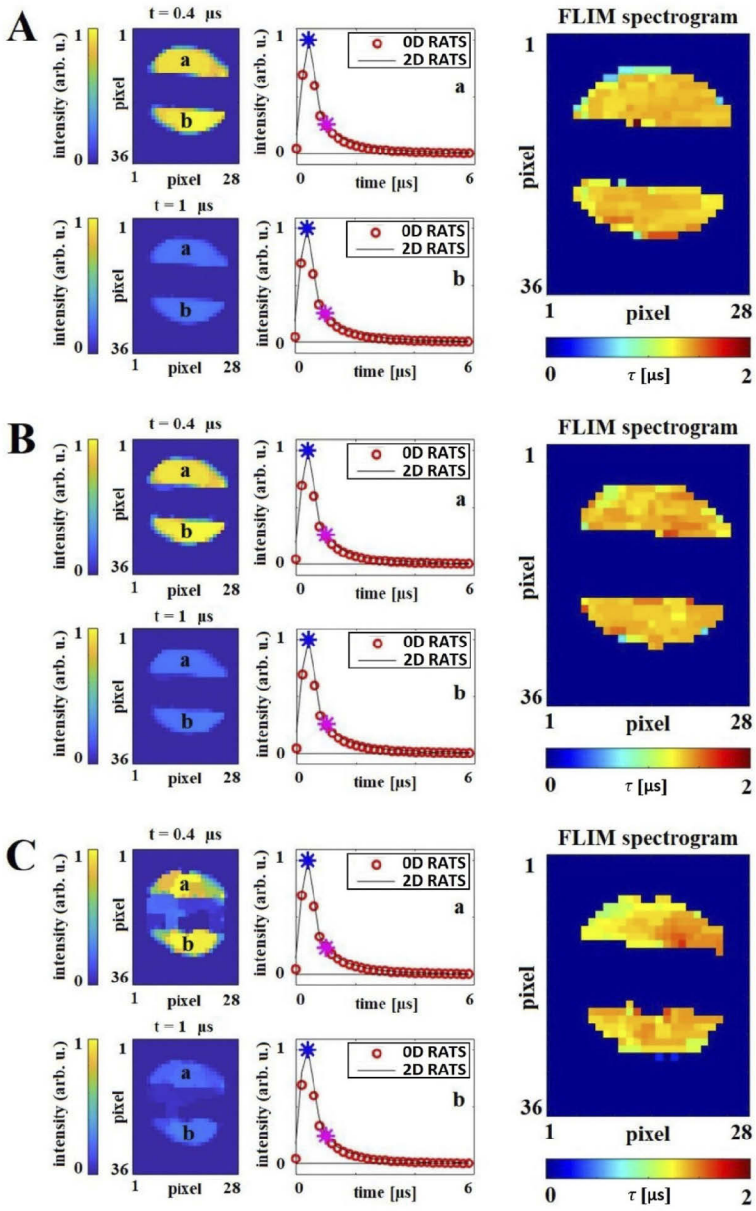

Fig. 8. Measurement of a masked OG565 filter: (A) compression ratio 0.4, (B) compression ratio 0.2, (C) compression ratio 0.05. Left panels: reconstruction of the PL map for two different times. Middle section: graphs "a" and "b" show the reconstructed I_D from 2D-RATS in a randomly selected pixel ("a" pix [14,10], "b" pix [16,25]) and I_D given via 0D-RATS; blue and violet stars denote the time of the PL maps on the left. Right section: map of the PL lifetimes for the points where the PL amplitude exceeded 10% of the maximum PL intensity.

Optics EXPRESS

The mean lifetimes for the sample measured with compression ratios 0.4, 0.2, and 0.05 are 1.31 µs, 1.29 µs, and 1.29 µs. The mentioned average lifetimes vary with standard deviations of 0.09 µs, 0.10 µs, and 0.13 µs. The statistical data do not include points that did not show a luminescence intensity lower than 10% of the sample maximum, as well as data from the sample edge, which were suffering from scattering signal and high noise level.

We observed that the lifetime precision, i.e., acquired standard deviations, are only marginally affected by the used compression ratio. This ratio has more effect on the quality of the lifetime maps.

In the second measurement, we acquired FLIM data of an artificially prepared sample with two different dynamics of PL decays I_D. The first area was an OG565 colour filter, while the second area consisted of a Si wafer with a nanoporous surface.

Both the OG565 filter and the nanoporous Si had been previously tested with a standard method and the 0D-RATS method, and the results from both 0D-RATS methods (Fig. 9, red crosses) were compared in randomly chosen pixels of the 2D PL map (see Fig. 9, solid lines). The results are summarized in Fig. 9 which follows the same logic as Fig. 8 but the compression ratios are different.

The measured area was around 18 mm^2; in total, 600 masks were scanned. Mask resolution was rescaled again according to the mean speckle size (35 pixels), leading to a resolution of the reconstructed PL map of 26×24 ($N = 624$). Due to the lower I_{PL} amplitude of nanoporous Si, the reconstructed data suffer from a lower signal-to-noise ratio. For this reason, we present reconstructed data for compression ratios $k = 0.9$ [Fig. 7(B)], and $k = 0.5$ [Fig. 7(C)]. The corresponding data acquisition times were 63 min, 49 min, and 35 min, respectively. The PL maps in Fig. 9 (left-hand side) have been normalized so that each data point has the same amplitude. Therefore, we observe a flat PL image at the early times (0.6 µs), while for the later time (1.6 µs), the prominent PL intensity is emitted from the upper part, i.e., nanoporous Si with a long PL decay.

Analogously to the previous measurement, individual τ values were determined again by fitting the data with double-exponential decay for both areas (OG565 and nanoporous Si). Lifetime τ corresponds, analogously to the previous measurement, to the time where the intensity of fitted I_D drops to 10% of the curve maximum. The impulse response function of measurement was 0.47 µs. For the nanoporous Si wafer, the mean lifetimes for the compression ratios of 0.9, 0.7, and 0.5 correspond to 21 µs, 21 µs, and 20 µs with a standard deviation of 3 µs, 3 µs, and 4 µs, respectively. For the OG565 filter, the mean lifetimes were 1.19 µs, 1.24 µs, and 1.28 µs, varying with a standard deviation of 0.09 µs, 0.16 µs, and 0.27 µs. The statistics included again only points that did not have a luminescence intensity greater than 10% of the sample maximum, as well as the edge points of the sample with the prevailing scattering signal. In the combined sample, we attained for all measurements a slightly lower lifetime of the OG565 filter area compared to the first sample. This arises due to the highly scattering Si wafer, which leads to a stronger leakage of the excitation signal compared to the first measurement. Subsequently, a larger amount of scattered excitation light reaches the detector and influences the results because it forms a response-function-limited peak, which it is not possible to completely separate from the PL decay.

4.4. Reconstruction error vs. intensity of PL decay

The intensity of PL is crucial for the resulting data reconstruction. This can be documented by the fact that the attained PL decay of the nanoporous Si suffers from a significantly higher noise level compared to the OG565 filter data. Analogously, we observed that the noise level of the PL decay increases with the delay after excitation, as the PL intensity decays and decreases. This effect was studied by using a relative error of reconstruction on the real dataset to capture the realistic behaviour of the experimental system, including the noise characteristics of the detectors.

Optics EXPRESS

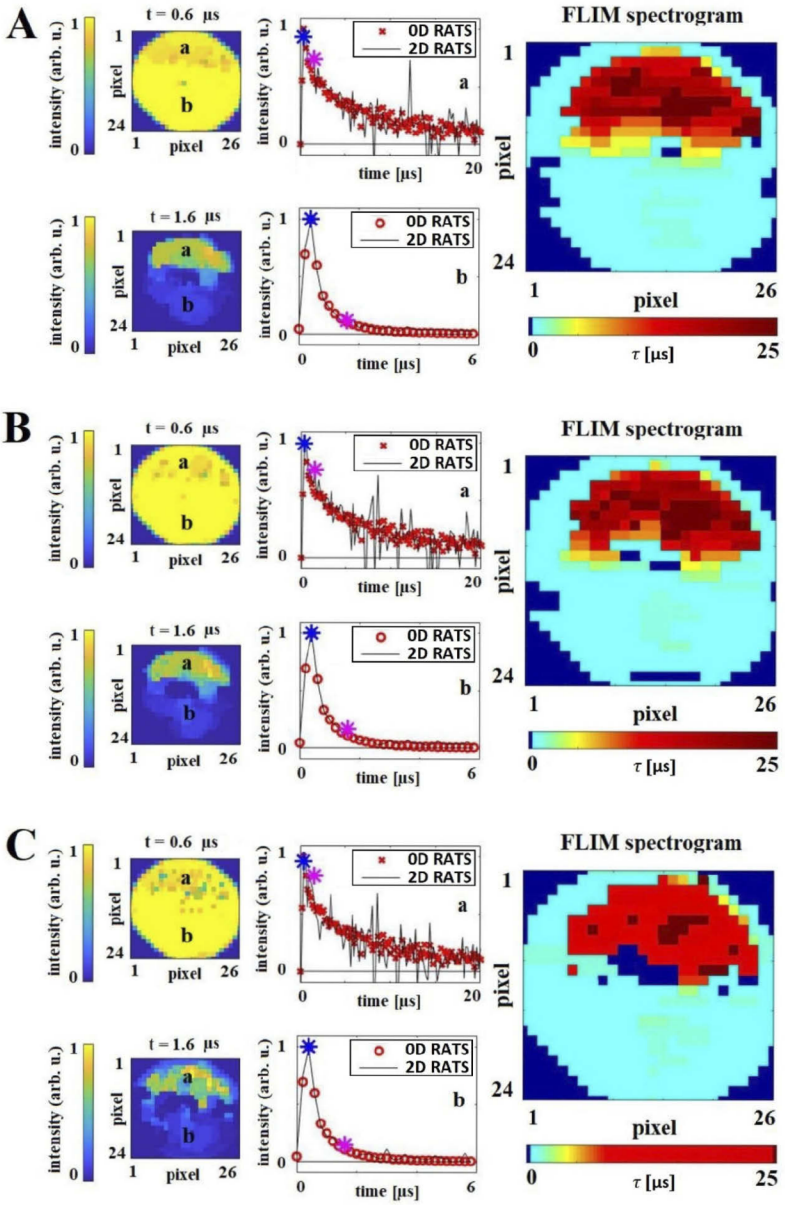

Fig. 9. Measurement of nanoporous Si wafer. (A) compression ratio 0.9, (B) compression ratio 0.7, (C) compression ratio 0.5. Left panels: reconstruction of the PL map for two different times. Middle part: graphs "a" and "b" show the reconstructed I_D from 2D-RATS in a randomly selected pixel ("a" pix [14,10], "b" pix [16,25]) and I_D given via 0D-RATS; blue and violet stars denote the time of the PL maps on the left. Right part: map of the PL lifetimes for the points where the PL amplitude exceeded 10% of the maximum PL intensity.

Optics EXPRESS

The relative error σ was determined as the average absolute deviation of the back reconstructed intensity signal d^R=Am [see Eq. (6)] and the original signal d at a given time point relative to the average value d:

$$\sigma = \frac{1}{M}\sum_{i=1}^{M}\frac{|d_i^R - d_i|}{d_i}. \tag{8}$$

Figure 10(A) (top panel) shows representative reconstructed decays for the first measurement (two areas with the same PL decay (OG565)). The PL decay of the upper part of the measured sample is indicated by a red line and the lower part with a blue line. In the bottom panel of Fig. 10(A), the relative error of reconstruction is evaluated. The same logic is also applied in Fig. 10(B), which shows representative decays for the combined sample (nanoporous Si + OG565 filter). The red line shows the PL decay of the upper part of the sample (nanoporous Si) and the blue line shows the PL decay of the lower part of the sample (filter OG565). The bottom panel of Fig. 10(B) then shows the relative reconstruction error. The relative error comparison according to Eq. (8) depicted in Fig. 10 (bottom panels) was done for the same compression ratio $k = 0.6$ and identical image resolution 26×24. This ensures that the length of the vector d remains constant. For cases where the length of the vector d changes, it is more appropriate to observe the reconstruction error with Eq. (7) because a lower number of elements of d can cause the reconstruction algorithm TVAL3 to reach a better agreement between d and d_0 while the reconstruction of the PL map can feature a lower quality.

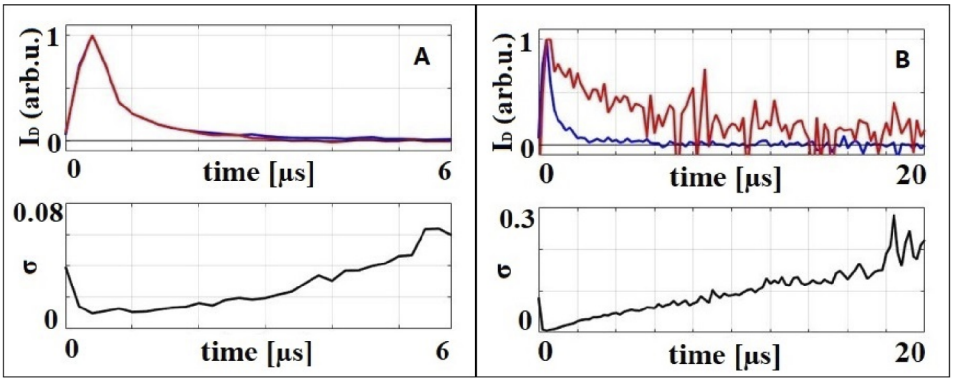

Fig. 10. Relative reconstruction error evaluation with respect to the level of I_D intensity. Upper panels: Two examples of PL decay curves (red and blue lines) extracted from the sample with two identical areas (filter OG565, panel A) and from the sample with two different areas (nanoporous Si + filter OG565, panel B). Bottom panels: reconstruction error σ is evaluated as a relative error via Eq. (8) in each reconstructed time point.

For both cases in Fig. 10, we observe that the relative error level steadily increases with the decreasing PL intensity (see the bottom panels). Thus, we can conclude that for a higher intensity of detected PL it would be possible to reconstruct decays with a lower relative error even for small compression ratios. However, the relative error still increases with the decreasing intensity of PL decay.

5. Conclusion

We present a new approach to FLIM, which is based on a combination of the random temporal speckles (RATS) method with the concept of a single-pixel camera. Spatio-temporal random speckle patterns make it possible to track both PL images and dynamics on the microsecond timescale. The speckle generation is based on rotating and movable diffusers, which reduces

Optics EXPRESS

system requirements. The result is a low-cost FLIM setup of unrivalled simplicity. The strength of the new concept lies in the imaging of PL decay on the microsecond timescale because the lifetime acquisition time is reduced owing to the use of compressed sensing. At the same time, the method can be performed using a simple single-pixel detector.

When compared to other commonly-used options of FLIM, the sample point-by-point scanning of PL decay rapidly reaches extremely high acquisition times as the resolution of an image increases. For instance, a 60×60 pixel image measured at 2 s per decay requires a total acquisition time of two hours. The use of intensified CCD or TCSPC with a 2D array of single-photon avalanche diodes (SPAD) can provide fast FLIM even in the microsecond timescale. Nevertheless, the use of such an array detector dramatically increases the cost of the setup.

The acquisition time of 2D-RATS depends on several factors. The most prominent one is the PL map resolution and the related compression ratio. We have shown that it is reasonable to use scaling according to the mean speckle size. A lower resolution causes a loss in the image quality, while a higher resolution cannot provide more information, as the resolution is limited by the mean speckle size. The FLIM data reconstruction error also highly depends on the intensity of PL. Hence, we can achieve fast acquisition by using a higher PL intensity while decreasing the compression ratio. Under ideal conditions, i.e., highly emitting samples, we were able to reach an acquisition time of 6 minutes. For a standard sample, it was necessary to increase the compression ratio and the resulting acquisition time reached 35 minutes.

We would like to stress that the 2D-RATS method is a general concept, which uses spatio-temporal random patterns to carry out time-resolved imaging. It can be therefore generalized for the imaging of any temporal signal and has many possible ways of implementation. Since this article serves as a demonstration of the new method, further optimization of the optical setup can provide us with more efficient excitation use and PL collection. For instance, the use of a pair of diffusers causes the vast majority of the excitation light energy to be lost in the setup and the resulting low excitation intensity can be limiting. Nevertheless, this can be solved by modifying the approach to mask generation – for instance, by using a digital micro-mirror device (DMD) or a multimode fibre. An increase in the excitation intensity and the signal to noise ratio (SNR) allows a further reduction of the compression ratio, thus decreasing the number of measurements and saving additional data acquisition time.

In summary, the method is a low-cost and straightforward alternative to commonly-used methods, providing the possibility of speedy measurement of fast mapping of PL decays on the microsecond timescale.

Funding. Akademie Věd České Republiky (ERC-CZ/AV-B (RUSH, Reg. No. ERC100431901)); Ministerstvo Školství, Mládeže a Tělovýchovy (Reg. No. CZ.02.1.01/0.0/0.0/16_026/0008390); Technická Univerzita v Liberci (SGS-2020-3057); Grantová Agentura České Republiky (17-26284Y).

Acknowledgment. We gratefully acknowledge Lukáš Ondič (Institute of Physics, Czech Academy of Sciences) for providing us with samples of nanoporous Si.

Disclosures. The authors declare no conflicts of interest.

References

1. J. Sytsma, J. M. Vroom, D. Grauw, and H. C. Gerritsen, "Time-gated fluorescence lifetime imaging and microvolume spectroscopy using two-photon excitation," J. Microsc. **191**(1), 39–51 (2008).
2. R. V. Krishnan, H. Saitoh, H. Terada, V. E. Centonze, and B. Herman, "Development of a multiphoton fluorescence lifetime imaging microscopy system using a streak camera," Rev. Sci. Instrum. **74**(5), 2714–2721 (2003).
3. S. Cheng, R. M. Cuenca, B. Liu, B. H. Malik, J. M. Jabbour, K. C. Maitland, J. Wright, Y.-S. L. Cheng, and J. A. Jo, "Handheld multispectral fluorescence lifetime imaging system for in vivo applications," Biomed. Opt. Express **5**(3), 921–931 (2014).
4. A. D. Elder, C. F. Kaminski, and J. H. Frank, "ϕ^2FLIM: a technique for alias-free frequency domain fluorescence lifetime imaging," Opt. Express **17**(25), 23181–23203 (2009).
5. W. Becker, A. Bergmann, G. Biscotti, K. Koenig, I. Riemann, L. Kelbauskas, and C. Biskup, "High-speed FLIM data acquisition by time-correlated single-photon counting," Proc. SPIE **5323**, 27–35 (2004).

Optics EXPRESS

6. N. Krstajić, S. Poland, J. Levitt, R. Walker, A. Erdogan, S. Ameer-Beg, and R. K. Henderson, "0.5 billion events per second time correlated single photon counting using CMOS SPAD arrays," Opt. Lett. **40**(18), 4305–4308 (2015).
7. X. Liu, D. Lin, W. Becker, J. Niu, B. Yu, L. Liu, and J. Qu, "Fast fluorescence lifetime imaging techniques: A review on challenge and development," J. Innovative Opt. Health Sci. **12**(05), 1930003 (2019).
8. V. Studer, J. Bobin, M. Chahid, H. S. Mousavi, E. Candes, and M. Dahan, "Compressive fluorescence microscopy for biological and hyperspectral imaging," Proc. Natl. Acad. Sci. U. S. A. **109**(26), E1679–E1687 (2012).
9. Q. Pian, R. Yao, N. Sinsuebphon, and X. Intes, "Compressive hyperspectral time-resolved wide-field fluorescence lifetime imaging," Nat. Photonics **11**(7), 411–414 (2017).
10. K. Žídek, O. Denk, and J. Hlubuček, "Lensless Photoluminescence Hyperspectral Camera Employing Random Speckle Patterns," Sci. Rep. **7**(1), 15309 (2017).
11. J. Junek, L. Ondič, and K. Žídek, "Random temporal laser speckles for the robust measurement of sub-microsecond photoluminescence decay," Opt. Express **28**(8), 12363–12372 (2020).
12. K. Zheng, K. Žídek, M. Abdellah, M. E. Messing, M. J. Al-Marri, and T. Pullerits, "Trap States and Their Dynamics in Organometal Halide Perovskite Nanoparticles and Bulk Crystals," J. Phys. Chem. C **120**(5), 3077–3084 (2016).
13. J. M. Griffin, A. J. Miller, A. J. Berry, S. Wimperis, and S. E. Ashbrook, "Dynamics on the microsecond timescale in hydrous silicates studied by solid-state 2H NMR spectroscopy," Phys. Chem. Chem. Phys. **12**(12), 2989–2998 (2010).
14. K. Dohnalová, L. Ondič, K. Kůsová, I. Pelant, J. L. Rehspringer, and R.-R. Mafouana, "White-emitting oxidized silicon nanocrystals: Discontinuity in spectral development with reducing size," J. Appl. Phys. **107**(5), 053102 (2010).
15. A. N. Tikhonov and V. Y. Arsenin, "Solutions of ill-posed problems," SIAM Rev. **21**, 266–267 (1977).
16. M. F. Duarte, M. A. Davenport, D. Takhar, J. N. Laska, T. Sun, K. F. Kelly, and R. G. Baraniuk, "Single-pixel imaging via compressive sampling," IEEE Signal Process. Mag. **25**(2), 83–91 (2008).
17. C. Li, Wotao Yin, and Yin Zhang, TVAL3 Home, Rice University, 2009, Last updated 11/07/2013, (available from: https://www.caam.rice.edu/~optimization/L1/TVAL3/).
18. C. Li, W. Yin, and Y. Zhang, "User's guide for TVAL3: TV minimization by augmented lagrangian and alternating direction algorithms," CAAM Rep. 20, 46–47 (2009).
19. C. Li, "An Efficient Algorithm For Total Variation Regularization with Applications to the Single Pixel Camera and Compressive Sensing," Master Thesis, Rice University (2009).
20. K. Žídek, F. Trojánek, P. Malý, L. Ondič, I. Pelant, K. Dohnalová, L. Šiller, R. Little, and B. R. Horrocks, "Femtosecond luminescence spectroscopy of core states in silicon nanocrystals," Opt. Express **18**(24), 25241–25249 (2010).
21. I. Hamarová, P. Šmíd, P. Horváth, and M. Hrabovský, "Methods for Determination of Mean Speckle Size in Simulated Speckle Pattern," Meas. Sci. Rev. **14**(3), 177–182 (2014).

Research Article | Vol. 30, No. 8 / 11 Apr 2022 / Optics Express 12654
Optics EXPRESS

Noise effect on 2D photoluminescence decay analysis using the RATS method in a single-pixel camera configuration

JIŘÍ JUNEK[1,2,*] AND KAREL ŽÍDEK[1]

[1]Regional Center for Special Optics and Optoelectronic Systems TOPTEC, Institute of Plasma Physics of the Czech Academy of Sciences v.v.i., Za Slovankou 1782/3, 182 00 Prague 8, Czech Republic
[2]Technical University in Liberec, Faculty of Mechatronics, Informatics and Interdisciplinary Studies, Studentská 1402/2, 461 17 Liberec, Czech Republic
*junekj@ipp.cas.cz

Abstract: Using a random temporal signal for sample excitation (RATS method) is a new, capable approach to measuring photoluminescence (PL) dynamics. The method can be used in single-point measurement (0D), but also it can be converted to PL decay imaging (2D) using a single-pixel camera configuration. In both cases, the reconstruction of the PL decay and PL snapshot is affected by ubiquitous noise**.** This article provides a detailed analysis of the noise effect on the RATS method and possible strategies for its suppression. We carried out an extensive set of simulations focusing on the effect of noise introduced through the random excitation signal and the corresponding PL waveform. We show that the PL signal noise level is critical for the method. Furthermore, we analyze the role of acquisition time, where we demonstrate the need for a non-periodic excitation signal. We show that it is beneficial to increase the acquisition time and that increasing the number of measurements in the single-pixel camera configuration has a minimal effect above a certain threshold. Finally, we study the effect of a regularization parameter used in the deconvolution step, and we observe that there is an optimum value set by the noise present in the PL dataset. Our results provide a guideline for optimization of the RATS measurement, but we also study effects generally occurring in PL decay measurements methods relying on the deconvolution step.

1. Introduction

Fluorescence lifetime imaging (FLIM) is a frequent spectrometric analysis in biology [1,2], chemistry [3], and materials engineering [4]. There are various techniques for measuring or evaluating photoluminescence (PL) dynamics, such as time-correlated single photon counting [5], gated PL counting [6], streak camera [7], time-domain or frequency-domain analog recording technique [8,9]. Another available method for PL decay measurement is based on random excitation of the measured sample - the RATS method (RAndom Temporal Signals) [10], which could also be set in a single-pixel camera (SPC) configuration [11] and carry out the FLIM experiment. We abbreviate this measurement as 2D-RATS. At the current state, the method can characterize morphology in the order of microseconds or sub-micro seconds (hundreds of nanoseconds), including halide perovskite samples, solid-phase luminophores, or Si nanocrystals [12–14]. However, ongoing research shows that it will be realistic to measure even at the nanosecond scale.

The 2D-RATS method combines the SPC technique with the excitation of the PL with random patterns (masks) blinking randomly in time. Each mask leads to a specific PL decay, which is measured for a set of uncorrelated masks. Then, using algorithms for undetermined systems, it is possible to reconstruct PL decays in each individual pixel of the 2D scene. The quality of reconstruction is affected by noise, which is inevitably present in all measured data. Therefore,

#450613 https://doi.org/10.1364/OE.450613
Journal © 2022 Received 5 Dec 2021; revised 9 Mar 2022; accepted 17 Mar 2022; published 31 Mar 2022

Optics EXPRESS

the noise analysis of the method is an essential piece of knowledge that allows optimization of the method and identifies the most sensitive aspects of the setup. Moreover, many results valid for the RATS method are also relevant for the PL measurement, where the deconvolution step is used [15].

In this article, we carry out a detailed study of various noise effects on the 2D-RATS measurement and their impact on the resulting FLIM information. Our analysis is based on extensive simulations and a set of synthetic data faithfully following the real experimental conditions for the SPC experiment carried with a digital micro-mirror device (binary illumination mask). A digital micro-mirror device is part of our latest 2D-RATS setup, where it replaced an optical diffuser (greyscale mask) [11]. Nevertheless, both binary and greyscale masks lead to the same trends with respect to the noise level, and the presented results are generally valid for both random mask implementations.

We analyze the benefits of various approaches to noise reduction. Besides the generally used option to prolong the acquisition time [16], the deconvolution step in the RATS method allows us to optimize the regularization parameter of the deconvolution [17,18]. Due to the random nature of the excitation signal in RATS, we avoid the use of any mathematical filters which can be apparently optimized for one type of signal, but due to the possibility of choosing a different signal frequency and sampling, such a filter can be difficult to transfer to a general case.

Our article provides guidelines for optimizing experiments for PL decay measurement and FLIM, where the deconvolution-based retrieval of PL dynamics is used. We demonstrate that the noise present in the PL dataset is the most critical factor. At the same time, we show that the resulting noise level in the FLIM dataset can be highly decreased by using a longer non-periodic excitation signal or by optimizing the regularization parameter. The parameter features an optimum value for a given noise level. We point out the issues connected to a periodic excitation signal.

In particular, we demonstrate that with proper choice of regularization parameter and acquisition time, the RATS method can attain results that are not distorted at all and can accurately map a 2D scene even with a relatively high noise level (3%).

2. RATS method

We will first introduce the principles of the single-spot 0D-RATS method and imaging 2D-RATS measurement. The cornerstone of the RATS method is sample excitation with a random signal I_{EXC}. The random signal I_{EXC} could be generated using a generator (lens, rotating diffuser, aperture) described in our previous work [10]. However, there are many different ways to generate a random signal. In the experiment should be detected I_{EXC} (photodiode) and PL signal I_{PL} (photomultiplier), which is given as convolution of I_{EXC} and PL decay I_D (Eq. (1)).

$$I_{PL} = I_{EXC} * I_D. \tag{1}$$

This fact can be used to recover the PL decay from I_{PL} by using the Fourier transform and the convolution theorem. The deconvolution is attainable only for the frequencies where the excitation signal has a non-zero amplitude. Nevertheless, due to random excitation, a single measurement contains a broad range of frequencies in a single dataset. PL decay I_D could then be determined via deconvolution (Eq. (2)), wherein the denominator is regularization parameter ε adding a part of the average power of the spectrum due to it is possible to solve ill-conditioned problems.

$$I_D = Re\left\{\mathbb{F}^{-1}\left[\frac{\mathbb{F}(I_{PL})\,\mathbb{F}^*(I_{EXC})}{\mathbb{F}(I_{EXC})\mathbb{F}^*(I_{EXC}) + \varepsilon\overline{\mathbb{F}(I_{EXC})\mathbb{F}^*(I_{EXC})}}\right]\right\}. \tag{2}$$

The 2D-RATS measurement is carried out in an SPC configuration, as we described in our previous article [11]. We point the reader to numerous articles summarizing the SPC

Optics EXPRESS

experiment for more details [19–22]. In our implementation of the SPC experiment, the sample was illuminated with a set of random excitation patterns (masks). The excitation masks were "blinking" with the same waveform $I_{EXC}(t)$, and the whole PL from each illuminated point i is collected to a single-pixel detector. The time t for which a single mask illuminates the sample following the intensity fluctuation of $I_{EXC}(t)$ is stated as acquisition time and is marked as t_{acq}. For the 0D-RATS, the acquisition time is equal to the total duration of the experiment. For the 2D-RATS experiment, the measurement over the acquisition time is repeated for each random mask.

The photoluminescence I_{PL} is given as a summation of $I_{PL}(i)$ signals. Then Eq. (1) can be rewritten for the total PL intensity as:

$$I_{PL} = \sum_{i=1}^{n} I_{PL}(i) = I_{EXC} * \sum_{i=1}^{n} I_D(i). \tag{3}$$

The number of excitation masks M is set by the number of image pixels N and the so-called compression ratio $k = M/N$. Because masks are not coherent, i.e., one pattern is not correlated with each other, each mask illuminates a different combination of the sample pixels, and, therefore, each mask represents its own I_{PL}, which can be used to retrieve the PL decay I_{DA}:

$$I_{DA} = Re\left\{\mathbb{F}^{-1}\left[\frac{\mathbb{F}\left(\sum_{i=1}^{n} I_{PL(i)}\right)\,\mathbb{F}^{*}(I_{Exc})}{\mathbb{F}(I_{Exc})\mathbb{F}^{*}(I_{Exc}) + \varepsilon\overline{\mathbb{F}(I_{Exc})\mathbb{F}^{*}(I_{Exc})}}\right]\right\}. \tag{4}$$

PL snapshot $m(t)$ can be reconstructed in each delay after excitation t using the calculated $I_{DA}(t)$ curves. For the given delay and each excitation mask, the $I_{DA}(t)$ provides a dataset I_{SPC} describing intensity fluctuation of M values – see Fig. 1(C), where each curve corresponds to a single I_{SPC} dataset. Then PL snapshot $m(t)$ is then retrieved from the underdetermined dataset by using a standard SPC retrieval:

$$min\{||Am(t) - I_{SPC}||_2^2 + TV(m(t))\}. \tag{5}$$

The sensing matrix A is formed from vectorized excitation patterns, TV stands for the total variation calculation.

By reconstructing a temporal snapshot for each delay t, we get a 3D datacube, which contains PL decay in every i-th pixel of the sample $I_D(i,t)$. The whole concept is illustrated and summarized in Fig. 1.

Optics EXPRESS

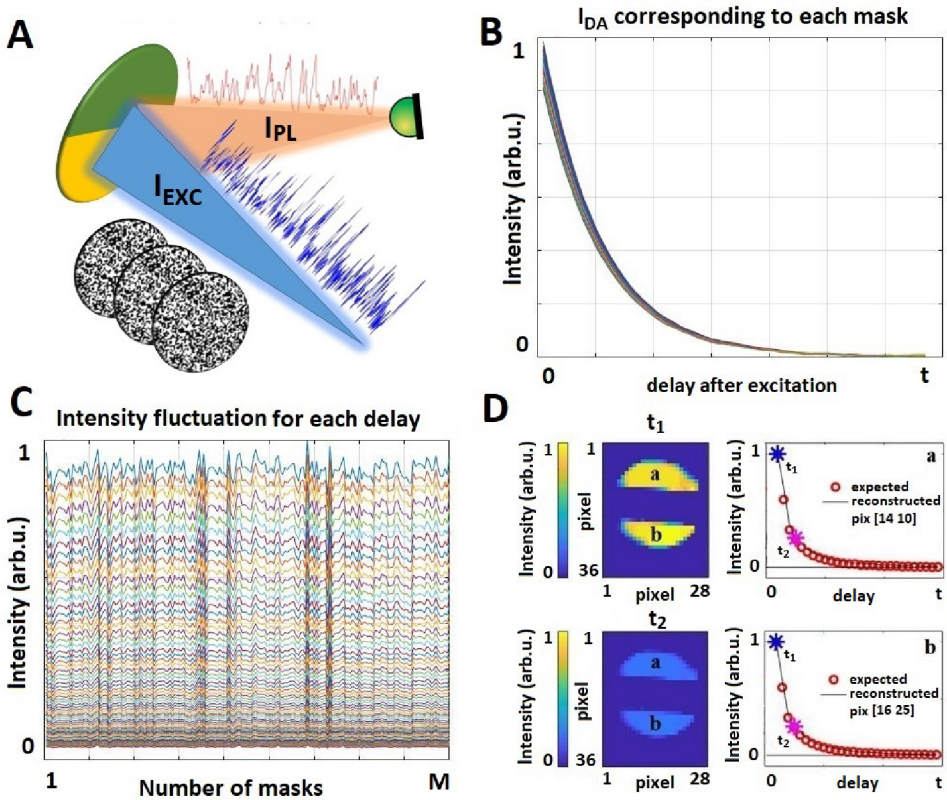

Fig. 1. (A) Scheme of 2D-RATS approach, where the sample is illuminated with a set of random patterns (masks) blinking according to I_{EXC}. The total PL intensity waveform I_{PL} is detected for each mask with a single-pixel detector. (B) Example of a set of calculated I_{DA}'s for corresponding masks – see Eq. (4). (C) Intensity fluctuation for each delay after excitation of I_{DA}. Knowing the fluctuation (I_{SPC} signal) and set of masks makes it possible to determine the PL map m at a given delay after excitation of I_{DA} using compressed sensing algorithms. (D) An example of reconstructed PL maps in delays t_1 and t_2. Plotted I_D's corresponding to pixel [14 10] (area "a") and to pixel [16 25] (area "b").

3. Noise effect simulation

A small contribution of noise can be expected in each measured signal in the experiment. In order to maintain stable conditions, the role of the noise was explored through simulations. A primary signal I_{EXC} was simulated using temporal speckles patterns [23], which are cornerstones of a random analog signal generator presented in our previous work [10]. The length of the simulated I_{EXC} signal was 0.1 s with an impulse response function of FWHM of 2.07µs. The PL decay I_D was considered with the lifetime $\tau = 20$ µs. Used noise levels throughout the article are consistent with the noise that can be expected in a realistic experiment [15]. In the current optical setup, an amplified signal from a photomultiplier is used for I_{PL} detection, and this sensitive part is the main source of the noise. The noise originates from scattered excitation photons and the noise induced in the detector itself, which is based on shot noise and standard electronic noise. The experimentally observed noise can be very well described with a flat frequency dependence, i.e., white noise.

Optics EXPRESS

The excitation signal I_{EXC} was simulated as a non-periodic random signal. The importance of a non-periodic signal will be explained in section 4.1. It is worth noting that with the exception of section 4.3, the regularization parameter ε (Eq. (2) and Eq. (4), respectively) is considered as $\varepsilon = 0.1$.

3.1. 0D-RATS

To demonstrate the basic steps, we shall start with the non-imaging RATS, i.e., 0D-RATS. We use two datasets of I_{EXC} and I_{PL}, which are subsequently used to retrieve the PL decay via Eq. (2). Therefore, we initially simulated the effect of noise present in these two datasets.

Firstly, we added white noise to I_{EXC}, while I_{PL} was kept absolutely noiseless (Fig. 2(A)) and vice versa (Fig. 2(B)). In both datasets in Fig. 2, the signal-to-noise ratio (SNR) was 15.2 dB which corresponds to 3% percent of noise in the system (see Eq. (6)).

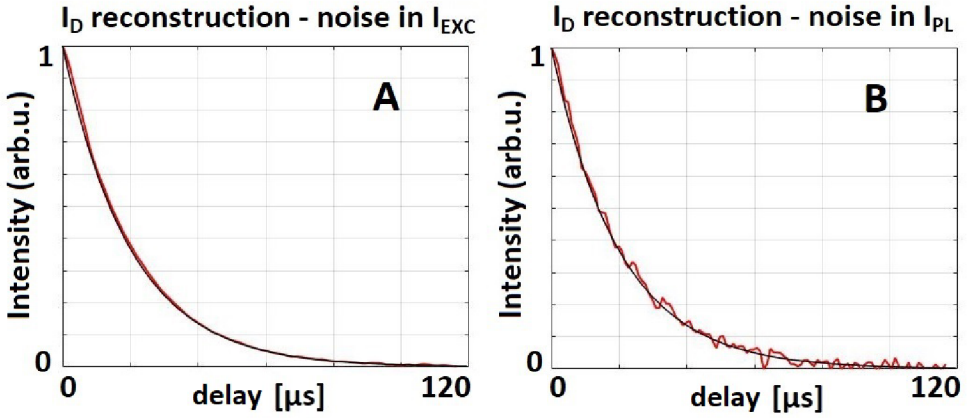

Fig. 2. (A) Reconstructed I_D with a noise level of 3% in I_{EXC}, which corresponds with SNR about 15.2 dB. I_{PL} was assumed noiseless. (B) Reconstructed I_D with a noise level of 3% in I_{PL}, corresponding with SNR about 15.2 dB. I_{EXC} was assumed noiseless.

For both retrieved decays in Fig. 2 (red lines), the noise had an effect on reconstructed I_D, but the investigated PL dynamics were not biased, i.e., the overall decay shape was not altered, and it was in perfect agreement with the expected output (black lines). Nevertheless, we observed that the noise in the I_{PL} dataset had a significantly more pronounced effect on the resulting noise in the retrieved PL decay (Fig. 2(B)).

$$SNR[dB] = -10\log_{10}\left(\frac{noise[\%]}{100}\right). \tag{6}$$

We can quantify the noise level by the root-mean-square error, which reaches $RMSE_{PL} = 12.9 \cdot 10^{-3}$ for the noise in the PL signal and $RMSE_{EXC} = 2.8 \cdot 10^{-3}$ for the noise in the excitation signal. That suggests that regularization in the denominator of Eq. (2) has a more pronounced effect on I_{EXC} than I_{PL}, which becomes the dominating source of noise in the retrieved decay.

3.2. 2D-RATS

As the next step, we also simulated the effect of noise in the I_{PL} and I_{EXC} signal on the 2D-RATS experiment. Here, the situation is more complex because the noise present in the I_{PL} and I_{EXC} datasets is first transposed into the noise of the retrieved PL decay curve $I_{DA}(t)$ from Eq. (4). The noise present in these curves is then propagating into the SPC signal I_{SPC}, which is then used for the retrieval of the set of PL snapshots for each delay in Eq. (5).

Optics EXPRESS

All simulated reconstructions were performed using binary masks. We used the reconstruction algorithm based on the sparsity of total variation TVAL3 [24,25]. The main parameters of the TVAL3 algorithm were: *mu* (2^{11}), *beta* (2^7). As an investigated sample, we used Matlab predefined image Phantom, where the PL decay with a single lifetime of $\tau = 20$ µs was set to be constant all over the Phantom's "body". Acquisition time and other conditions simulating real experiments were kept the same as for the 0D-RATS simulations above.

We carried out the same calculation as we presented in Section 3.1, and we show in Fig. 3 the retrieved PL snapshots *m(t)* in the peak PL intensity, i.e., $t = 0$ µs, where the contrast of the PL signal is the highest. The case was studied for three different SPC compression ratios $k = 0.4$, 0.6, 0.8 and four signal-to-noise ratios $SNR = 15.2$, 18.2, 20, 23 dB, which corresponds to 3%, 1.5%, 1%, 0.5% level of noise in the signal.

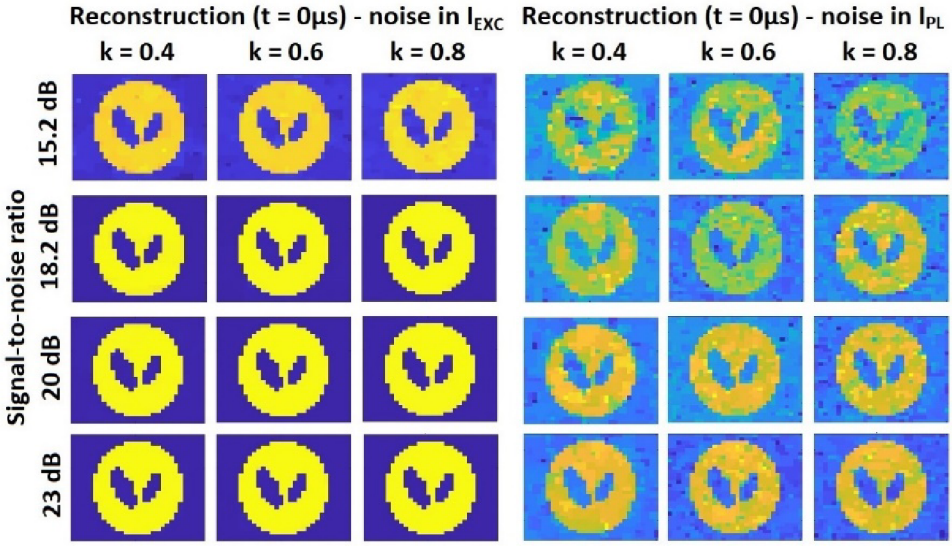

Fig. 3. Left part: reconstructions of PL map m in delay with maximal intensity (t = 0 µs) in case of noise in I_{EXC}. Right part: reconstructions of PL map m in delay with maximal intensity (t = 0 µs) in case of noise in the I_{PL}. The noise parameters are for both SNR = 15.2, 18.2, 20, 25 dB (rows) and the compression ratios are k = 0.4, 0.6, 0.8 (columns).

The results are summarized in Fig. 3 for the noise introduced in the I_{EXC} signal (left-hand side) and the noise introduced in the I_{PL} signal (right-hand side), and the corresponding resulting noise levels are presented in Table 1.

Analogously to the 0D-RATS, the noise in I_{PL} has a significantly worse effect on the image retrieval than the noise in the I_{EXC} signal. By comparing different noise levels (compare lines in Fig. 3), one can see that the *SNR* of the I_{PL} is the main limiting factor in the snapshot retrieval. The effect of compression ratio (compare columns in Fig. 3) does not play any significant role for the values above 0.4. This means that it is not efficient to compensate for higher noise in the measured signal by simply increasing the number of measured excitation masks.

To quantify the effect of each parameter, we introduced three different measures. Firstly, we can judge the image reconstruction quality, where we compare the retrieved snapshot m (in delay $t = 0$ µs) with the actual image used in simulations U by using Frobenius norm of the two:

$$R = \frac{||m - U||_F}{||U||_F}. \tag{7}$$

Optics EXPRESS

Table 1. Quality of the retrieved image (R, lower number = higher quality) and SPC signal (SPC-SNR, higher number = higher quality) corresponding to Fig. 3 for noise introduced via IEXC and IPL signal.

	noise source	k	noise level			
			SNR 15.2dB	SNR 18.2dB	SNR 20dB	SNR 23dB
R	EXC	0.4	0.177	0.158	0.150	0.142
		0.6	0.175	0.155	0.149	0.142
		0.8	0.175	0.155	0.149	0.142
	PL	0.4	0.328	0.265	0.242	0.191
		0.6	0.312	0.264	0.215	0.192
		0.8	0.326	0.261	0.224	0.181
SPC-SNR	EXC	0.4	38.01	43.80	48.14	54.97
		0.6	38.06	43.84	48.05	55.04
		0.8	37.98	43.90	48.25	55.16
	PL	0.4	34.67	37.52	39.53	43.24
		0.6	34.86	37.45	40.01	43.10
		0.8	34.84	37.83	39.48	42.72

We can also focus on the PL dynamics for each pixel i, where the reconstructed decay curve $I_{DREC}(i)$ is normalized and compared with the actual decay curve $I_{\mathrm{D}}(i)$, which was used to simulate the data. The comparison was made from $t_0 = 0$ µs to $t_{\mathrm{T}} = 120$ µs, which is a sufficient temporal range for the decay curve with a lifetime of 20 µs. We denote this error as the decay deviation σ:

$$\sigma = \frac{1}{N}\sum_{i=1}^{N}\sum_{t=t_0}^{t_\tau}\sqrt{(I_{DREC}(i,t) - I_D(i,t))^2}. \tag{8}$$

Finally, we also determined the SNR of the I_{SPC} signal, which is used for the image retrieval m in delay $t = 0$ µs. Note that the I_{SPC} signal indicates the fluctuation of I_{DA} curves corresponding to the respective delay. The fluctuations (I_{SPC}) are affected by the noise in both I_{EXC} and I_{PL}. We extract the I_{SPC} noise level to provide a comparison to other SPC experiments. $SPC\text{-}SNR_{EXC}$ denotes the signal-to-noise level in I_{SPC} when the noise was added to I_{EXC} and $SPC\text{-}SNR_{PL}$ indicates the case when the noise was added to the I_{PL}. Analogously, the indices "PL" and "EXC" have the same meanings for R_{EXC} and R_{PL} or σ_{EXC} and σ_{PL}.

4. Noise level optimization

In Section 3, we studied the effect of the noise level in the I_{EXC} respective I_{PL} simulated dataset on the retrieval of the PL decay curve and PL snapshot. The noise levels are determined by the properties of an optical setup, which features a certain photon budget (number of detectable photons), types of detectors, and samples. For an optimized optical setup, such characteristics can not be easily improved.

On the other hand, it is possible to enhance the quality of the retrieved PL decay or FLIM on the expenses of the acquisition time. Therefore, we studied the benefits connected to a longer acquisition time. Due to the fact that the RATS method is based on signal deconvolution, an important factor is the periodicity of the signal, as we discuss in the following subsection.

4.1. Periodic extension of acquisition time

A straightforward approach to improve the quality of the PL decay I_{D} retrieval via Eq. (2) is to repeat the same measurement for the same excitation waveform. Hence, we attain a periodic I_{EXC}

Optics EXPRESS

and I_{PL} signal. However, it is worth stressing that the use of a periodic signal I_{EXC} will create unwanted artefacts in the retrieved data. It follows from the nature of deconvolution in Eq. (2) that such periodic excitation waveform leads to a periodic I_D signal with a lower amplitude. We will demonstrate this effect on a 0D-RATS simulation.

We compared the retrieved PL decay (I_D curve) in the case of a non-periodic I_{EXC} signal with a duration of 0.1 s and a periodic I_{EXC} signal (7 periods) with the same total duration of 0.1 s. This is illustrated by Fig. 5. For completeness, we present in Fig. 4 the non-periodic signal used and the periodic signal counting seven periods. Both signals were simulated based on simulations of randomly changing speckle patterns [23], which corresponds with excitation signals generated via a random signal generator (lens-rotary diffuser-aperture) presented in our previous work [10]. Due to the rotating diffuser, a periodic signal can be expected, which due to small vibrations may be rather quasi-periodic. However, a perfectly periodic and non-periodic signal can be achieved via a suitable laser modulation.

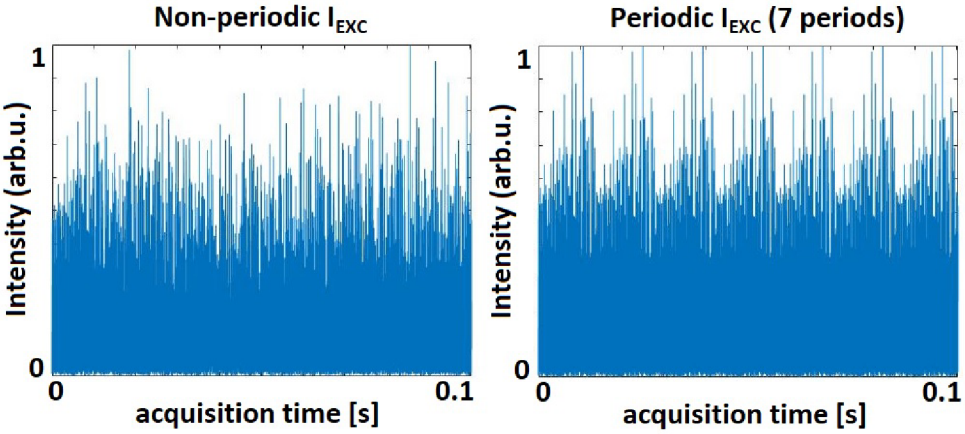

Fig. 4. Used excitation non-periodic signal (left panel) and periodic signal with 7 periods (right panel). Both signals were simulated based on simulations of randomly changing speckle patterns [23], which corresponds with excitation signals generated via generator (lens-rotary diffuser-aperture) presented in our previous work [10].

The entire retrieved PL dataset is depicted in Fig. 5. The comparison between the periodic and non-periodic excitation – see right and left-hand side, respectively – shows that the amplitude of the retrieved PL for the periodic I_{EXC} signal is about seven times smaller compared to the non-periodic case and the PL signal has multiple replicas.

When we zoom in Fig. 5(B) into the PL dynamics during the first hundreds of microseconds, i.e., one of the PL decay replicas, we get after normalization the correct I_D following the actual decay – see Fig. 6. However, the resulting *SNR* is decreased. We tested in Fig. 6 the noise introduced via the excitation signal I_{EXC} (panel A) and PL signal I_{PL} (panel B). The root-mean-square error for curves in Fig. 6 reaches $RMSE_{PL} = 29.7 \cdot 10^{-3}$ and $RMSE_{EXC} = 7.8 \cdot 10^{-3}$ for the noise introduced in the I_{PL} and I_{EXC} signal, respectively. The noise level in Fig. 6 can be directly compared to Fig. 2, where we used a non-periodic signal and where $RMSE_{PL} = 12.9 \cdot 10^{-3}$ and $RMSE_{EXC} = 2.8 \cdot 10^{-3}$. For the non-periodic signal, the resulting noise level was more than 2-times lower.

To further illustrate this behavior, we carried out a set of simulations, where we kept a constant total acquisition time of 0.1 s, while the I_{EXC} signal was set to be periodic with up to 16 periods – see Fig. 7. The root-mean-square error increases with the number of periods for both situations – noise in the I_{EXC} and I_{PL} signal. Therefore, for the sake of optimum signal reconstruction in the RATS method, it is worth avoiding any periodicity in the I_{EXC} signal.

Optics EXPRESS

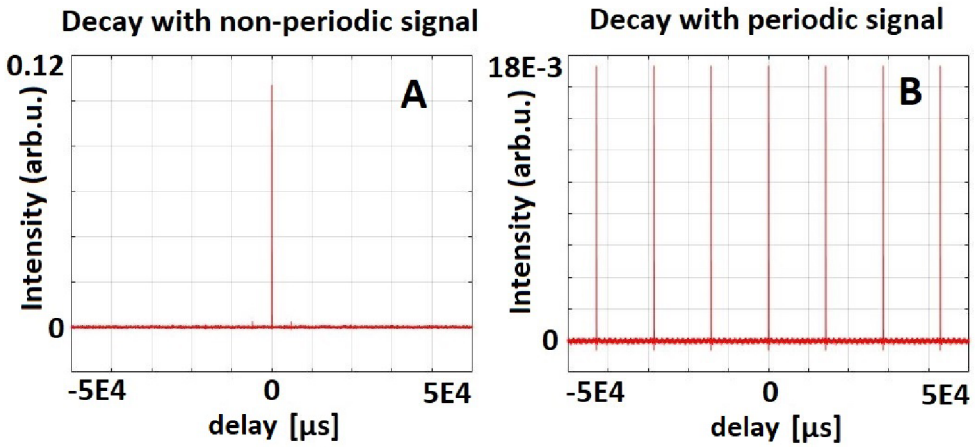

Fig. 5. Results of I_D reconstruction (deconvolution), when non-periodic (panel A) and periodic (panel B) I_{EXC} was used for sample excitation with lifetime $\tau = 20$ µs.

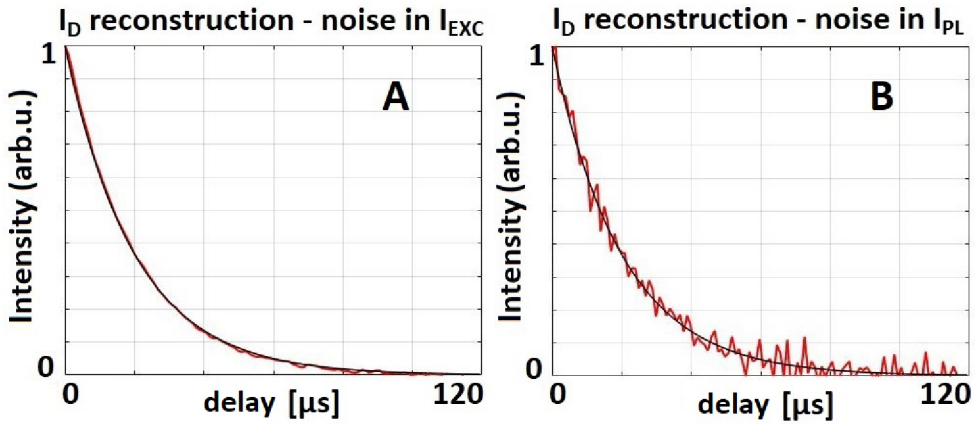

Fig. 6. Zoomed results of I_D reconstruction ($\tau = 20$ µs.), when I_{EXC} was used as a periodic signal (7 periods). Redline is reconstructed data, and the black line is reference data. (A) Reconstruction with an amount of noise of 3% in I_{EXC} (correspond with SNR about 15.2 dB). (B) Reconstruction with an amount of noise of 3% in I_{PL} (correspond with SNR about 15.2 dB).

Optics EXPRESS

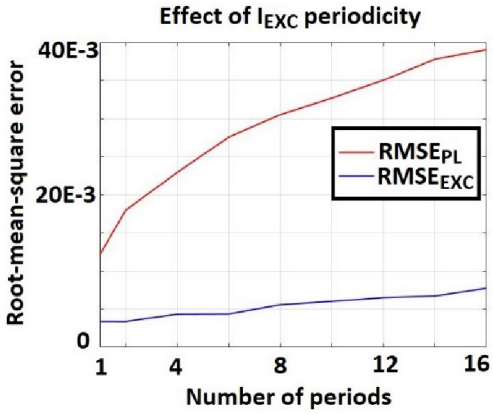

Fig. 7. RMSE of I_D for a periodical I_{EXC} with a constant total acquisition time of $t_{acq} = 0.1$ s. The number of periods in the I_{EXC} signal is varied. I_{PL} respective I_{EXC} noise level: SNR 15.2 dB.

4.2. Non-periodic acquistion time extension

The possible way to suppress the noise effect is to extend the acquisition time so that we avoid any I_{EXC} signal periodicity. This approach favors frequencies representing the true signal in the Fourier spectrum and suppresses the contribution of white noise. We carried out simulations corresponding to the 2D-RATS measurement presented in Fig. 3. Nevertheless, here we used a set of acquisition times $t_{acq} = 0.1$ s, $t_{acq} = 0.2$ s, $t_{acq} = 0.4$ s, $t_{acq} = 1$ s and $t_{acq} = 2$ s. Other conditions, such as reconstruction parameters, regularization parameter ε, and signal properties, were kept the same as in Section 3.

As in Section 3.2, we focus on the quality of the retrieved image (R_{EXC}, R_{PL}), noise introduced into the SPC signal ($SPC\text{-}SNR_{EXC}$, $SPC\text{-}SNR_{PL}$) in delay t = 0 µs. Moreover, this section also focuses on the deviation of the whole reconstructed PL decay in each pixel of the sample (σ_{EXC}, σ_{PL}).

Dependences of each noise characteristics on the acquisition time are presented in Fig. 8–10. In these figures, the line/symbol color indicates the given *SNR* (red: 15.2dB, blue: 18.2dB, black: 20dB and magenta: 23dB); line/symbol type represent the compression ratio k (cross: 0.8, circle: 0.6, full line: 0.4).

All the results in Fig. 8–10 confirm that the effect of noise level (varying color) is much more pronounced than the compression ratio (varying line/symbol type), i.e., increasing the number of excitation patterns above 40% compared to the number of the pixel has a negligible effect on the image quality.

When we focus on the noise introduced via I_{EXC} signal, it has a low effect on the resulting image reconstruction – see Fig. 3, left-hand side. For this reason, the change in the acquisition time has almost no effect on the resulting noise level regarding the image quality and SPC signal error (see Fig. 8,9). A subtle peak in Fig. 8 for the acquisition time 0.2 s and a decrease in Fig. 9 for the same acquisition time are connected. They both indicate an increased amount of noise in the I_{SPC} signal for the given case of PL map reconstruction at delay t = 0 µs, which is unexpected in light of the other results. However, we should consider that this result is connected just with only one delay point ($t = 0$ µs). If we take into account the whole decay curve I_D (signal-to-noise ratio in all SPC signals connected with delay points of the curve I_D), which is shown in Fig. 10, it can be observed that this irregularity is averaged out.

On the contrary, for the noise introduced via the I_{PL} signal, we can highly improve the quality of the retrieved image by the increased acquisition time. This image quality enhancement is

Optics EXPRESS

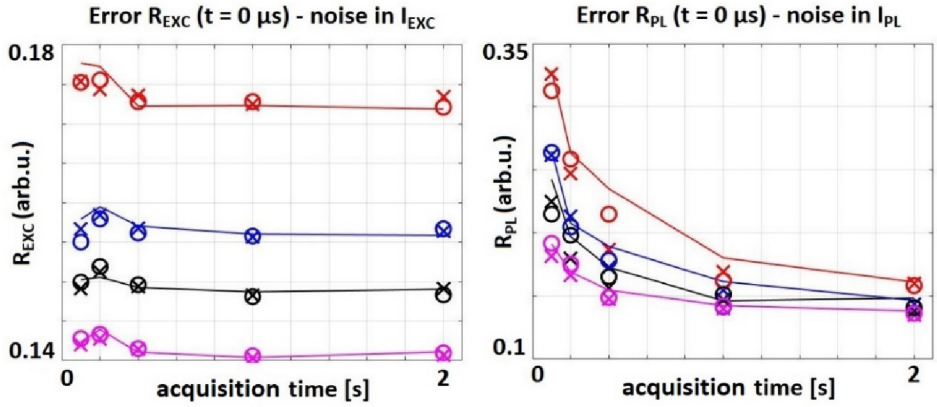

Fig. 8. Reconstruction error R_{EXC} (left part), R_{PL} (right part) at the delay t = 0 µs dependence on sensing time for different SNR: 15.2 dB (red), 18.2 dB (blue), 20 dB (black), 23 dB (magenta) and three different compression ratio k = 0.4 (full line), k = 0.6 (circle), k = 0.8 (cross).

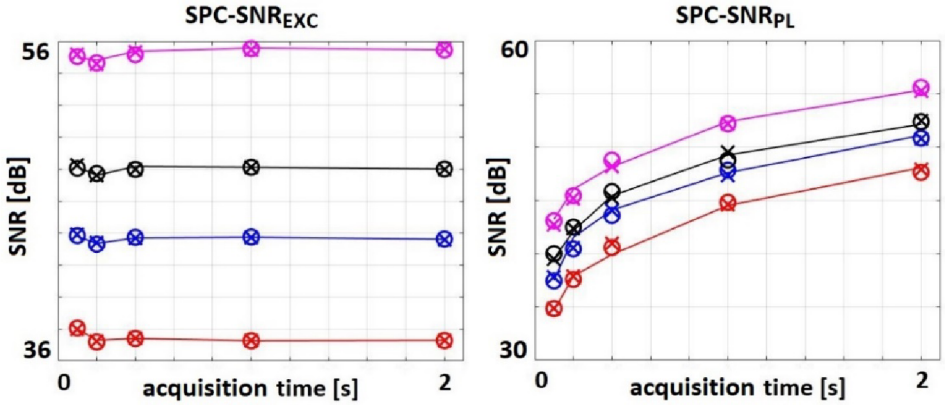

Fig. 9. Noise dependence in SPC signal (random fluctuation in intensity of I_D in delay t = 0 µs, because of changing illumination masks) on sensing time according to added noise to I_{EXC} (left part) and I_{PL} (right part) with SNR: 15.2 dB (red), 18.2 dB (blue), 20 dB (black), 23 dB (magenta) and three different compression ratio k = 0.4 (full line), k = 0.6 (circle), k = 0.8 (cross).

Optics EXPRESS

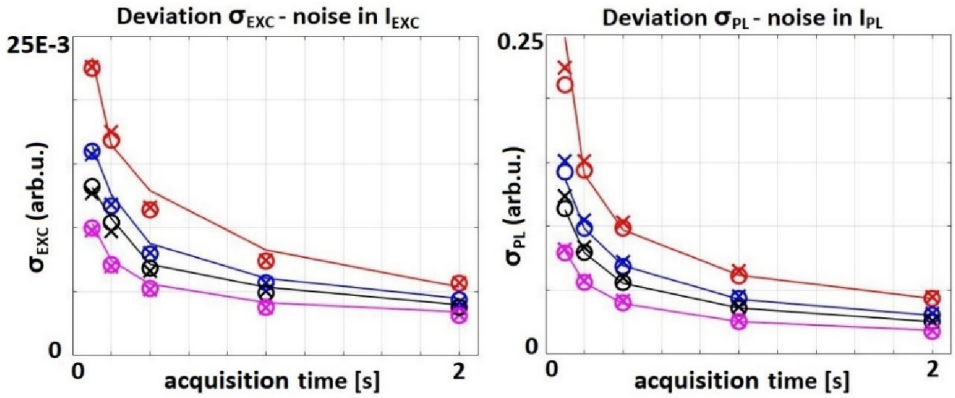

Fig. 10. Acquisition time dependance of σ_{EXC} – noise added to I_{EXC} (left part) and σ_{PL} – noise added to I_{PL} (right part). SNR: 15.2 dB (red), 18.2 dB (blue), 20 dB (black), 23 dB (magenta) and three different compression ratio k = 0.4 (full line), k = 0.6 (circle), k = 0.8 (cross).

much more pronounced for higher noise levels. In the case where the noise level is 15.2 dB (3%), the R_{PL} will decrease by 50%, while when the noise level is 23 dB (0.5%), the R_{PL} will decrease by only 25%.

The results described in Fig. 8 are linked to the results presented in Fig. 9. As expected, the highest *SPC-SNR*$_{EXC}$ and *SPC-SNR*$_{PL}$ are reached for the lowest noise level in the system - *SNR* = 23 dB (0.5%). On the other hand, the *SPC-SNR*$_{PL}$ increases as the acquisition time increases, which results in a decrease in the R_{PL}. An interesting finding is that when the acquisition time is extended to 2s, the *SPC-SNR*$_{PL}$ increases even above the *SPC-SNR*$_{EXC}$ value corresponding to this acquisition time. Consequently, the same trend is observed for the R_{PL} and R_{EXC} values at a scanning time of 2 s.

Although it was stated that R_{EXC} and *SPC-SNR*$_{EXC}$ do not change significantly with the acquisition time, it is worth noting that these values represent only a single PL snapshot at the selected delay $t = 0$ µs. The effect of acquisition time is notable for the decay curve reconstruction, which is highly improved both for the noise in I_{EXC} and I_{PL} – see σ in Fig. 10. Decay deviation σ decreases with the increasing acquisition time. Although both errors are in a different order of magnitude, by increasing the acquisition time from 0.1 s to 2 s, both σ errors decreased by the same ratio.

4.3. *Regularization parameter effect*

Another way to suppress the effect of noise is to change the regularization parameter ε in Eq. (2) and Eq. (4). The regularization parameter makes it possible to solve the ill-conditioned problem, where "division by zero" could occur for frequencies with very low amplitude in the I_{EXC} signal [26]. The regularization parameter adds a part of the averaged power of the spectrum to the denominator of the Eq. (2) respective Eq. (4) and thus suppresses the influence of less frequent frequencies in the signal (white noise). As a result, the calculated I_D or I_{DA} is smoothed.

As in the previous section, the influence of the parameter ε was investigated regarding the quality of the reconstructed PL snapshot at the zero delay after excitation, which corresponds to the maximum PL intensity. All simulations were carried with the acquisition time of 0.1 s and a range of ε from 0.05 to 1. Reconstruction parameters and signal properties were held the same as in Section 3. Figure 11–13 follow the same color scheme as in the previous section with respect to *SNR* (color) and compression ratio (line/symbol type).

Optics EXPRESS

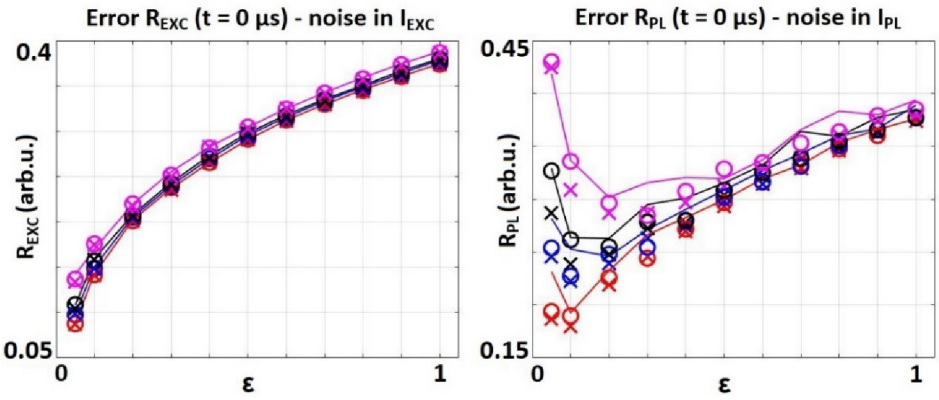

Fig. 11. Reconstruction error R_{EXC} (left part), R_{PL} (right part) at the delay t = 0 μs dependence on ε - different SNR: 15.2 dB (red), 18.2 dB (blue), 20 dB (black), 23 dB (magenta) and three different compression ratio k = 0.4 (full line), k = 0.6 (circle), k = 0.8 (cross).

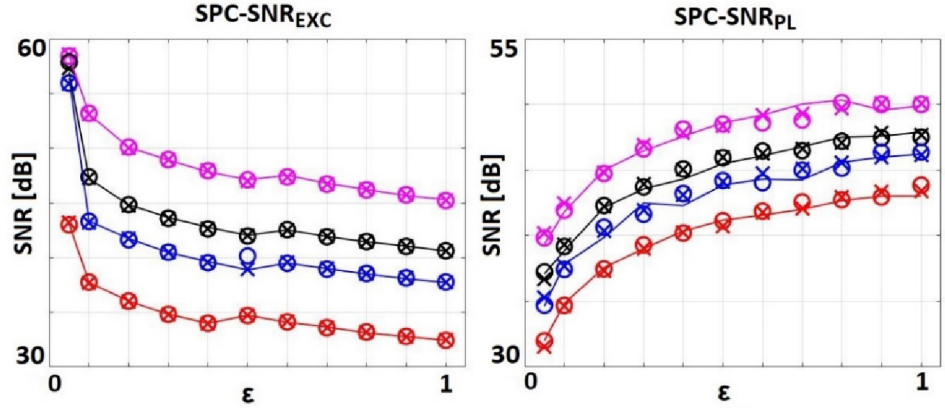

Fig. 12. Noise dependence in SPC signal (random fluctuation in intensity of I_D in delay t = 0 μs, because of changing illumination masks) on ε according to added noise to I_{EXC} (left part) and I_{PL} (right part) with SNR: 15.2 dB (red), 18.2 dB (blue), 20 dB (black), 23 dB (magenta) and three different compression ratio k = 0.4 (full line), k = 0.6 (circle), k = 0.8 (cross).

Optics EXPRESS

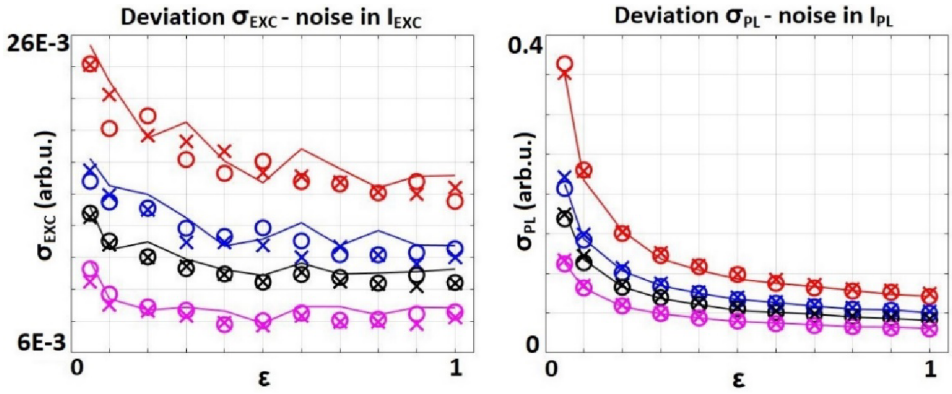

Fig. 13. ε dependance of σ_{EXC} – noise added to I_{EXC} (left part) and σ_{PL} – noise added to I_{PL} (right part). SNR: 15.2 dB (red), 18.2 dB (blue), 20 dB (black), 23 dB (magenta) and three different compression ratio k = 0.4 (full line), k = 0.6 (circle), k = 0.8 (cross).

In accordance with the previous results, the effect of the added noise is much more pronounced than the compression ratio used. We will first focus on the influence of regularization parameter ε on the quality of the retrieved image, i.e., R_{EXC} and R_{PL} – see Fig. 11. In these results, we see an interplay of two effects: the smoothing of the I_{DA} and I_D, respectively, and the bias of the reconstructed I_{DA} respective I_D.

Since the noise level in the I_{EXC} affects the I_{DA} reconstruction less than in I_{PL}, the effect of biased reconstruction of I_{DA} prevails and the R_{EXC} error increase with ε. Whereas in the case of R_{PL}, the noise smoothing effect prevails in I_{DA} for the low ε values and the R_{PL} decreases. However, with increasing ε, the bias effect becomes dominant and the image quality is decreased again.

This is confirmed by Fig. 12, which shows the amount of noise in the individual $SPC\text{-}SNR_{EXC}$ and $SPC\text{-}SNR_{PL}$. This implies that for the given noise level in the I_{PL} signal, there is an optimum regularization parameter providing the best results and this provides a guideline of the optimum ε value.

Figure 13 focuses on σ, which evaluates the fidelity of the reconstructed decay curves. Here, with increasing ε, both σ_{EXC} and σ_{PL} decrease despite the bias effect, i.e., a higher ε value provides a better estimate of the decay curve. We ascribe it to the fact that with decreasing intensity of I_{DA} (the following delay after excitation), the noise level in the SPC signal increases, and thus the smoothing effect of the regularization parameter prevails over the bias effect.

Both the dependence of σ_{EXC} and σ_{PL} on ε are influenced by the amount of noise in the system. Especially for the high-noise PL signal (15.2 dB, 3%), the increase of ε from 0.05 to 1 reduced the σ_{PL} by 79%. Analogously to the previous results, the increase in regularization parameter has a lower effect on the noise introduced via I_{EXC} signal – see σ_{EXC}, which decreases by 32% for the same noise level and ε change.

5. Conclusion

In this paper, we carried out an extensive analysis of the effect of noise within the RATS technique – a novel method for the PL decay reconstruction and FLIM. As we mentioned in the introduction, the method can now be used mainly in materials engineering due to the possibility of detecting PL decays at the microsecond or sub-microsecond level. However, ongoing research opens the possibility of measuring in units of nanoseconds, which could open up further possibilities for the characterization of a range of optical materials, chemical substances, as well as biological

Optics EXPRESS

samples. Since this is a new method, the findings presented are important for the further direction of the method. The problem was investigated using simulations for cases with noise levels reaching 0.5–3% (*SNR* 23–15.2dB) of the signal. To disentangle the effect of each noise source, the noise was added to I_{EXC} only and I_{PL} was left noiseless and vice versa.

We consistently observed that the same noise level has a significantly greater effect when present in the I_{PL}, which we ascribe to the fact that the regularization parameter ε is associated with the I_{EXC} in the denominator of the relationship Eq. (2) and Eq. (4). Hence, the most efficient strategy to improve the data quality is to focus on the I_{PL} intensity level and the connected noise.

Secondly, all our data simulations revealed that the effect of noise level is incomparably more important than the compression ratio k, i.e., the number of measured excitation masks in the single-pixel experiment. In other words, for $k > 0.4$, it is not possible to compensate for a higher noise level by increasing the number of excitation masks.

It is also essential to avoid using periodic excitation signals, which can cause periodicity in the retrieved decay and increase the resulting I_D relative noise level. It is worth noting that the RATS method was originally based on an analog random signal generator, the main component of which is a rotary diffuser. Therefore, we attained a quasi-periodic signal, which played a significant role in the method. Using a non-periodic signal, for instance, by laser modulation, a greater signal-to-noise ratio will be obtained.

As expected, we observed that increasing the acquisition time of a single decay measurement (single excitation mask) can highly reduce the resulting noise and effectively compensate for the noise present in the PL measurement. The choice of acquisition time is also connected with the *IRF* of the signal and the expected PL lifetimes. Moreover, it fundamentally manages total sensing time during which the entire data set is acquired from all masks. Here we used lifetime $\mathsf{T} = 20$ µs, so that I_{EXC} signal with $IRF = 2.07$ µs was selected with data sampling 0.99 µs. For other signal parameters, different results than those presented here can be achieved after the same signal length extension. If we focus on shorter lifetimes, a faster signal (smaller *IRF*) is needed, and the total scanning time is also reduced in a given ratio. However, the simulated trends for *R*, *SPC-SNR*, and σ can be applied without compromising generality.

In order to suppress signal noise, we have deliberately avoided any mathematical signal filtering techniques so that we do not lose important information due to the random nature of the signal. Mathematical signal filtering could be optimized on the expenses of the general applicability of the results. Therefore, we explored instead the possibility to optimize the regularization parameter ε used in the PL decay retrieval.

The parameter ε was changed in the range 0.05 to 1. We observed a trade-off between the two effects. On the one hand, a higher value of ε smoothes the I_{DA} curve, while, on the other hand, it distorts the I_{DA} because some frequencies of the Fourier spectrum are favored. Therefore, we observed that there is an optimum value of ε connected to the noise level in the I_{PL} signal. As a rule of thumb, for a system with a low noise level, we recommend keeping the parameter ε at 0.1 or 0.2. For a system with a high noise level, it is possible to increase the regularization parameter ε more significantly.

Funding. Ministerstvo Školství, Mládeže a Tělovýchovy (CZ.02.1.01/0.0/0.0/16_026/0008390); Technická Univerzita v Liberci (SGS-2021-3003).

Acknowledgment. We gratefully acknowledge the Mechanics laboratory of TOPTEC (Institute of Plasma Physics, Czech Academy of Sciences) for providing us with unique optomechanics components since the beginning of RATS method development.

Disclosures. The authors declare no conflicts of interest.

Data availability. Data underlying the results presented in this paper are not publicly available at this time but may be obtained from the authors upon reasonable request.

Optics EXPRESS

References

1. R. Cubeddu, D. Comelli, C. D'Andrea, P. Taroni, and G. Valentini, "Time-resolved fluorescence imaging in biology and medicine," J. Phys. D: Appl. Phys. **35**(9), 201R61 (2002).
2. S. Kalinina, J. Breymayer, P. Schäfer, E. Calzia, V. Shcheslavskiy, W. Becker, and A. Rück, "Correlative NAD(P)H-FLIM and oxygen sensing-PLIM for metabolic mapping," J. Biophotonics **9**(8), 800–811 (2016).
3. C. D. Wilms, H. Schmidt, and J. Eilers, "Quantitative two-photon Ca2 + imaging via fluorescence lifetime analysis," Cell Calcium **40**(1), 73–79 (2006).
4. K. Žídek, F. Trojánek, P. Malý, L. Ondič, I. Pelant, K. Dohnalová, L. Šiller, R. Little, and B. R. Horrocks, "Femtosecond luminescence spectroscopy of core states in silicon nanocrystals," Opt. Express **18**(24), 25241–25249 (2010).
5. W. Becker, *Advanced Time-Correlated Single Photon Counting Techniques*, (Springer, Berlin, 2005).
6. J. Sytsma, J. M. Vroom, D. Grauw, and H. C. Gerritsen, "Time-gated fluorescence lifetime imaging and microvolume spectroscopy using two-photon excitation," J. Microsc. **191**(1), 39–51 (2008).
7. J. Qu, L. Liu, D. Chen, Z. Lin, G. Xu, B. Guo, and H. Niu, "Temporally and spectrally resolved sampling imaging with a specially designed streak camera," Opt. Lett. **31**(3), 368–370 (2006).
8. Y. Won, S. Moon, W. Yang, D. Kim, W.-T. Han, and D. Y. Kim, "High-speed confocal fluorescence lifetime imaging microscopy (FLIM) with the analog mean delay (AMD) method," Opt. Express **19**(4), 3396–3405 (2011).
9. E. Gratton, S. Breusegem, J. D. B. Sutin, Q. Ruan, and N. P. Barry, "Fluorescence lifetime imaging for the two-photon microscope: time-domain and frequency-domain methods," J. Biomed. Opt **8**(3), 381–390 (2003).
10. J. Junek, L. Ondič, and K. Žídek, "Random temporal laser speckles for the robust measurement of sub-microsecond photoluminescence decay," Opt. Express **28**(8), 12363–12372 (2020).
11. J. Junek and K. Žídek, "Fluorescence lifetime imaging via spatio-temporal speckle patterns in a single-pixel camera configuration," Opt. Express **29**(4), 5538–5551 (2021).
12. K. Zheng, K. Žídek, M. Abdellah, M. E. Messing, M. J. Al-Marri, and T. Pullerits, "Trap States and Their Dynamics in Organometal Halide Perovskite Nanoparticles and Bulk Crystals," J. Phys. Chem. C **120**(5), 3077–3084 (2016).
13. J. M. Griffin, A. J. Miller, A. J. Berry, S. Wimperis, and S. E. Ashbrook, "Dynamics on the microsecond timescale in hydrous silicates studied by solid-state 2H NMR spectroscopy," Phys. Chem. Chem. Phys. **12**(12), 2989–2998 (2010).
14. K. Dohnalová, L. Ondič, K. Kůsová, I. Pelant, J. L. Rehspringer, and R.-R. Mafouana, "White-emitting oxidized silicon nanocrystals: Discontinuity in spectral development with reducing size," J. Appl. Phys. **107**(5), 053102 (2010).
15. P. Pande and J. A. Jo, "Automated Analysis of Fluorescence Lifetime Imaging Microscopy (FLIM) Data Based on the Laguerre Deconvolution Method," IEEE Trans. Biomed. Eng. **58**(1), 172–181 (2011).
16. A. B. Watson, "Probability summation over time," Vision Res. **19**(5), 515–522 (1979).
17. T. Regińska, "A Regularization Parameter in Discrete Ill-Posed Problems," SIAM J. Sci. Comput. **17**(3), 740–749 (1996).
18. H. W. Engl, "On the choice of the regularization parameter for iterated Tikhonov regularization of III-posed problems," J. Approximation Theory **49**(1), 55–63 (1987).
19. V. Studer, J. Bobin, M. Chahid, H. S. Mousavi, E. Candes, and M. Dahan, "Compressive fluorescence microscopy for biological and hyperspectral imaging," Proc. Natl. Acad. Sci. U. S. A. **109**(26), E1679–E1687 (2012).
20. Q. Pian, R. Yao, N. Sinsuebphon, and X. Intes, "Compressive hyperspectral time-resolved wide-field fluorescence lifetime imaging," Nat. Photonics **11**(7), 411–414 (2017).
21. K. Žídek, O. Denk, and J. Hlubuček, "Lensless Photoluminescence Hyperspectral Camera Employing Random Speckle Patterns," Sci. Rep. **7**(1), 15309 (2017).
22. M. F. Duarte, M. A. Davenport, D. Takhar, J. N. Laska, T. Sun, K. F. Kelly, and R. G. Baraniuk, "Single-pixel imaging via compressive sampling," IEEE Signal Process. Mag. **25**(2), 83–91 (2008).
23. F. Gascón and F. Salazar, "A simple method to simulate diffraction and speckle patterns with a PC," Optik **117**(2), 49–57 (2006).
24. C. Li, Wotao Yin, and Yin Zhang, TVAL3 Home, Rice University, 2009, Last updated 11/07/2013, https://www.caam.rice.edu/~optimization/L1/TVAL3/.
25. C. Li, W. Yin, and Y. Zhang, "User's guide for TVAL3: TV minimization by augmented lagrangian and alternating direction algorithms," CAAM Report 20, 46–47 (2009).
26. A. N. Tikhonov and V. Y. Arsenin, "Solutions of ill-posed problems," SIAM Rev. **21**, 266–267 (1979).

Nanosecond compressive fluorescence lifetime microscopy imaging via the RATS method with a direct reconstruction of lifetime maps

JIŘÍ JUNEK[1,2,*] AND KAREL ŽÍDEK[1]

[1]*Regional Center for Special Optics and Optoelectronic Systems TOPTEC, Institute of Plasma Physics of the Czech Academy of Sciences, Za Slovankou 1782/3, 182 00 Prague 8, Czech Republic*
[2]*Technical University in Liberec, Faculty of Mechatronics, Informatics and Interdisciplinary Studies, Studentská 1402/2, 461 17 Liberec, Czech Republic*
**junekj@ipp.cas.cz*

Abstract: The RAndom Temporal Signals (RATS) method has proven to be a useful and versatile method for measuring photoluminescence (PL) dynamics and fluorescence lifetime imaging (FLIM). Here, we present two fundamental development steps in the method. First, we demonstrate that by using random digital laser modulation in RATS, it is possible to implement the measurement of PL dynamics with temporal resolution in units of nanoseconds. Secondly, we propose an alternative approach to evaluating FLIM measurements based on a single-pixel camera experiment. In contrast to the standard evaluation, which requires a lengthy iterative reconstruction of PL maps for each timepoint, here we use a limited set of predetermined PL lifetimes and calculate the amplitude maps corresponding to each lifetime. The alternative approach significantly saves post-processing time and, in addition, in a system with noise present, it shows better stability in terms of the accuracy of the FLIM spectrogram. Besides simulations that confirmed the functionality of the extension, we implemented the new advancements into a microscope optical setup for mapping PL dynamics on the micrometer scale. The presented principles were also verified experimentally by mapping a LuAG:Ce crystal surface.

1. Introduction

Fluorescence lifetime imaging (FLIM) is an important part of spectrometry dealing with photoluminescence (PL) dynamics. It is used mainly in biology [1,2], chemical physics [3,4], as well as in materials engineering [5-8].

There are several methods commonly used for FLIM. The best-known are time-correlated single-photon counting (TCSPC) [9], streak camera [10], gated photon counting [11], and the analog time-domain or frequency-domain technique [12,13]. However, each method has its principle limitations and, as a result, its preferred field of application. In other words, while a given time-resolved method is perfect for a certain use, it may be completely unsuitable for another [14].

Although FLIM has been developed for decades, new concepts which further improve the technique have been reported recently. The main goal is to obtain measurements and evaluations in real time, mainly to investigate biological and medical samples [15,16]. However, real-time FLIM acquisition depends on using pulsed lasers, digitizers, GPUs or 2D arrays of single photon avalanche diodes, which considerably increase the cost of such setups. This holds also for the new FLIM alternatives, such as phasor spectral FLIM (Phasor S-FLIM) [17]. Another competing concept, the analog mean delay method (ADM) [18], can be used for

real-time vivo measurements. Nevertheless, ADM cannot be used to determine the actual shape of PL decay.

Therefore, FLIM research has also developed in the direction of using compressed sensing (CS), where the most typical application is the single-pixel camera (SPC) experiment, which makes the FLIM optical setup more affordable [19]. SPC experiments are very useful in terms of reducing the cost of the experimental setup, but they are typically not suited for real-time in-vivo imaging—both due to the sequential signal acquisition and consequent data retrieval. However, new post-processing approaches for SPC in FLIM are still being developed, e.g., the use of deep learning, which significantly shortens reconstruction time [20]. On the other hand, the neural network needs to be properly trained in order to obtain the required performance over the necessary time range of the investigated lifetimes.

Most of the improvements in CS are applied to standard time-resolved methods and thus still carry their principle limitations. E.g., TCSPC achieves excellent results for nanosecond or sub-nanosecond decays. However, for the measurement of decays on the order of hundreds of nanoseconds (field of material engineering), the method requires a measurement time of hours.

Therefore, it is still essential to continue developing new PL dynamics analysis methods. An example is the RAndom Temporal Signals (RATS) method, which is one of the novel approaches to FLIM. The method is based on the excitation of the measured sample via a randomly fluctuating intensity in time, which makes it possible to fully retrieve the PL decay from a single measured dataset. The RATS and 2D-RATS methods have proven to be valuable, straightforward, and low-cost alternatives to the commonly used FLIM approaches, although their previous implementation had limited their use in real-life experiments.

The initial proof-of-principle measurements of PL decay via RATS were based on a simple generator of a random excitation signal, where we focused a beam on a rotary diffuser and cropped the generated field of speckles with a suitable iris aperture [21]. Such a generator allows for the generation of an analog random excitation in the microsecond and sub-microsecond region, which is well suited for long-lived luminophores or nanoporous silicon [3,22]. However, reaching faster timescales is not realistic in this configuration.

At the same time, employing a diffuser limited the overall efficiency of the excitation laser because only a fraction of the diffused light was used. This fact was even more pronounced in our proof-of-principle implementation of the RATS method in FLIM (2D-RATS), which demonstrated that it is possible to map PL dynamics via an optical setup based on two diffusers [23].

Finally, the initially used post-processing consists of the reconstruction of PL maps at each delay after excitation and subsequent fitting to obtain a lifetime in a given image pixel. This procedure is highly computationally costly.

This article provides an overview of a new implementation of the 2D-RATS, i.e., the FLIM experiment, which overcomes all the above-stated shortcomings. This was enabled by three fundamental modifications in the RATS experiment. In particular, we introduced a new digital mode of random intensity fluctuation by using direct laser modulation. Fast laser modulation enabled us to reach the temporal resolution in the PL decay measurement of 6 ns. Secondly, using a digital micromirror device (DMD) to invoke random spatial masks, we gained incomparably higher efficiency reaching values a hundred times higher compared to the proof-of-principle experiments [23].

Finally, we propose a novel approach to PL data analysis where we first identify the significant PL lifetime components. An amplitude map of each component is subsequently computationally extracted. Therefore, a typical analysis—a bi-exponential fit of 35×35 map with a compression ratio of 0.4 and 100 timepoints of PL decay—leads to post-processing times about 10-times shorter compared to the approach used in our previous work [23].

Overall, the presented implementation shifts the abilities of the 2D-RATS method to a different level, which we demonstrate in both the synthetic and experimental data. The ability to retrieve PL dynamics on the scale of tens of nanoseconds in combination with the ability to cover long-lived PL decay make the method very useful in the field of material engineering [7,8]. At the same time, the current implementation remains a low-cost solution compared to standard FLIM setups.

2. Overview of the RATS method

2.1 0D-RATS

As mentioned in the introduction, the principle of the method is to excite the measured sample with a random excitation signal I_{EXC}. The generated photoluminescent I_{PL} signal, which is a convolution of the excitation signal and the PL decay of the measured sample I_D, also has a random character as a result of the random excitation:

$$I_{PL} = I_{EXC} * I_D. \tag{1}$$

The PL decay I_D curve can be calculated by using deconvolution. In the presented results, the Tikhonov regularization was applied to avoid ill-conditioned problems [24]:

$$I_D = Re\left\{\mathbb{F}^{-1}\left[\frac{\mathbb{F}\left(I_{PL}\right)\,\mathbb{F}^{*}\left(I_{EXC}\right)}{\mathbb{F}\left(I_{EXC}\right)\mathbb{F}^{*}\left(I_{EXC}\right)+\varepsilon\overline{\mathbb{F}\left(I_{EXC}\right)\mathbb{F}^{*}\left(I_{EXC}\right)}}\right]\right\}. \tag{2}$$

Moreover, the Tikhonov regularization parameter ε can also be used to suppress the noise effect of the system [25]. More details about a single-point measurement approach (0D-RATS) can also be found in our previous works [21, 23].

2.2 2D-RATS

In the case of 2D measurements, a straightforward option is to use the 0D-RATS method in raster mode, which can be very effective, for example, using a mirror with a Micro Electro Mechanical System (MEMS) [26]. Nevertheless, the use of compressive sampling in the configuration of the single-pixel camera ensures the acquisition of the desired dataset by a lower number of measurements compared to the raster mode, where the number of measurements corresponds to the number of pixels of an image [27].

The principle of the so-called 2D-RATS measurement consists in illuminating the scene with a set of M random masks of N pixels, where the ratio M/N indicates the compression ratio k [23]. The individual masks have a random character in space, and their intensity varies in time according to I_{EXC}—see Fig. 1(A). The randomness of the mask ensures that a different n illuminated segment of the sample is excited in each measurement. Therefore, Eq. (1) can be rewritten to the sum of the PL from each segment:

$$I_{PL} = \sum_{i=1}^{n} I_{PL}\left(i\right) = I_{EXC} * \sum_{i=1}^{n} I_D\left(i\right). \tag{3}$$

As a result, we always attain a unique I_{PL} for each of the M masks. By using the I_{PL} dataset, it is possible to reconstruct the individual I_{DA} decay curves corresponding to the given mask:

$$I_{DA} = Re\left\{\mathbb{F}^{-1}\left[\frac{\mathbb{F}\left(\sum_{i=1}^{n} I_{PL(i)}\right)\mathbb{F}^{*}\left(I_{Exc}\right)}{\mathbb{F}\left(I_{Exc}\right)\mathbb{F}^{*}\left(I_{Exc}\right)+\varepsilon\overline{\mathbb{F}\left(I_{Exc}\right)\mathbb{F}^{*}\left(I_{Exc}\right)}}\right]\right\}. \tag{4}$$

Thus, each random mask is represented by one I_{DA}.

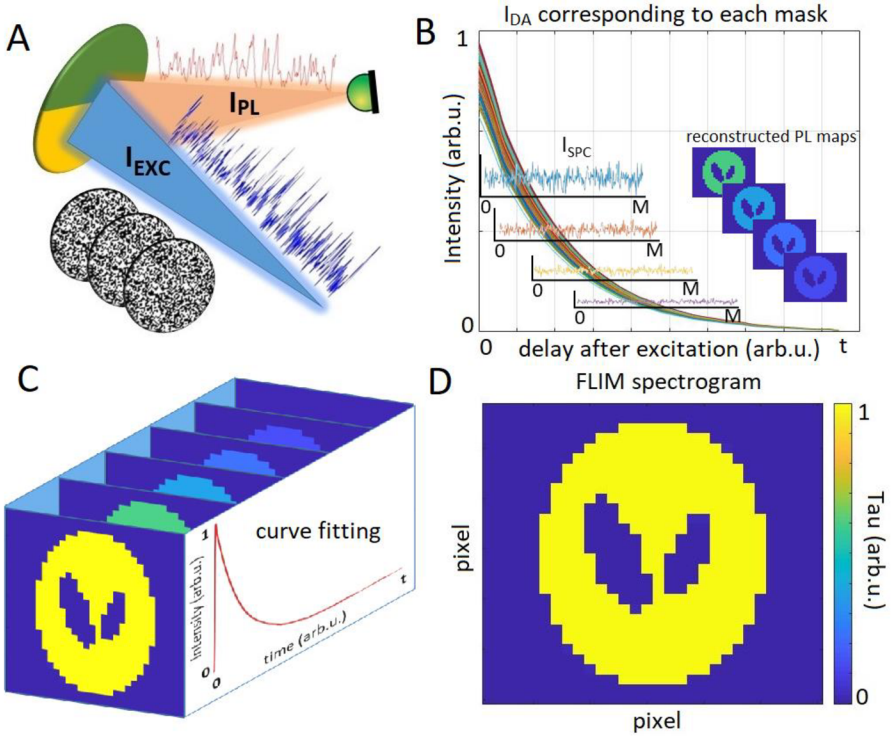

Fig. 1. (A) Scheme of principles of the 2D-RATS method. The sample is illuminated with masks following a temporal fluctuation of excitation signal I_{EXC}, which generate the corresponding PL signal I_{PL}. (B) Set of calculated I_{DA} (solid lines in the main graph) corresponding to the set of masks can be recalculated into the I_{SPC} signals (inset graphs for several delays t). By using Eq. (5) we attain the corresponding reconstructions of the PL maps. (C) Scheme of a 3D datacube of reconstructed PL maps and indicated fitting. (D) Example of a final FLIM spectrogram as a map of PL lifetimes.

The measured set of I_{DA} curves then needs to be converted into the temporal slides of PL decay. To do this, we need to determine the PL intensity I_{SPC} at a selected delay for all masks—see Fig. 1(B). The I_{SPC} dataset is simply extracted from the I_{DA} curves for the studied delay after excitation t. By using the knowledge of the random masks and the I_{SPC}, the PL map for each delay after excitation $m(x,y,t)$ can be determined using standard compressed sensing algorithms employed for the single-pixel camera experiment. We aim at solving an undetermined system using Eq. (5), where the set of vectorized masks is stated as B and TV is stated for total variation and the PL map for a given delay after excitation is declared just as $m(x', t)$ because it is vectorized:

$$min\left\{\left\|Bm(x',t)-I_{SPC}\right\|_2^2+TV(m(x',t))\right\}. \tag{5}$$

The presented approach uses a well-established image retrieval procedure from the single-pixel camera experiment. A significant drawback is that this approach requires reconstructing PL maps for all delays after excitation and creating a 3D datacube to obtain complete information—see Fig. 1(C). This implies carrying out typically tens of iterative solutions of Eq. (5), which is computationally very costly. Finally, to attain the FLIM spectrogram (Fig. 1(D)), it is necessary to fit the third dimension (temporal dependence) of the 3D datacube in each pixel with a suitable function—typically a multi-exponential fit—and determine the lifetime τ. For better understanding, refer to Fig. 1, which summarizes the whole procedure.

Compared to standard FLIM approaches, such as TCSPC or gated photon counting, 2D-RATS provides very robust PL retrieval, where the only parameter to be kept in mind is to

ensure is that the setup has a sufficiently low width of the impulse response function (IRF) compared to the measured lifetimes, i.e., a sufficiently fast random signal. In contrast, the suitability of the setting parameters in TCSPC must be checked with respect to the repetition rate of excitation pulses or PL intensity. In the case of using gated photon counting, the user should choose the appropriate number of gates, length of gate, and other parameters.

3. Digital RATS modulation with direct PL lifetime map reconstruction

3.1 Digital random signal generation

The previously published proof-of-principle RATS experiment was based on generating a random excitation pattern by using a rotary diffuser. This leads to a rapidly fluctuating signal, which we denote as a random analog signal, as the light intensity continuously randomly varies in time. While this approach is useful owing to its simplicity and negligible cost, it limits the use of the RATS setup with respect to the reachable temporal resolution.

Therefore, we implemented an advanced mode of random signal generation with higher efficiency by using a modulated laser. One of the lasers that makes this possible is the Cobolt S06-01 (405 nm), which can be modulated digitally up to 150 MHz in a random fashion. The result is a rectangular signal with a randomly distributed duty cycle, which we denote as a random digital modulation.

We compare the digital and analog generation of a random signal in 0D-RATS on simulated data, while the experimental demonstration can be found in Section 4. An example of a simulated digital signal can be seen in Fig. 2 (upper left panel), where the character of the signal is more apparent in a zoomed part of the signal from 0 to 0.5 ms (see inset).

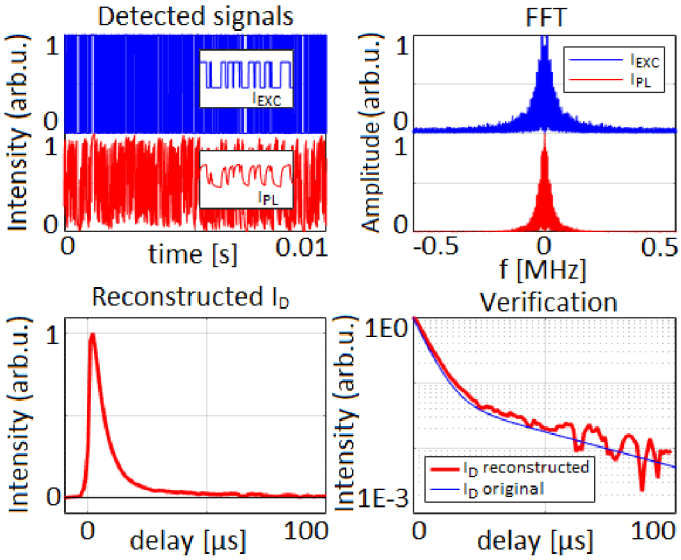

Fig. 2. Simulated measurement of bi-exponential I_D with parameters $A_1 = 1$, $A_2 = 15$, $\tau_1 = 40$ µs, and $\tau_2 = 5$ µs using digital random signal with $IRF_D = 1.45$ µs. Upper left panel: excitation (blue line) and PL (red line) signal in time; upper right panel: amplitudes of Fourier components in excitation (blue line) and PL (red line); lower left panel: retrieved PL decay curve in a linear scale; lower right panel: retrieved PL decay (red line) compared to the original decay (blue line) in a semilogarithmic scale.

Fig. 2 also shows a simulated measurement of bi-exponential PL decay I_D (see Eq. (6)) using the aforementioned modulated I_{EXC} with a random distribution of duty cycle (random digital signal).

$$I_D = A_1 e^{-t/\tau_1} + A_2 e^{-t/\tau_2}. \quad (6)$$

Fig. 2, which shows the digital modulation, can be directly compared with Fig. 3, which presents the simulated measurement of the same bi-exponential PL decay I_D using a random analog I_{EXC} signal. In both figures, the parameters of the used bi-exponential I_D were $A_1 = 1$, $A_2 = 15$, $\tau_1 = 40$ µs and $\tau_2 = 5$ µs. Impulse response function (IRF) for random digital signal was $IRF_D = 1.45$ µs and for random analog signal it was $IRF_A = 2.07$ µs.

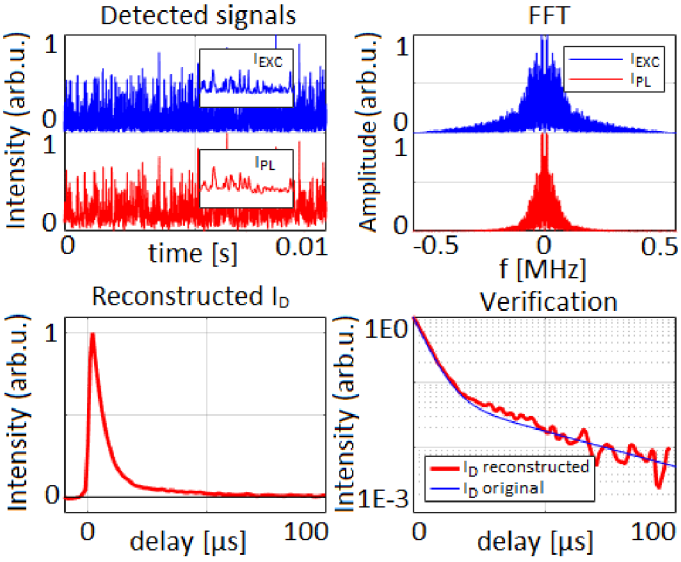

Fig. 3. Simulated measurement of bi-exponential I_D with parameters $A_1 = 1$, $A_2 = 15$, $\tau_1 = 40$ µs and $\tau_2 = 5$ µs using analog random signal with $IRF_A = 2.07$ µs. Upper left panel: excitation (blue line) and PL (red line) signal in time; upper right panel: amplitudes of Fourier components in excitation (blue line) and PL (red line); lower left panel: retrieved PL decay curve in a linear scale; lower right panel: retrieved PL decay (red line) compared to the original decay (blue line) in a semilogarithmic scale.

By comparing the simulated PL decay retrieval for the digital and analog modulation, we can conclude, in agreement with our expectations, that both the approaches lead to identical PL decay. Therefore, digital modulation of excitation intensity can be used without losing the credibility of the retrieved PL decay. Although the spectrum of a digital signal features a narrower central peak in the Fourier space, it has higher amplitudes for higher frequencies. Therefore, the digital signal reaches a lower IRF width compared to the analog one.

We present the experimental confirmation of the agreement in Section 4. It is worth noting that the applicability of the analog modulation approach had been previously verified with a streak camera or TCSPC [21,23].

3.2 Direct PL lifetime map reconstruction

The original approach to PL lifetime imaging (FLIM) was based on the retrieval of a PL map for each delay after excitation, as it is introduced in Section 2.2. The real-life measurements showed that this procedure makes the post-processing routine highly time-consuming. Therefore, we propose an alternative approach that allows determining the FLIM spectrogram solely from the number of reconstructions, which equals the expected number of lifetimes in the measured sample. Namely, by determining a set of viable PL lifetimes in the sample, we can mathematically reconstruct the amplitude maps directly for the given lifetime τ. This

approach is highly beneficial for samples with a set of PL markers, mapping samples with distinct defects, or color centers emitting with well-defined lifetime.

In the cases where we know a priori the present lifetimes in a sample—for instance, a sample with a set of PL markers [28]—we can directly use this knowledge. However, in the opposite case, it is necessary to take the so-called zeroth step, i.e., illuminate the entire measured area of a sample with a homogeneous excitation spot and determine the PL decay curve I_{DA0} representing the whole sample, using Eq. (4). The I_{DA0} curve can be used to extract all present lifetimes via fitting. Since the entire spectrum of lifetimes is obtained from the zeroth step, it is then sufficient to fit only amplitudes of each lifetime during the I_{DA} investigation (see text below). The literature states that it is appropriate to assume the fitting with a bi-exponential or tri-exponential decay [14]. Thus, we tested the novel principle of post-processing for bi-exponential decay (see Eq. (6)).

The direct PL lifetime map reconstruction is based on the single-pixel camera concept. Therefore, it can be used the same measurement routine. The measured sample was illuminated with random patterns (masks), which follow the temporal fluctuation of intensity according to I_{EXC}. The I_{DA} corresponding to each mask was reconstructed according to Eq. (4). The obtained I_{DA} curves were then fitted with a multi-exponential function with a fixed set of lifetimes. The fitting provided us with the amplitudes corresponding to the individual lifetimes.

If we consider the bi-exponential decay curve of the sample (see Eq. (6)), we obtain the parameters τ_1 and τ_2 from the fitted I_{DA0}. We assume the presence of τ_1, τ_2 in all measured I_{DA} curves and, therefore, we only fit parameters A_1 and A_2 of all I_{DA} curves. Because the sample is illuminated by the number of masks M (given by the compression ratio k), we also get M different values of A_1 and A_2, which creates vectors A_1SPC, A_2SPC of size M. Since the amplitudes A_1 and A_2 are a linear superposition of all PL decays within the illuminated area of the sample, we can employ the same retrieval algorithms as we use for the PL intensity map.

The knowledge of the used masks and A_1SPC, A_2SPC vectors can be used to reconstruct amplitude maps using Eq. (7). In this case of bi-exponential decay, we obtain two amplitude maps of lifetime $H\tau_1$ and $H\tau_2$.

$$min\left\{\left\|BH_{\tau n}-A_nSPC\right\|_2^2+TV(H_{\tau n})\right\}. \tag{7}$$

In the case of monoexponential decay, the reconstructed map H_τ represents the amplitude distribution for a given τ. Nevertheless, if it is an n-exponential decay, the lifetime τ in each pixel (FLIM spectrogram) must be determined. There are multiple approaches to calculating the overall decay lifetime of a complex PL decay curve. Here we consistently used the weighted average:

$$\tau(x,y)=\frac{\sum_{i=1}^{n}H_{\tau i}\tau_i}{\sum_{i=1}^{n}H_{\tau i}}. \tag{8}$$

The process of amplitude map retrieval is described in more detail in a scheme assuming the bi-exponential decay (τ_1 = 20 ns, τ_2 = 70 ns), as shown in Fig. 4. Amplitude distribution of τ_1 can be observed in $H\tau_1$ map, and amplitude distribution of τ_2 is shown in $H\tau_2$ map. Using Eq. (8) we calculated the total FLIM spectrogram with the mean lifetime.

The proposed approach significantly accelerated the post-processing procedure, and the whole FLIM spectrogram can be determined using n reconstructions for n-exponential decay. Thus, in the case of bi-exponential decay, there are only two reconstructions of the undetermined system. Moreover, this approach offers excellent resistance to noise in the measured data, as shown in the next subsection.

Due to its principles, the presented direct lifetime retrieval is more suited for materials with several emitting species with sharp PL lifetime values, where the contribution of each species

varies over the scene. In such a case, the method outperforms the standard approach, as we will show later. In the case where each pixel of the scene features a different lifetime value from a broad distribution, the method can still attain reasonable results by including more lifetimes and calculating the mean PL lifetime according to Eq. (8). Nevertheless, for a very broad lifetime distribution, using the standard frame-by-frame retrieval can be considered as a better option.

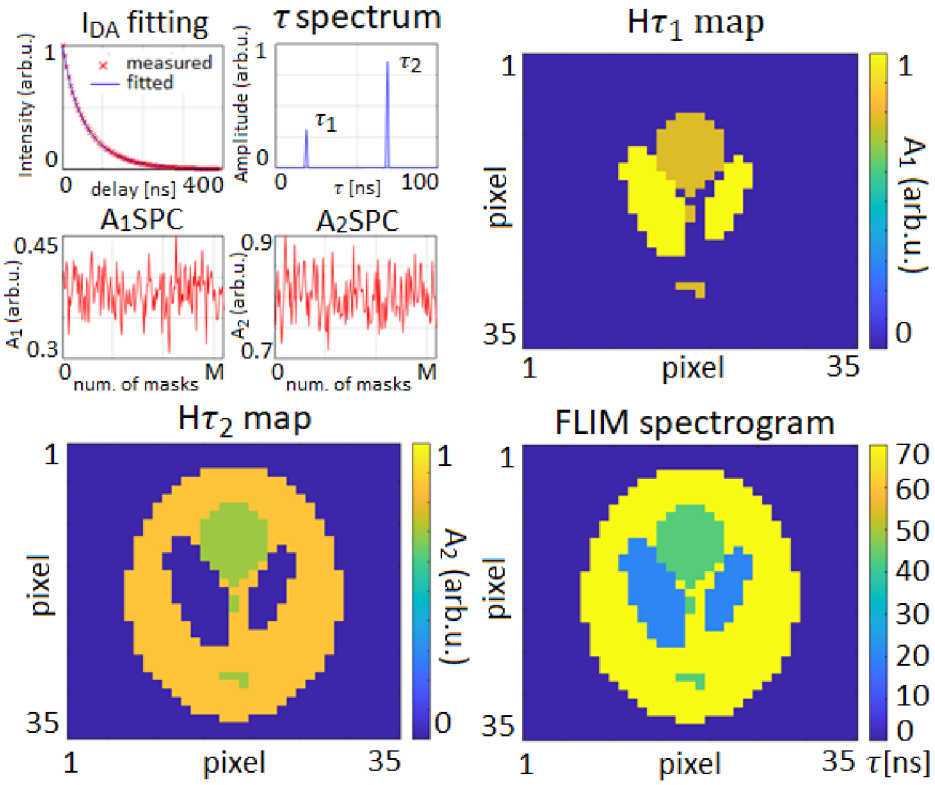

Fig. 4. (A) Example of fitting I_{DA} curve amplitudes A_1 and A_2, where the distribution of τ_1 and τ_2 is already known from I_{DA0} fitting. The amplitude fitting provides vectors A_1SPC and A_2SPC. (B) Reconstructed amplitude map $H\tau_1$. (C) Reconstructed amplitude map $H\tau_2$. (D) Calculated FLIM spectrogram based of knowledge of $H\tau_1$ and $H\tau_2$.

3.3 The comparison of noise effect on both post-processing approaches

The new approach to the FLIM spectrogram evaluation introduced in Section 3.2 significantly reduces the time required for post-processing compared to the original approach described in Section 2.2. In this section, we compare both approaches with respect to the quality of the obtained FLIM spectrogram with different levels of noise present in the measured data.

In our previous work, we showed that the quality of the retrieved I_{DA} and the 2D scene reconstruction is significantly more affected by the noise level present in I_{PL} compared to the I_{EXC}. Furthermore, it was shown that the quality of 2D scene reconstruction is negligibly affected by the change in compression ratio compared to the amount of noise in the system [25]. Therefore, for the following simulations, the compression ratio was always kept at k = 0.4, and we tested only the noise present in the PL signal I_{PL}, which we set to 0%, 0.5%, 1%, and 1.5%, respectively. The I_{EXC} signal was kept noiseless. The resulting FLIM spectrogram of lifetimes F was always compared with the ground truth U to extract the percentage error of the reconstructed image R:

$$R = \frac{\sum \sqrt{(F-U)^2}}{\sum \sqrt{U^2}} \cdot 100. \tag{9}$$

The spectrograms obtained by the original approach described in Section 2.2 are labeled as $FLIM_B$, while the spectrograms obtained by the new, proposed approach are labeled as $FLIM_A$. The simulation results are summarized in Fig. 5, where the individual row represents the different noise levels in the I_{PL} signal, while the columns indicate gradually the $H\tau_1$, $H\tau_2$, $FLIM_A$ and compare them to the $FLIM_B$. The dependence of the error R on the noise level is then provided in Fig. 6.

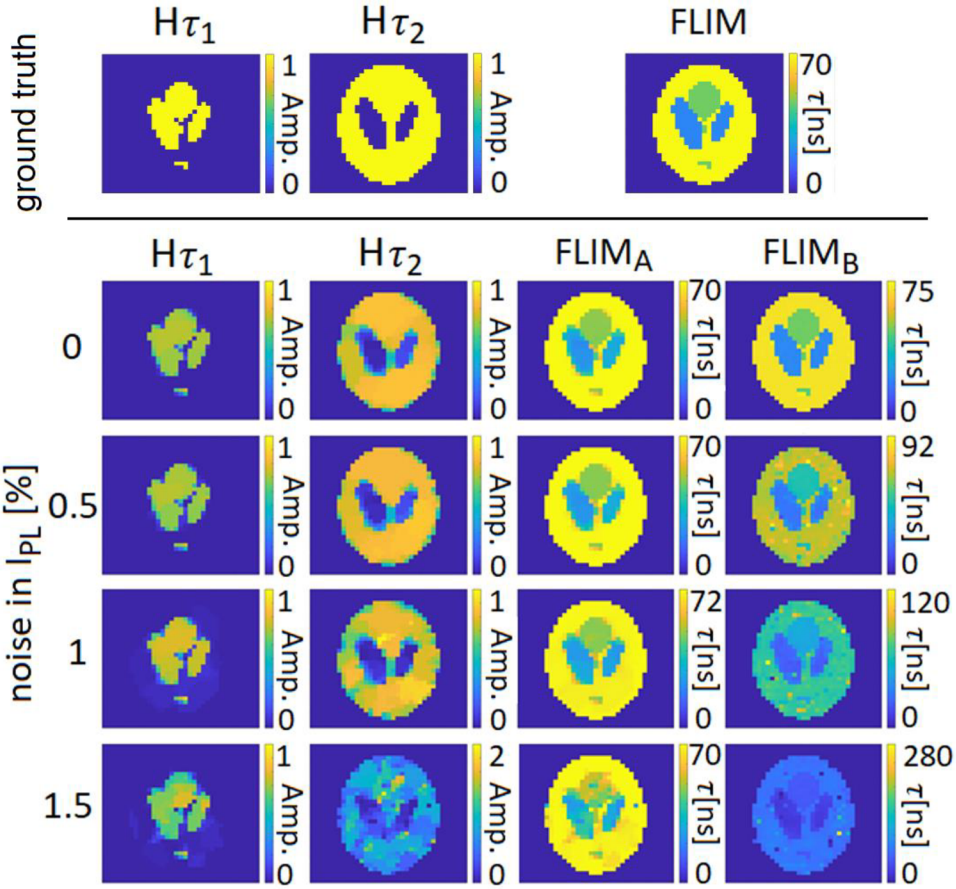

Fig. 5. Above the line is the ground truth, which can be compared to the simulated results below the line. The results of simulations of noise effect on both post-processing approaches. The new approach, represented through $FLIM_A$ (the third column), is supplemented by reconstructions of partial amplitude maps $H\tau_1$ (the first column) and $H\tau_2$ (the second column). The results of the original approach are represented through $FLIM_B$ (the fourth column). Each row corresponds to chosen noise level in the system (0-1.5%).

For this simulation, a scene with two areas τ_1 = 20 ns and τ_2 = 70 ns and corresponding amplitudes A_1 = 1 and A_2 = 1 was employed. The "sample" combines parts with a mono-exponential decay with a region featuring a bi-exponential decay.

The TVAL3 algorithm was used to reconstruct the undetermined systems in Eq. (7) [29,30]. In the case of $FLIM_B$, it was the intensity PL maps reconstruction, where the main parameters

of the algorithm were *mu* (2^{11}) and *beta* (2^7). In the case of $FLIM_A$, amplitude maps reconstruction was used, where the main parameters were set to *mu* (2^9), and *beta* (2^6). The mentioned parameters *mu* and *beta* were optimized for both approaches independently to attain the best reconstruction results with the lowest residues.

Reconstructed pixels that were below 10% of the PL amplitude were removed from the statistics for both $FLIM_A$ and $FLIM_B$ in Fig. 5 and also in Fig. 6. The fitting curves for both $FLIM_A$ (I_{DA}'s) and $FLIM_B$ (3D-datacube) cases were always in the range of 0 ns to 400 ns, which is sufficient for the entered parameters τ_1 and τ_2.

For a rigorous discussion of results, it is important to realize that the $FLIM_B$ results (original approach) are dominantly affected by noise in I_{SPC} (see Fig. 1(B)). This noise arises from inaccuracies in the reconstruction of individual PL maps $m(x,y,t)$ when creating a 3D datacube (see Fig.1(C)). Due to the character of the image retrieval, the noisy data entering the fit can cause a vast local error of the PL lifetime value in a few pixels. Therefore, $FLIM_B$ spectrograms could deviate from the ground truth values locally, while the overall agreement might be kept.

On the contrary, the $FLIM_A$ approach could introduce an error already in the zeroth-step of the process, when the whole sample is homogeneously illuminated, and the set of lifetimes contained in the sample is analyzed via I_{DA0} fitting. The obtained lifetimes from the zeroth step are further considered during the remaining I_{DA} evaluation, where they are used to calculate the mean PL lifetime via amplitudes A_1 and A_2. Since the amplitude maps are calculated from an undetermined system with the condition of a low total image variation, we attained smooth images without local errors despite the present noise. On the other hand, the error of the initial lifetime fit propagates to the final FLIM spectrogram. Therefore, in our simulations, the reconstruction of 0% noise in the system, $FLIM_B$ (original FLIM analysis) has higher accuracy than $FLIM_A$. However, in a situation with a PL noise of 0.5% and higher, $FLIM_A$ is more accurate than $FLIM_B$ (see Fig.6).

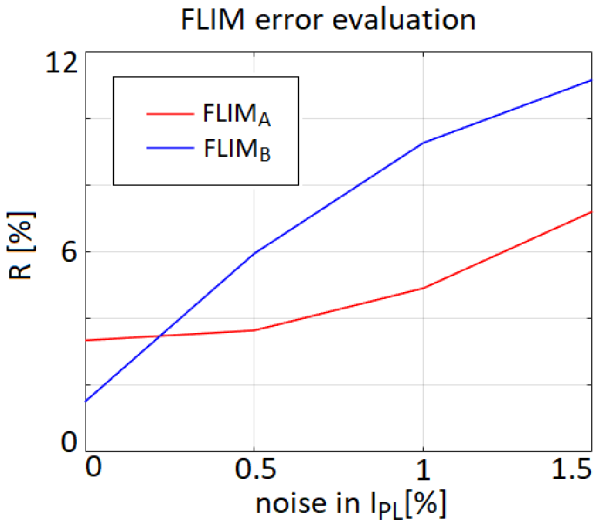

Fig. 6. Evaluation of FLIM spectrogram reconstruction error – see Eq. (9) - via $FLIM_A$ (direct PL lifetime map) and $FLIM_B$ (frame-by-frame standard analysis) approach for a different amount of noise in a system (I_{PL} signal).

Although it may seem that an imprecise fit of PL lifetimes in the zeroth step will highly affect the $FLIM_A$ results, our tests proved that this effect is not pronounced. We summarized in Table 1 all the obtained lifetimes after the zeroth step (I_{DA0} fitting), which all suffer from the inevitable fitting error. Nevertheless, the total error of the $FLIM_A$ spectrograms—see Fig. 6—increases with the noise in the fitted data and does not follow the lifetime errors. As an example,

the worst zeroth-step lifetime fit is associated with the noise of 1% in the system (see Table 1), while the highest total reconstruction error is linked to the data with the noise of 1.5% (see Fig.6). To outline the fitting issue, we present results obtained after a single I_{DA0} trace fitting. However, the imprecise determination of lifetimes can be improved by statistical averaging over several measurements in the zeroth step.

Table 1. Summary of results of I_{DA0} fitting in zeroth step of $FLIM_A$ determination process.

Noise in I_{PL} signal [%]	τ_1 [ns]	τ_2 [ns]
0	21	70
0.5	21	70
1	24	72
1.5	22	70

Overall, it can be stated that the direct PL lifetime map reconstruction ($FLIM_A$) is more stable in terms of noise. The standard frame-by-frame retrieval ($FLIM_B$) may be locally accurate, while some pixels may be entirely out of scale, and it is not easy to determine whether this is an effect of the noise of an actual sample property.

It is beneficial to address new methods for accurately determining the parameters of exponential curves [31], which would further improve the quality of both considered approaches. Nevertheless, the novel presented approach is less time-consuming in post-processing than the standard one.

4. Experimental implementation

4.1 Optical setup

The advanced optical setup stemmed from the original proof-of-principle experiments [23]. Its scheme is shown in Fig. 7.

Temporal modulation was ensured via modulated Cobolt laser S06-01 MLD (405nm). The modulation signal was produced by the Digilent Cmod A7 development kit and was generated in the FPGA Xilinx Artix-7 (VIVADO software package). The bitstream is generated via Linear Feedback Shift Register (LFSR) from flip-flops and XNOR gate feedback, configured in FPGA. The output of the LFSR meets many randomness tests [32]. Using the above-mentioned configuration, one can generate any bitstream with the desired repetition period of the random signal. Thus, it is possible to choose as long a period as necessary for one measurement and thus avoid the effect of I_{EXC} periodicity described in our previous work [25].

A temporally modulated laser beam is expanded using a GBE20-A Thorlabs beam expander and guided to the digital micromirror device (DMD) through mirrors M_1 and M_2 so that one of the reflected beams is reflected in the normal direction of the DMD chip surface. In order to achieve an even distribution of the DMD-generated illumination pattern, the laser beam diameter is magnified 20 times in front of the DMD, so it significantly exceeds the dimensions of the DMD chip.

The DLPLCR65EVM DMD from Texas Instruments was controlled via a DLPLCRC900EVM module. We used 35×35 pixel patterns both in the simulations (Section 3) and in the demonstration measurements (Section 4). However, rather than the entire DMD chip size, only a limited part of the chip in its center was used to generate patterns. This enabled us to use a low numerical aperture within the setup.

Because the DMD pixel size is in the micrometer scale (7.56 μm), diffraction on the pixels should be considered [33,34]. Therefore, the diffracted beam from the DMD is collected with

an AR-coated fused silica lens L_1 (Ø50mm, f = 75 mm) and then filtered using a low pass filter in the configuration of L_1 and the second AR-coated fused silica lens L_2 (Ø25mm, f = 50 mm) and iris aperture. Hence, only one diffraction order passes through the low pass filter and hits the Thorlabs N-BK7 beam splitter BS (CM1-BS013 (50:50)). The reflected part of the beam is targeted on a PDA10A2 photodiode for I_{EXC} detection, while the transmitted part of the beam goes through a 405 nm bandpass filter F_1 (Thorlabs FBH405-10) to avoid possible parasite I_{PL} generation in N-BK7 glass (BS).

Subsequently, the beam is transmitted through a dichroic mirror DM (Thorlabs DMSP425, 425 nm cut-off) and imaged by a microscope objective—4X Olympus plan achromat objective (0.10 NA, 18.5 mm WD). Using the 4X Olympus plan achromat lens, we ideally get a single pixel size of 12.6 µm and a field of view of about 450x450 µm. The stated values were confirmed with calibration grids with a defined line spacing of 50 µm.

The illumination pattern imaged by a microscopic lens on a sample can be captured using a CMOS camera (IDS UI-3240ML-M-GL) to find the optimal focus. The microscopic lens also collects the generated I_{PL} signal, which is reflected and focused on a photomultiplier (Hamamatsu H10721-20) through a dichroic mirror and lens L_3 (Ø25mm, f = 12 mm). Prior to PL detection, the collected light is filtered by the Thorlabs 500 nm cut-off filter F_2 (FELH0500) to avoid a possible back reflection of I_{EXC}. Thus, all decay curves correspond to PL in a range above 500 nm of wavelength.

The temporal waveforms of both the I_{EXC} and the I_{PL} signals are collected by using the TiePie Handyscope HS6-1000XM. The impulse response function (IRF) depends on the modulation frequency and many additional parameters and we provide IRF width for each experiment.

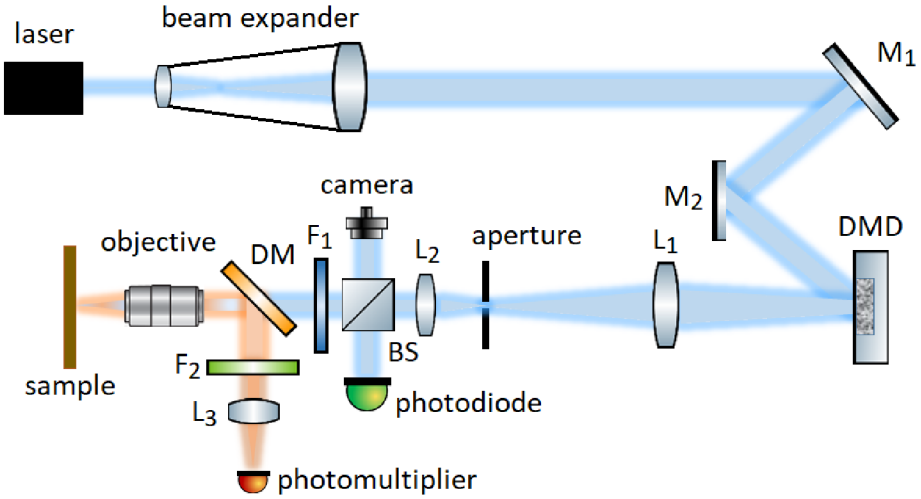

Fig. 7. The 2D-RATS method in a single-pixel camera configuration implemented into a microscope optical setup.

In the current configuration, where we used a cw-operated laser at 125 mW, we attained an intensity of the excitation light of 0.35 mW at the sample plane. This means that the setup efficiency was about 0.3%. Note that the use of excitation laser efficiency was not optimized, and it was highly affected by using an excessive beam diameter at the DMD, the use of a part of the DMD chip, selection of a single diffraction order, or beam splitter ratio—these parameters can be tuned to improve efficiency. Yet, we reached efficiency a hundred times higher compared to the proof-of-principle diffusor-based 2D RATS setup (efficiency of about 0.003%) [23].

4.2 Digital and analog modulation of the excitation signal

By comparing the simulated PL decay retrieval for the digital and analog modulation in Section 3.1, we concluded, in agreement with our expectations, that both the approaches lead to identical PL decay. We used the new optical setup to carry out the same comparison experimentally.

Both approaches (analog vs. digital random I_{EXC}) were compared in a single-point measurement (0D-RATS) configuration, where the SCHOTT OG565 absorption filter was used as a test sample. The setup described in this article was used for the digital excitation modulation, while the proof-of-principle setup was employed for the analog excitation modulation [21]. For the analog modulation, we reached an improved analog modulation speed by tightly focusing an expanded excitation beam (f = 25 mm, spot size 2.5 µm) on a fine diffusor produced with SiC1200 abrasives. Both the beam distance from the diffuser center of 115 mm and the rotation speed of 100 Hz contributed to the fast modulation. Therefore, the IRF width for the analog case was w_A = 71 ns. The digital modulation was adjusted to reach a similar IRF width of w_D = 47 ns.

To gain a rigorous comparison, the I^0_D curve obtained using the random digital signal was convolved with the Gaussian function $G(w)$ with a FWHM w equal to the root mean square difference of w_A and w_D values:

$$I_D = I_D^0 * G\left(\sqrt{w_A^2 - w_D^2}\right). \tag{10}$$

The experimental results in a semilogarithmic representation are presented in Fig. 8. They confirmed that the digital and analog modulation of the signal can be equally employed in the PL decay analysis and lead to the same decay functions.

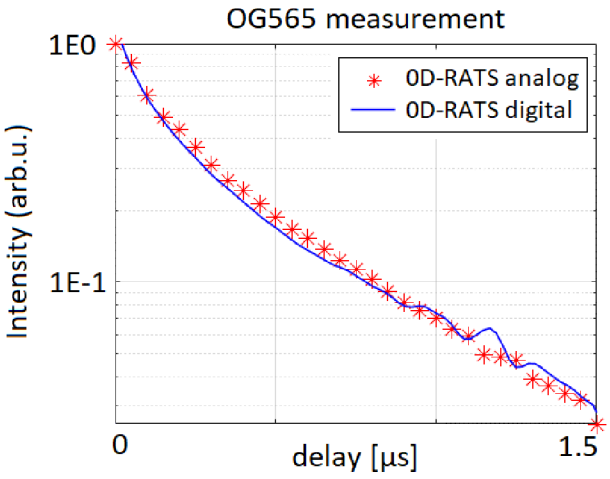

Fig. 8. Comparation measurement of OG565 filter using analog and digital random I_{EXC} with w_A =71 ns and w_D = 47 ns.

4.3 Temporal resolution of digital modulation of the excitation signal

By using the thorough optimization of the diffuser-based intensity modulation, we reached the IRF width of 71 ns, as stated before. Now, we will turn to show the potential of digital modulation using the Cobolt S06-01 laser. Here, we tested the variation of both the laser modulation frequency and the sampling rate—see Fig. 9. We can see that the fastest combination leads to the IRF width of 6 ns, which is an order of magnitude below the optimized diffuser-based modulation.

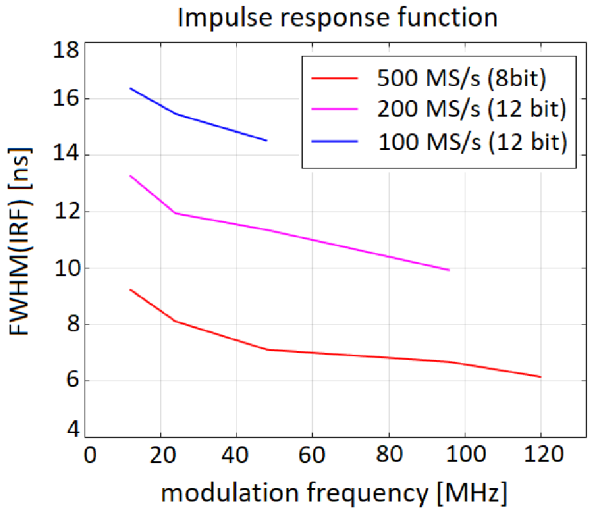

Fig. 9. IRF measurement for different modulation frequencies and different sampling frequencies.

That is primarily due to the laser parameters, especially modulation. Hence, it is easy to generate a much faster random signal than using our previously described rotary diffuser-based generator [21]. Apart from this, a prominent feature in Fig. 9 is that the IRF width does not strongly depend on the modulation frequency. This behaviour is the consequence of the rectangular character of the digital signal. From the general principles of rectangular signal generation, the signal contains rapidly rising and falling edges carrying significantly higher frequencies than the set modulation frequency of the digital signal. These frequencies would be revealed with sufficient sampling and bandwidth. Therefore, ideally, a digitizer with significantly faster sampling and a broader bandwidth should be used for such a (i.e., modulated) signal.

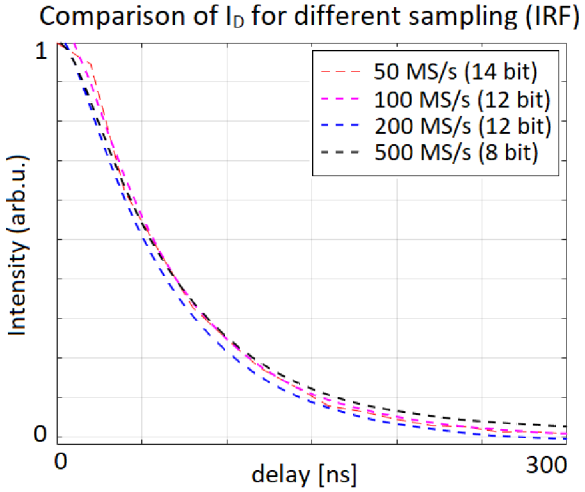

Fig. 10. Comparison of I_D measured on LuAG:Ce for different sampling frequencies (different IRF width). Measurements with lower IRF width were convolved with the root square deviation of IRF width related to measurements with the highest IRF width.

The employed HS6-1000XM TiePie USB-handyscope allows sampling of up to 500 MSa/s with a bandwidth of 250 MHz when scanning on two channels simultaneously. Hence the

Nyquist condition for the fastest bit carrier frequency was met, but the frequencies of leading and trailing edges were truncated. As a result, the IRF width strongly depends on the sampling rate, as shown in Fig. 9.

However, since the carrier frequencies are not truncated, no aliasing occurs, and thus the resulting I_D reconstruction is not distorted. To confirm this statement, we plot in Fig. 10 PL decay of the LuAG:Ce luminophore for various sampling options. As in Fig. 9, each measurement was convolved with a Gaussian function to match the largest IRF width within the measurements. This allows for a direct comparison of the curves. We did not observe any notable variation in the decay curves and corresponding PL lifetime for the sampling rates well above the PL decay rates.

In total, a RATS setup with digital signal modulation, which is not limited by the bandwidth of the detector and the corresponding electronics, has the ultimate resolution due to the steepness of the rectangular laser signal edge and the sampling rate.

4.4 Demonstration measurement

The 2D-RATS experiment based on the advancements presented in Section 3.2 was experimentally implemented into a microscope setup based on a single-pixel camera configuration. The technical details of the setup are described in Section 4.1. Here we provide an example of data acquired by the advanced setup and data processing.

We selected a LuAG:Ce scintillation crystal as a test sample [35], which features strong PL emission. The test sample was a thin monocrystal plate polished on both sides with visible, microscopic scratches and cracks. One of the cracks was selected as the testing spot since we expected a significant increase in PL intensity at the defect. The PL intensity is higher due to high scattering, which improves PL signal outcoupling from the sample.

A 4X Olympus plan achromat objective (0.10 NA, 18.5 mm WD) was used to map the testing area of 450×450 μm with a pixel size of 12.6 μm (35×35 pixels). The compression ratio was set to k = 0.4 (490 measurements) with a single PL decay dataset measured over 10 ms. However, the current total acquisition time in the order of tens of minutes was caused dominantly by the data transfer and data handling, which can be significantly optimized. The sampling frequency was 200 MHz and the modulation frequency of the fastest bit of the random signal reached 98 MHz, which resulted in IRF width of 9.9 ns.

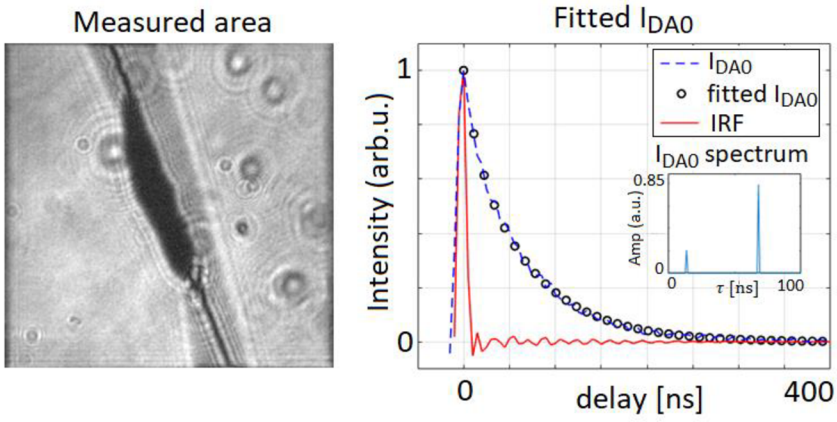

Fig. 11. Left panel: Measured area of the LuAG:Ce crystal. Right panel: Corresponding I_{DA0} with fitted bi-exponential curve and revealed spectrum of the τ_1 and τ_2.

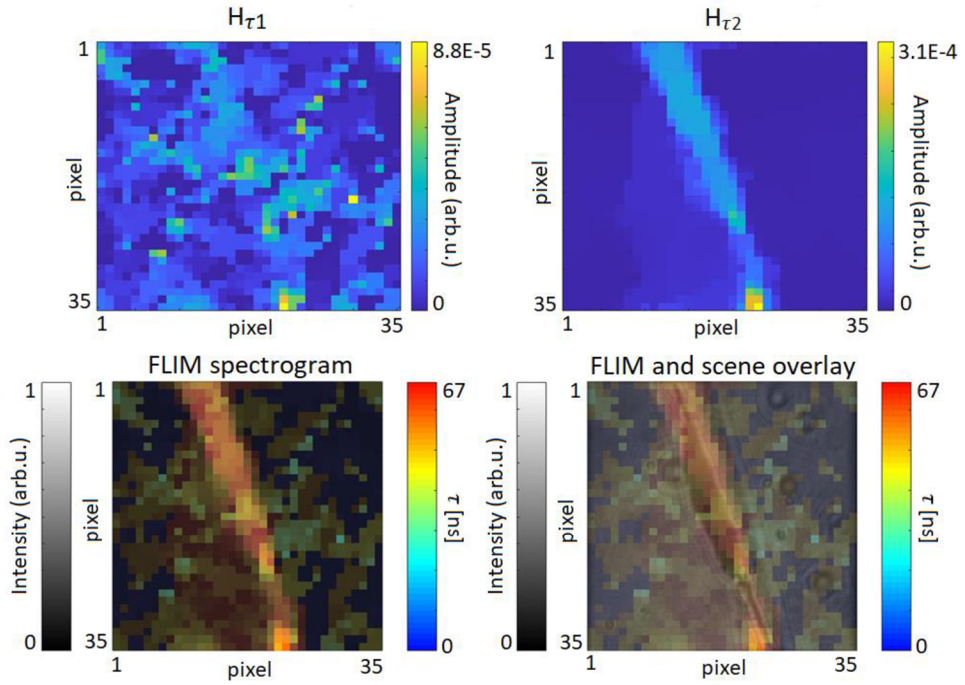

Fig. 12. Upper panels: Reconstruction of $H\tau_1$ and $H\tau_2$ areas corresponding to expected lifetimes. Lower panels: FLIM spectrogram determination and its overlay with the measured scene.

In the initial analysis, we tested the measurement for a more general bi-exponential fit, even though we expected the LuAG:Ce to show a monoexponential decay. The mapped region and the corresponding I_{DA0}, together with the IRF, are shown in Fig. 11. Fitting the I_{DA0} revealed the PL lifetimes of $\tau_1 = 11$ ns and $\tau_2 = 67$ ns.

The results of mapping $H\tau_1$, $H\tau_2$, and the FLIM spectrogram are presented in Fig. 12. The map of the first component can be assigned to random scattering points and scattered light along the crack. The map of the second component closely follows the shape of the crack, where the PL from LuAG:Ce is efficiently coupled out from the crystal. The FLIM spectrogram combines both amplitudes, where the second component dominates, owing to its high amplitude. The brightness of the individual pixels in the FLIM spectrograms was scaled according to the PL intensity, i.e., the sum of the amplitudes A_1 and A_2 in a given pixel. In Fig. 12, it is also possible to observe the overlay of the measured area and the obtained FLIM spectrogram. The overlay documents the agreement between the PL mapping and the sample properties. It is worth noting that only pixels with PL intensities greater than and including 10% of the maximum are shown in the FLIM spectrogram.

As we stated before, the assumption of the bi-exponential decay of LuAG:Ce was not physically correct. Moreover, τ_1 is close to the IRF width, which distorts A_1SPC. Therefore, we also provide an analysis of the PL, where we assume a monoexponential decay. Such a situation would, for instance, correspond to the mapping of a biological sample with a single PL marker. For the monoexponential decay, we obtained only one $H\tau$ region for the lifetime of 59 ns, which corresponds well with the PL lifetime of LuAG:Ce [36]. The $H\tau$ is directly represented in the FLIM spectrogram, as shown in Fig. 13. We can see that in this case we attained a clear image of the crack with high PL intensity together with low-intensity PL regions surrounding the cracks where the PL is outcoupled from the monocrystal inefficiently.

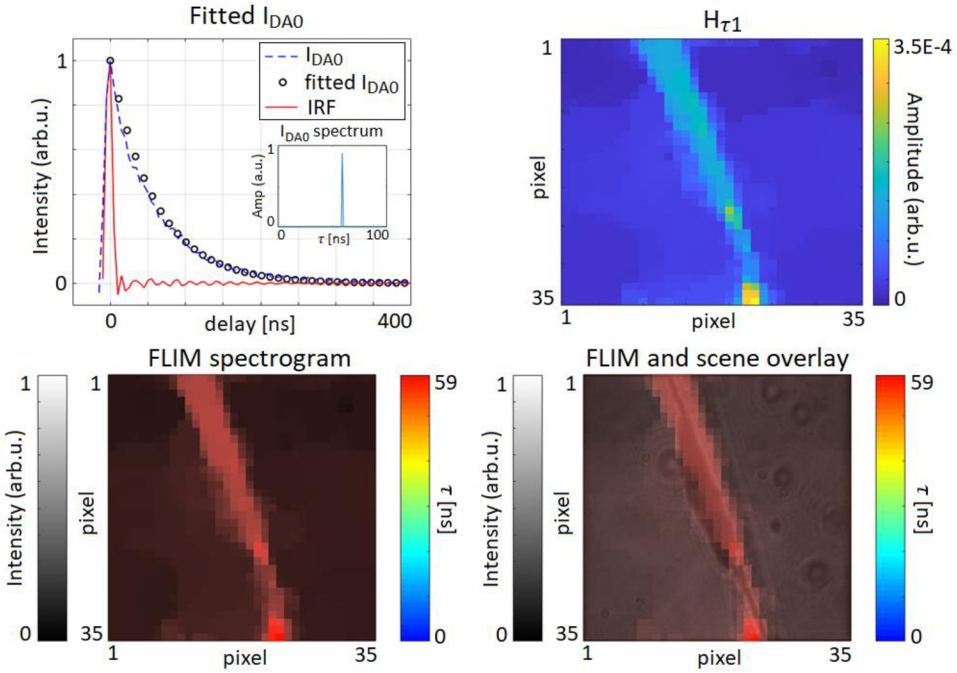

Figure 13: Upper panels: Fitted I_{DA0} with monoexponential curve and reconstructed area $H_{\tau 1}$ for corresponding τ_1. Lower panels: FLIM spectrogram determination and its overlay with the measured scene.

5. Conclusion

We outline two significant advancements for the RATS method for measuring PL dynamics and FLIM. The first is the possibility of random excitation via a digitally modulated signal. Using this approach, it is possible to achieve a time resolution down to units of nanoseconds and to significantly simplify the optical setup. Secondly, the article also presents a new approach to the evaluation of the FLIM spectrogram, which significantly reduces the number of necessary reconstructions of the undetermined system and reduces the post-processing time accordingly. Moreover, the novel approach to data processing reduces the required number of fitted curves in proportion to the chosen compression ratio k.

The original and the newly proposed approach to FLIM retrieval were compared in simulations regarding noise analysis. The new approach was demonstrated to reduce the possibility of locally incorrect lifetime determination. Therefore, the proposed amplitude map retrieval is more robust compared to the standard analysis against increasing noise level.

The advancements were implemented in a microscope setup based on the single-pixel camera technique. A digital micromirror device (DMD) was used to generate random patterns (masks), which also enables full illumination of the scene to determine lifetimes within the sample. In addition, the combination of DMD and random digital modulation of the laser increases the efficiency of the optical system a hundred times compared to the original arrangement using diffusers [23].

We analyzed the advancements on synthetic data, as well as on testing measurements. Namely, we carried out the imaging of a LuAG:Ce crystal, where a crack in the crystal was mapped. The resulting FLIM spectrograms from the PL analysis were in perfect agreement with the camera images.

Funding

This work was supported by the Ministry of Education, Youth and Sports ("Partnership for Excellence in Superprecise Optics," Reg. No. CZ.02.1.01/0.0/0.0/16_026/0008390), the Czech Science Foundation (GACR) (Grant number: 22-09296S), and the Student Grant Competition at the Technical University of Liberec (under project no. SGS-2021-3003).

Acknowledgment

We gratefully acknowledge CRYTUR company for providing us with LuAG:Ce crystals, and Jakub Nečásek for his help with a digital modulation device.

Disclosure

The authors declare no conflicts of interest.

Data availability

Data underlying the results presented in this paper are not publicly available at this time but may be obtained from the authors upon reasonable request.

References

1. R. Cubeddu, D. Comelli, C. D'Andrea, P. Taroni, and G. Valentini, "Time-resolved fluorescence imaging in biology and medicine," J. Phys. D: Appl. Phys. **35**(9), 201R61 (2002).
2. S. Kalinina, J. Breymayer, P. Schäfer, E. Calzia, V. Shcheslavskiy, W. Becker, and A. Rück, "Correlative NAD(P)H-FLIM and oxygen sensing-PLIM for metabolic mapping," J. Biophotonics **9**(8), 800–811 (2016).
3. J. M. Griffin, A. J. Miller, A. J. Berry, S. Wimperis, and S. E. Ashbrook, "Dynamics on the microsecond timescale in hydrous silicates studied by solid-state 2H NMR spectroscopy," Phys. Chem. Chem. Phys. 12(12), 2989–2998 (2010).
4. C. D. Wilms, H. Schmidt, and J. Eilers, "Quantitative two-photon Ca2 + imaging via fluorescence lifetime analysis," Cell Calcium 40(1), 73–79 (2006).
5. K. Žídek, F. Trojánek, P. Malý, L. Ondič, I. Pelant, K. Dohnalová, L. Šiller, R. Little, and B. R. Horrocks, "Femtosecond luminescence spectroscopy of core states in silicon nanocrystals," Opt. Express 18(24), 25241–25249 (2010).
6. K. Dohnalová, L. Ondič, K. Kůsová, I. Pelant, J. L. Rehspringer, and R.-R. Mafouana, "White-emitting oxidized silicon nanocrystals: Discontinuity in spectral development with reducing size," J. Appl. Phys. 107(5), 053102 (2010).
7. J.-C. Blancon, H. Tsai, W. Nie, C. C. Stoumpos, L. Pedesseau, C. Katan, M. Kepenekian, C. M. M. Soe, K. Appavoo, M. Y. Sfeir, S. Tretiak, P. M. Ajayan, M. G. Kanatzidis, J. Even, J. J. Crochet, and A. D. Mohite, "Extremely efficient internal exciton dissociation through edge states in layered 2D perovskites," Science 355, 1288–1292 (2017).
8. S. Kahmann, E. K. Tekelenburg, H. Duim, M. E. Kamminga, and M. A. Loi, "Extrinsic nature of the broad photoluminescence in lead iodide-based Ruddlesden–Popper perovskites," Nat Commun 11, 2344 (2020).
9. W. Becker, Advanced Time-Correlated Single Photon Counting Techniques, (Springer, Berlin, 2005).
10. J. Qu, L. Liu, D. Chen, Z. Lin, G. Xu, B. Guo, and H. Niu, "Temporally and spectrally resolved sampling imaging with a specially designed streak camera," Opt. Lett. 31(3), 368–370 (2006).
11. E. P. Buurman, R. Sanders, A. Draaijer, H. C. Gerritsen, J. J. F. van Veen, P. M. Houpt, and Y. K. Levine, "Fluorescence lifetime imaging using a confocal laser scanning microscope," Scanning **14**, 155–159 (1992).
12. Y. Won, S. Moon, W. Yang, D. Kim, W.-T. Han, and D. Y. Kim, "High-speed confocal fluorescence lifetime imaging microscopy (FLIM) with the analog mean delay (AMD) method," Opt. Express 19(4), 3396–3405 (2011).
13. E. Gratton, S. Breusegem, J. D. B. Sutin, Q. Ruan, and N. P. Barry, "Fluorescence lifetime imaging for the two-photon microscope: time-domain and frequency-domain methods," J. Biomed. Opt 8(3), 381–390 (2003).
14. I. Pelant and J. Valenta, Luminescence Spectroscopy of Semiconductors (Oxford University, 2012).
15. Y. Zhang, I. H. Guldner, E. L. Nichols, D. Benirschke, C. J. Smith, S. Zhang, and S. S. Howard, "Instant FLIM enables 4D in vivo lifetime imaging of intact and injured zebrafish and mouse brains," Optica, OPTICA 8, 885–897 (2021).
16. J. E. Sorrells, R. R. Iyer, L. Yang, E. J. Chaney, M. Marjanovic, H. Tu, and S. A. Boppart, "Single-photon peak event detection (SPEED): a computational method for fast photon counting in fluorescence lifetime imaging microscopy," Opt. Express, OE 29, 37759–37775 (2021).
17. L. Scipioni, A. Rossetta, G. Tedeschi, and E. Gratton, "Phasor S-FLIM: a new paradigm for fast and robust spectral fluorescence lifetime imaging," Nat Methods 18, 542–550 (2021).

18. B. Kim, B. Park, S. Lee, and Y. Won, "GPU accelerated real-time confocal fluorescence lifetime imaging microscopy (FLIM) based on the analog mean-delay (AMD) method," Biomed. Opt. Express, BOE 7, 5055–5065 (2016).
19. Q. Pian, R. Yao, N. Sinsuebphon, and X. Intes, "Compressive hyperspectral time-resolved wide-field fluorescence lifetime imaging," Nat. Photonics 11(7), 411–414 (2017).
20. R. Yao, M. Ochoa, P. Yan, and X. Intes, "Net-FLICS: fast quantitative wide-field fluorescence lifetime imaging with compressed sensing—a deep learning approach," Light Sci Appl 8, 26 (2019).
21. J. Junek, L. Ondič, and K. Žídek, "Random temporal laser speckles for the robust measurement of sub-microsecond photoluminescence decay," Opt. Express 28(8), 12363–12372 (2020).
22. K. Kůsová, O. Cibulka, K. Dohnalová, I. Pelant, J. Valenta, A. Fučíková, K. Žídek, J. Lang, J. Englich, P. Matějka, P. Štěpánek, and S. Bakardjieva, "Brightly Luminescent Organically Capped Silicon Nanocrystals Fabricated at Room Temperature and Atmospheric Pressure," ACS Nano 4(8), 4495–4504 (2010).
23. J. Junek and K. Žídek, "Fluorescence lifetime imaging via spatio-temporal speckle patterns in a single-pixel camera configuration," Opt. Express 29(4), 5538–5551 (2021).
24. A. N. Tikhonov and V. Y. Arsenin, "Solutions of ill-posed problems," SIAM Rev. 21, 266–267 (1977).
25. J. Junek, and K. Žídek, "Noise effect on 2D photoluminescence decay analysis using the RATS method in a single-pixel camera configuration," Opt. Express 30(8), 12654–12669 (2022).
26. P. Reinig, H.-G. Dallmann, M. Schwarzenberg, J. Ziebarth, J. Knobbe, J. Junek, R. Herbst, J. Rathert, R. Gerlach, U. Blache, S. Tretbar, and S. Fricke, "MEMS-based confocal laser scanning fluorescence microscopy for tumor demarcation in oncological surgery," in Advanced Biomedical and Clinical Diagnostic and Surgical Guidance Systems XX (SPIE, 2022), Vol. 11949, pp. 32–40.
27. G. M. Gibson, S. D. Johnson, and M. J. Padgett, "Single-pixel imaging 12 years on: a review," Opt. Express, OE 28, 28190–28208 (2020).
28. X. Liu, D. Lin, W. Becker, J. Niu, B. Yu, L. Liu, and J. Qu, "Fast fluorescence lifetime imaging techniques: A review on challenge and development," J. Innov. Opt. Health Sci. 12, 1930003 (2019).
29. C. Li, Wotao Yin, and Yin Zhang, TVAL3 Home, Rice University, 2009, Last updated 11/07/2013, https://www.caam.rice.edu/~optimization/L1/TVAL3/.
30. C. Li, W. Yin, and Y. Zhang, "User's guide for TVAL3: TV minimization by augmented lagrangian and alternating direction algorithms," CAAM Report20, 46–47 (2009).
31. A. A. Istratov and O. F. Vyvenko, "Exponential analysis in physical phenomena," Review of Scientific Instruments 70, 1233–1257 (1999).
32. G. Marsaglia, "Xorshift RNGs," Journal of Statistical Software 8, 1–6 (2003).
33. N. Chakrova, B. Rieger, and S. Stallinga, "Development of a DMD-based fluorescence microscope," in Three-Dimensional and Multidimensional Microscopy: Image Acquisition and Processing XXII (SPIE, 2015), Vol. 9330, pp. 23–33.
34. X. Chen, B. Yan, F. Song, Y. Wang, F. Xiao, and K. Alameh, "Diffraction of digital micromirror device gratings and its effect on properties of tunable fiber lasers," Appl. Opt., AO 51, 7214–7220 (2012).
35. Yu. Zorenko, V. Gorbenko, A. Voloshinovskii, G. Stryganyuk, V. Mikhailin, V. Kolobanov, D. Spassky, M. Nikl, and K. Blazek, "Exciton-related luminescence in LuAG:Ce single crystals and single crystalline films," physica status solidi (a) 202, 1113–1119 (2005).
36. M. Nikl, "Energy transfer phenomena in the luminescence of wide band-gap scintillators," physica status solidi (a) 202, 201–206 (2005).